Research & Development

2013

Mechanical Engineering Letters, Szent István University

TRANS−TRIO SCIENCES
Gent • Gödöllő • Baia Mare

Preface

The first and second officially announced GGB Trans-Trio-Sciences Workshop held in Szent István University, Gödöllő, was organized as a parallel session of „Synergy and Technical Development" international conferences in agricultural engineering, 2009 and 2011, Gödöllő. The selected and reviewed scientific content of the workshops was published in the "Mechanical Engineering Letters".

<div align="center">

„GBB Trans-Trio Sciences"
Gent – Gödöllő – Baia Mare

</div>

The further scientific co-operation of the partners in the field of tribology related engineering and design led to third workshop also escorting the *„Synergy and Technical Development"* international conference, 2013. This release of „Mechanical Engineering Letters" vol. 9. contains reviewed articles selected from the second Trans-Trio-Sciences Workshop concerning tribology from the points of materials, construction, computational and experimental modelling, friction and wear process control, maintenance of worn parts.

Prof. Gábor Kalácska	Prof. Patrick DE BAETS	Prof. Nicolae UNGUREANU
Szent István University	University Gent	North University
Gödöllő	Belgium	Baia Mare
Hungary		Romania

Contents

Exploration of tribological characteristics of naturally woven fiber composites

Jacob SUKUMARAN[1], Vanessa RODRIGUEZ[1], Siva IRULLAPPASAMY[2],
Winowlin Jappes JEBAS THANGIAH[3], Mátyás ANDÓ[4], Patrick DE BAETS[1]

[1]Department of Mechanical Construction and Production, Laboratory Soete, Ghent University
[2]Centre for Composite Materials, Kalasalingam University, Tamilnadu, India
[3]Department of Mechanical Engineering, CAPE Institute of Technology, Tamilnadu, India
[4]Institute for Mechanical Engineering Technology, Faculty of Mechanical Engineering,
Szent István University, Gödöllő

Abstract

Natural fiber composites (NFC) being one of the new interventions in the composite industry, is given less importance for tribological applications. In the current research, an in-depth study is made to understand the influence of normal force and speed, affecting the tribological characteristics. Various forms of lignocellulosic fibers exist, out of which coconut fibers are advantageous due to its naturally woven state. Tribological characterization was performed using a ball on disc configuration. Online measurements of friction force elucidate that the friction characteristics of naturally woven coconut sheath reinforced polymer (CSRP) composite stabilize at increased speed. Moreover, the orientation of the fiber strongly influences mode of wear.

Keywords

coconut fiber composite, wear, friction

1. Introduction

In the last few decades natural fiber composites (NFC) were always been a topic of discussion for structural applications „Ray *et al* (2001), Thamae *et al* (2007)". These NFCs are not new to the engineering industry, since automakers had its application in structural components (panel) in the early 50's. Special interest on these fibers has been recently created due to the fluctuations in the cost of synthetic fibers, energy intensive process and ecological consideration. NFC which is used in structural application has been limitedly explored from the tribological view point. Different categories of NFC comprise diverse groups having plant and animal fibers. Existing literature reports that the plant fibers such as banana fibres, jute, coir and sisal being commonly used as a reinforcing material „Mullick (2012), Singh *et al* (2012), Ashokan *et al* (2012), Majhi *et al* (2012)". These fibers are with different characteristics such as continuous and

discontinuous fibers. Considering the tribological application one of the important sectors is the bearing industry, where the use of continuous fiber as reinforcements has been followed for a long period. These continuous fibers are synthetically made and woven to be used as reinforcements, but as nature's gift there are fibers which exist in the woven form in the natural realm which can be post processed and used as reinforcements (Satyanarayana *et al* 1982). However, these fibers are not given any importance until Jappes *et al* started to study the mechanical and tribological chaecteristics of naturally woven coconut sheath reinforced polymer composites (CSRP), which has the advantage of having the woven state in nature (Jappes *et al* 2011). Reddy *et al* while comparing the different types of natural fibers has reported that the alkali treated coir sheath has superior tensile characteristics than Borassur, Tamarind, Hildegardia, Sterculia Urens (Reddy *et al* 2010).

Existing work on these CSRP composites were done for mechanical and tribological characterization "Jappes *et al* (2011) and Siva *et al* (2012)". However, the study has limitations in establishing a working range of parameters for extreme load conditions experienced in bearings. The current research aims at exploring the potential of these composites at extreme conditions in terms of normal force and speed. For that reason a ball on disc configuration is used where high contact pressure can be established from the Hertzian point contact. Two different loading conditions with a low load at 5 N and a high load at 20 N were used to investigate the tribological nature at extreme loads.

2. Materials and methods

In the current investigation, the preparation of CSRP composite comprises unsaturated Polyester (General Purpose grade: SBA2303) as matrix, Methyl ethyl ketone peroxide (MEKP) as catalyst and cobalt-naphthenate as accelerator. The naturally woven coconut sheath was acquired from the agriculture field in Tamilnadu, India. A photomacrograph of the coconut fibers is shown in fig. 1a. The naturally woven coconut sheath reinforced polyester composites are made using compression molding technique. More details about the manufacturing of coconut sheath composite were mentioned elsewhere in the earlier research (Siva *et al* 2012). For our investigation the disc size of 30 mm diameter were punched out of the laminated sheet. The used counter material is commercially available through hardened 100Cr6 steel. The laminated sheets were tested against 100Cr6 steel balls (Ø 6mm). Material properties are given in table 1. Adding to the existing properties the shore D hardness of the bulk material and specifically for individual fiber was measured using a Shore D hardness tester (BAQ) confirming to the ASTM D2240 standard. A typical microscopic image of the indentation made by the shore D indenter specifically on the main fiber is given in fig. 1b. The average of 5 shore D measurement for fiber and the bulk material are 67.9 ±1 and 72.3 ±1 respectively. The roughness of the polymer composite were measured using surface profilometer (Somicronic® EMS

Surfascan 3D, type SM3, needle type ST305) accordance with ISO 4228 standard. The arithmetical mean roughnesses (Ra) of polymer disc along the direction of fibers and across the direction of fibers were 3.34 and 3.78 µm ±10%, respectively. The post microscopy was performed using light optical microscope (Olympus).
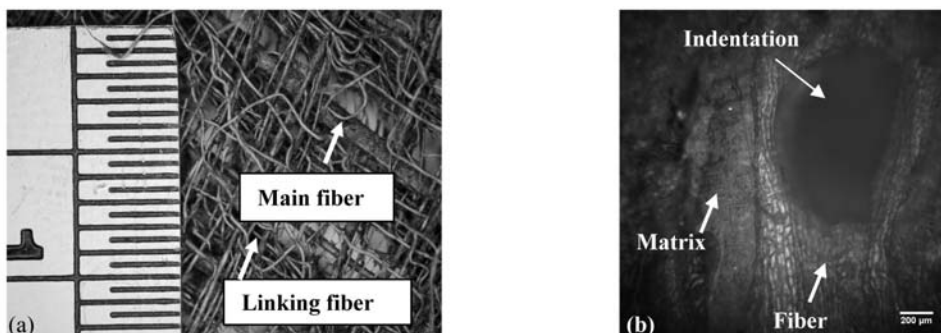
Figure 1. (a) Naturally woven coconut sheath fiber
(b) Shore D indentation on the main fiber

Tribological tests were done using a ball on disc configuration having a Hertzian point contact. All tests were performed using a tribometer (CSM, Switzerland) at room temperature of 25 ºC and a relative humidity of 50 % ± 5%. The schematics of the test configuration and the photomacrograph of the CSRP composite disc and the 100Cr6 ball specimen are shown in fig. 2. All tests were performed according to ASTM G99-95a standard. The test were conducted for three different surface velocity of 0.2, 0.4 and 0.6 m/s and two different loads of 5 N and 20 N corresponding to 70 MPa and 110 MPa contact pressure. All tests were performed for a sliding distance of 1000 m.
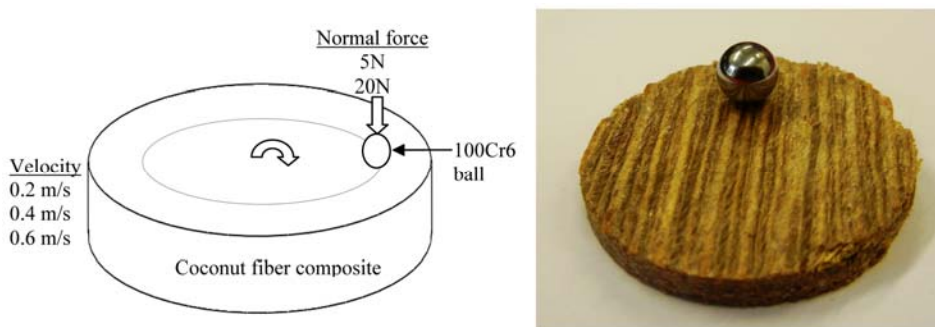
Figure 2. Schematics of the test configuration and the photomicrograph of the 100 Cr6 steel ball and naturally woven coconut sheath reinforced polymer composite disc specimen.

Table 1. Mechanical properties of the naturally woven coconut
fiber composite (Shiva *et al* 2012)

Properties	NFC
Tensile strength (MPa)	60
Elongation (%)	2.3
Young's modulus (MPa)	2608
Density(g/cm^3)	1.059

3. Result and discussion

Test results of composite disc on steel ball elucidates that the orientation of
fibers plays a significant role in deciding the friction and wear mechanisms.
From the visual inspection of the wear track and on the debris found on the steel
ball it is clear that the wear mode for the matrix is through brittle failure. Also no
signs of ductile flow can be seen in the wear track. Powder like debris are seen
in the vicinity of the wear track and also in the steel ball as shown in fig. 3. No
damage was observed in the steel ball except for the accumulation of polyester
matrix. The wear characterization by means of a penetration depth or estimating
the wear groove is hardly possible in this material due to the fact that the
material removal is fractional. The matrix is removed in the first place followed
by breaking of individual fibers. In such a case with the orientation of the fiber
in specific direction creates discrepancies in wear measurement.
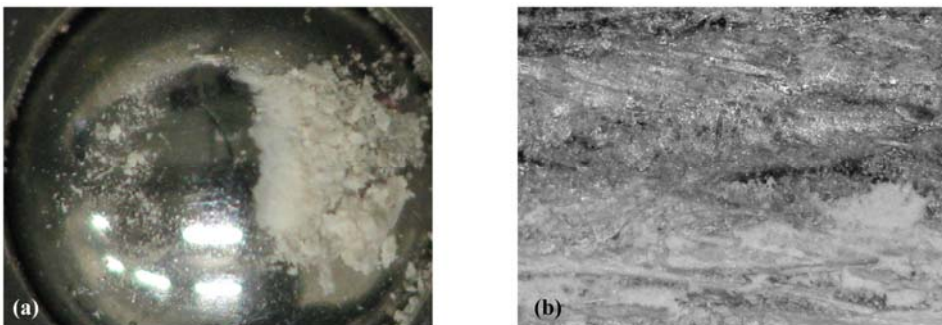
Figure 3. Photo macrographs of debris (a) steel ball tested at 0.6 m/s at 20N normal force
(b) composite surface

With the increase in sliding speed for both loading condition (5 N and 20 N)
there is an increase in friction coefficient. Fig. 4 shows typical friction curves for
all six test conditions. It is evident that there is a high rate of increase during the
initial run-in period followed by a steady state. The steady state friction was
accounted from 600 m to 1000 m of the total sliding distance.
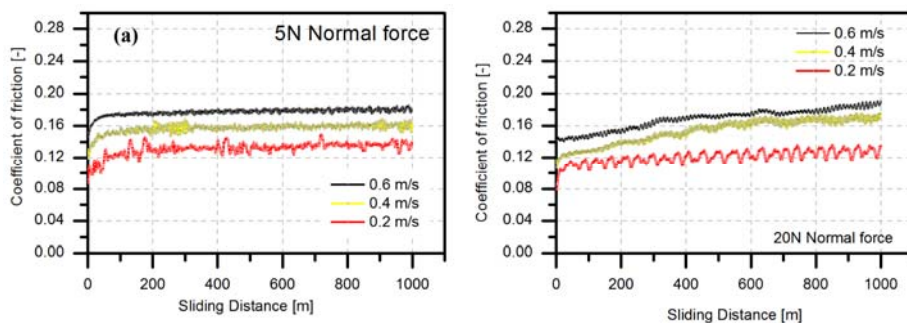
Figure 4. Friction curves (a) 5N load (b) 20N load

Comparing the friction characteristics of 0.2 m/s for both 5 N and 20 N it is clear that in low loading condition (5 N) the friction coefficient is quiet stable however on increasing the load to 20 N the friction coefficient fluctuates significantly. This is due to the fact that on high loading condition partial removal of individual phase occurs through removal of matrix by the steel ball thereby exposing the fibers to dominate the friction characteristics. This is clearly seen in the photomacrograph where the fibers are exposed and polishing effect of fiber by the steel counter face is evident as seen in fig. 5a. The fluctuation in this case is also due to the valley created from the matrix removal. However, in low load condition (5 N) the matrix is not completely removed as seen in fig. 5b thus, showing uniform friction behaviour. At 5 N load the steel ball glides over the surface without causing much damage in the matrix thus creating a situation of pure polymer on steel contact. Also from the width of the wear track it is clear that the penetration is more in case of 20 N normal force. One more feature which can be seen in the high load condition is the fibers are still intact without any significant damage providing mechanical strength to the laminate. The basic purpose of the fibers in reinforced composites is that the fibers take the mechanical loads for which the tribological characteristics are managed by the matrix. At low loading condition this hypothesis has been well maintained by the CSRP composites.
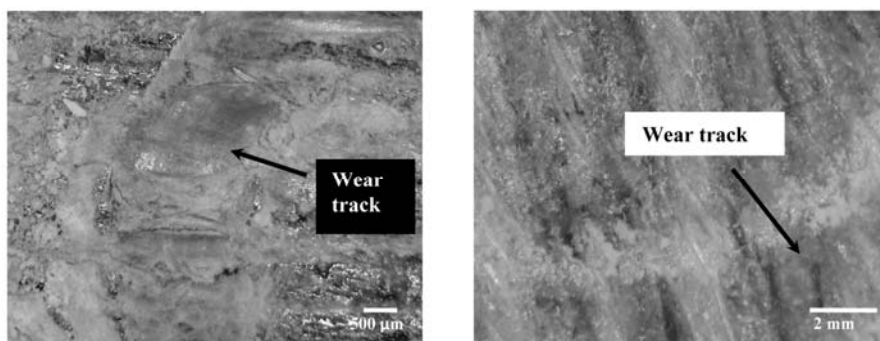
Figure 5. Photomacrograph of the wear track (a) 20N load at 0.2 m/s (b) 5N load at 0.2 m/s

Analyzing the friction curves (fig. 6), both the loading condition provide similar values of friction coefficient in the steady state for the three different speeds (0.2, 0.4 and 0.6 m/s). The mechanism of wear varies between different loads. On investigating the effect of speed there is a linear increase in friction force for 5 N normal force however, there is a slight variation in 20 N normal force which is due to the partial removal of matrix as explained earlier. Under small velocity 0.2 m/s the friction curve fluctuates more on comparing with 0.4 and 0.6 m/s speeds. It is typical, that measurements taken at low speed can be influenced greatly by the surface change effect than the measurements made at high speed condition.
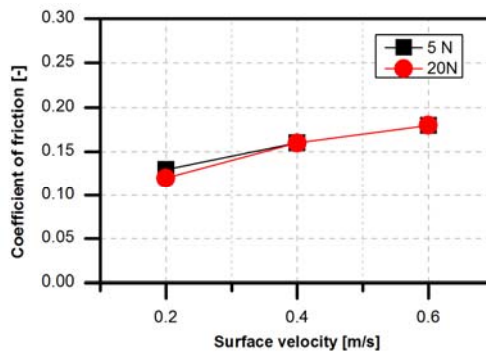
Figure 6. Friction map for naturally woven coconut fiber composite

A distinctive phenomenon in changing the wear mechanism is the fiber breakage at high speed and high load condition as shown in fig. 7a. However, such phenomenons are not experienced in low load condition (5 N) where the main mode of wear is by partial removal of matrix (fig. 7b). In fig. 7a the debonding of fiber matrix interface is also clearly observed. The breakage of individual fiber can be attributed to the impact of the steel ball at increased load. In the primary stage of wear the matrix are removed partially creating valleys between the two main fibers. When the steel ball glides over these two fibers an impact is created while sliding from one fiber to the other fiber. In our case the impact is effective only under high loading condition. In such a case the impact is introduced purely to the fiber where the ends of these fibers are supported by the matrix outside the wear track. The fracturing of individual fiber occurs only when the ball is sliding perpendicular to the fiber axis (fig 8a). However, when the ball is parallel to the fiber axis it glides over the fiber rather than creating an impact which causes the breakage of fiber. Thus, leaving no space for fiber damage when the fibers are oriented parallel to the sliding direction (fig. 8b). Similar effects were reported by other researchers while testing the influence of fiber orientation in altering the tribological characteristics. A comparable surface feature was earlier reported by Sharma *et al* where tests on carbon fiber

reinforced (UD) PEI has positive tribological characteristics when the fibers are oriented parallel (0º) to the sliding direction. However, when the fibers are perpendicular (90º) to the sliding direction brittle fractures of fibers were experienced (Sharma *et al* 2009). Analogous results were also reported by Shim *et al* for a test conducted on unidirectional carbon fiber reinforced epoxy composite tested against Stainless steel (SUS 304) (Shim *et al* 1992). Also a test by Liang *et al* on investigating the orientation of fiber affecting the tribological chaecteristics using a single pendulum scratching found that the fibers oriented perpendicular to the sliding direction experienced breakage of fibers (Liang *et al* 1996).
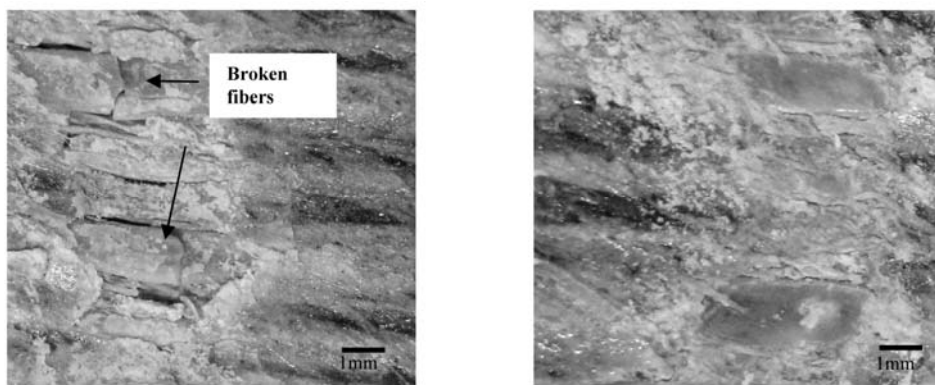
Figure 7. Shows the worn surface of composite at (a) 20 N and 0.6m/s (b) 5 N and 0.6 m/s
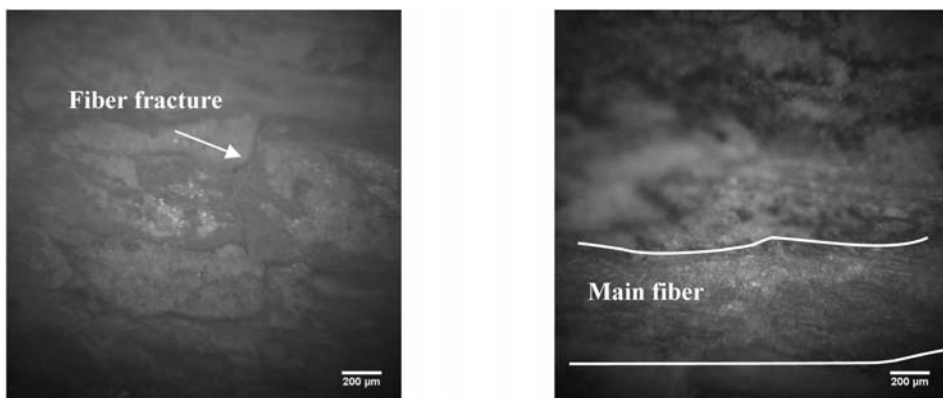
Figure 8. Worn surface of composite tested at 0.6 m/s at 20 N normal force (a) fibers oriented perpendicular to the sliding direction (b) fibers oriented parallel to the sliding direction

The overall tribological behaviour of the CSRP composite shows positive friction characteristics in the ball on disc test with 100Cr6 counter material, but, with small disadvantage of broken fibers in the perpendicular direction. Thus,

leaving more space for further investigations on the influence of fiber orientation.

Conclusions

In the investigation on establishing the working perimeter of coconut fiber composite the following conclusion can be drawn

- Between two different loads (5 N and 20 N), there is no significant change in coefficient of friction. However, the friction trends are stable at low loading condition (5 N).
- Considering the effect of speed the friction coefficient has a linear behaviour with the increasing speed.
- Eventhough there is an increase in friction coefficient at high speed condition the stable characteristics are established only at high speed on comparing with low speeds.
- From this research it is evident that CSRP composite provide best friction characteristics for high speed (0.6 m/s) with low load (5 N) operating conditions.

Acknowledgements

References

[1] Asokan, P., Firdoous, M., Sonal, W., (2012) Properties And Potential Of Bio Fibres, Bio Binders, And Bio Composites, Rev.Adv.Mater. Sci. Vol. 30 pp. 254-261.
[2] Jappes, J.T.W. and I. Siva, I., (2011) Studies on the influence of silane treatment on mechanical properties of coconut sheath-reinforced polyester composite. Polymer-plastics technology and engineering, 2011. Vol. 50(15): pp. 1600-1605.
[3] Majhi, S., Samantarai, S. P., Acharya, S.K., (2012), Tribological behavior of modified rice husk filled epoxy composite, Journal of Scientific & Engineering research, Vol. 3, (6), pp. 1-5.
[4] Mullick, S. S. (2012) Fabrication and Characterisation of alkali treated natural fibre reinforced polymer composites, Master thesis, Department of physics, Indian institute of technology-Rourkela, May 2012.
[5] Obi Reddy, K., Sivamohan Reddy, G.,Uma Maheswari, C., Varada Rajulu, A., Madhusudhana Rao, K., (2010) Structural characterization of coconut tree

leaf sheath fiber reinforcement. Journal of Forestry research, 2010. 21(1): pp. 53-58.

[6] Ray, D., Sarkar, B. K., Rana, A. K., Bose, N.R,(2001), Effect of alkali treated jute fibres on composite properties. Bulletin of Materials Science, Vol. 24(2): pp. 129-135.

[7] Satyanarayana, K., Pillai, C., Sukumaran, K., Pillai, S., Rohatgi, P., Vijayan, K., (1982) Structure property studies of fibres from various parts of the coconut tree. Journal of Materials Science, Vol. 17(8): pp. 2453-2462.

[8] Singh, V. K, Gope P. C., Sakshi,C., Singh, B. D., (2012), Mechanical Behavior of Banana Fiber Based Hybrid Bio Composites, J. Mater. Environ. Sci. Vol. 3 (1) pp. 185-194.

[9] Siva, I., Jappes, J. T. W., Suresha, B., (2012), Investigation on mechanical and tribological behavior of naturally woven coconut sheath-reinforced polymer composites, polymer composites ., Vol. 33, pp.723–732.

[10] Sharma, M., Rao, I. M., J. Bijwe, J., (2009), Influence of orientation of long fibers in carbon fiber–polyetherimide composites on mechanical and tribological properties, Wear 267 (2009) 839–845.

[11] Shim, H. H., Kwon, O. K., Youn, J. R., (1992), Effects of fiber orientation and humidity on friction and wear properties of graphite fiber composites, Wear, Vol. 157, pp. 141-149.

[12] Thamae, T. and Baillie, C. (2007), Influence of fibre extraction method, alkali and silane treatment on the interface of Agave americana waste HDPE composites as possible roof ceilings in Lesotho. Composite Interfaces,. Vol. 14(7-9): pp. 821-836.

[13] Liang, Y. N., Li, S. Z., Zhang, R. H., Li, S., (1996), Effect of fiber orientation on a graphite fiber composite in single pendulum scratching, Wear, Vol. 198, pp. 122-123.

Influence of abrasion wear process on amplitude roughness parameters

István BARÁNYI

Institute for Mechanical Engineering Technology, Szent István University, Gödöllő
Donát Bánki Faculty of Mechanical and Safety Engineering, Óbuda University

Abstract

Nowadays one of the most important tasks in tribology to design the surfaces optimised to the operation. According to the literature we can define clearly and detailed all of the optimal machining parameters, but we have only limited information about the changes of surface microtopography. In a case of tribological test researchers define the wear rate and form and identifying the wear form, but the roughness profile modification which defines example the real contact area, the heat and material transport have been investigated only a small degree.

In this article i would like to introduce the modification of the amplitude roughness parameters in a point of view of normal force and sliding distance in a case of non-lubricated abrasive process.

Keywords

wear, abrasion, average roughness, skewness, kurtosis, peak, valley

1. Introduction

In the past decades new roughness parameters and measuring systems have been developed, these new methods have been used only a small degree in the engineering practices. The widely used parameters (example average roughness and root mean squared roughness) define the basic manufactured specific in the case of orientated microtopography [Valasek, 2011], [Kári-Horváth, 2010][Kári-Horváth, 2009] or the roughness of the cutting tool [Sipos, 2010],[Horváth, 2011].

Tribologists often define the wear with the help of the wear rate in a function of normal pressure (normal force) and the sliding distance [Kalácska, 2012, 2013], but the literature consist only a few article from the roughness modification of the worn part [Zsidai, 2002], [Jánosi, 2004] or manage the realtime monitoring of the process [Ungureanu, 2007] [Rodregues, 2011], [Ando, 2012], [Sukumaran, 2011] . In my topic I would like to determine which „traditional" roughness parameters are represents the worn roughness profile correctly in a case of different abrasive wear state [Horváth, 2012].

2. Mathematical background and characterisation technique

The roughness measurement standards divide the parameters in different classes:
- Amplitude parameters (characterised with vertical features),
- Spacing parameters (characterised with horizontal features),
- Hybrid parameters, (characterised with horizontal and vertical features)
- Statistical parameters (characterised with statistical methods).

The wildly used amplitude parameters define the „traditional" approach wich wildly used in the engineering practice. These parameters mathematical background:

$$Ra = \frac{1}{N} \sum_{i=1}^{N} |y(i)| \tag{1}$$

$$Rq = \sqrt{\frac{1}{N} \sum_{i=1}^{N} y(i)^2} \tag{2}$$

$$Rv = |\min(y)| \tag{3}$$

$$Rp = |\max(y)| \tag{4}$$

$$Rsk = \frac{1}{NRq^3} \sum_{i=1}^{N} y(i)^3 \tag{5}$$

$$Rku = \frac{1}{NRq^4} \sum_{i=1}^{N} y(i)^4 \tag{6}$$

Where:
Ra   average roughness,
Rq   root mean squared roughness,
Rv   depth of the deepest valley,
Rp   height of the highest peak,
Rsk   skewness,
Rku   kurtosis,
N   number of the point in the measuring length,
y(i)   height coordinate of the point.

3. Investigated roughness profiles

The investigated surface topographies made by turning. The investigation was steel-sandpaper sliding pair. The sliding distance was between 600mm and 10800mm (the step was 600 mm) ,the normal force was between 200N and 600N (the step was 100N), the velocity was 25 mm/s and lubrication have not used.

The steel part profile was recorded a Mahr Perthen Concept 3D type stylus instrument. The travelling length was12.5 mm and the sampling distance was 0.5

μm. As Fig1. shows, the abrasive wear process particularly disappear the profile peak zone and modify the height coordinates of the points.

a., original

b., worn 1st stage

c., worn 2nd stage

d., worn 3rd stage
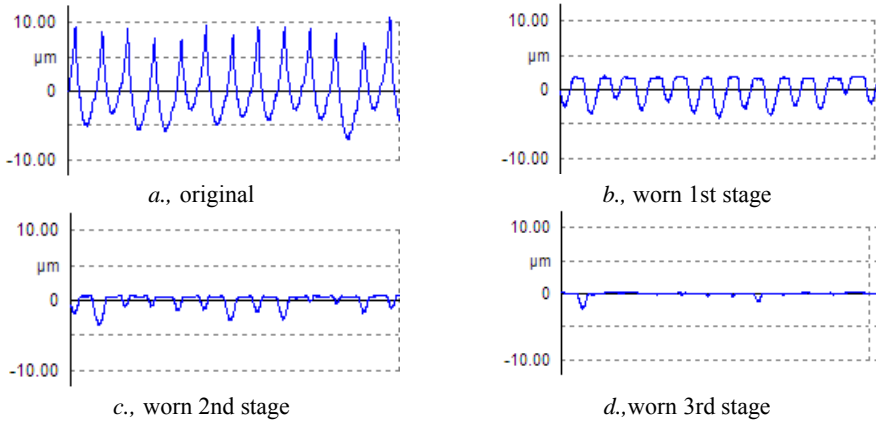
Figure 1.a-d The original and some of the worn roughness profile

a., average roughness

b., root mean squared roughness

c., depth of the deepest valley

d., height of the highest peak

e., skewness

f., kurtosis
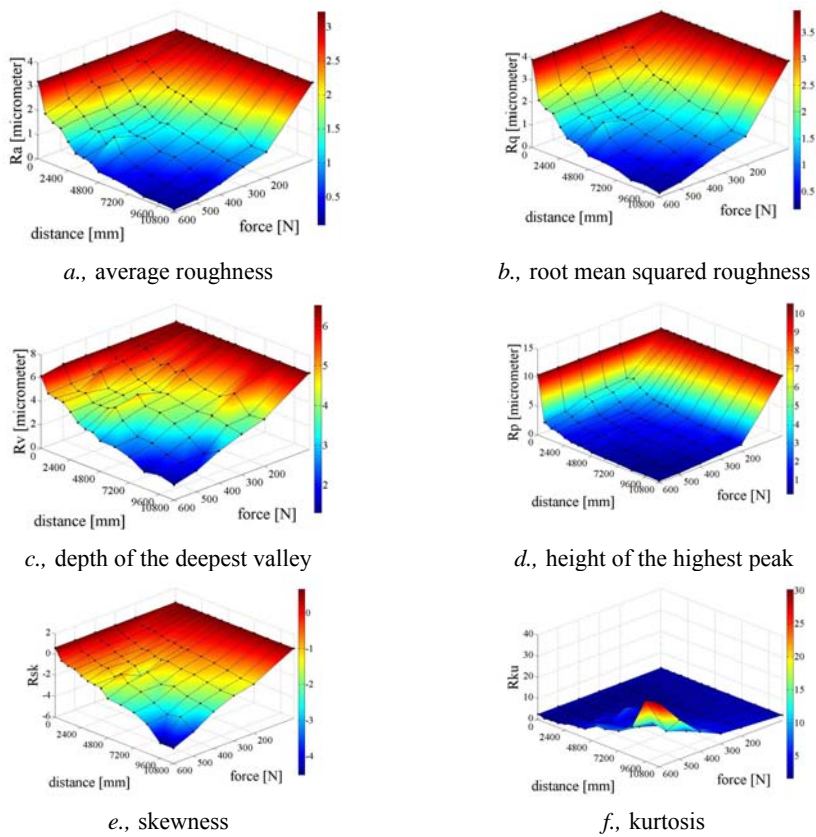
Figure 2.a-f the roughness parameters in a function of normal force and slideing distance

Figure 2a-f shows the modficiation of the value of the roughness parameters in the abrasive wear case from the manufactured microtopography to the totally disappeared microtopography stage.

4. Results and conclusions

As Fig 2. shows the roughness parameters values. The average roughness and the root mean square roughness graphs are similar tendency, because the mathematical definition these parameters are same (Rq less sensitive to the local errors).Fig 2 c and d represents the connection of the peak and the valley zone. The first stage of the process the peak zone apace disappeared and the depth of the valley zone decreased slowly.

The skewness and the roughness parameters demonstrate the specific feature of the wear process: The Rsk parameter decreased in a function of force and the distance, because the main line of the profile is moved downward. The grow of the Rsk value in the maximum of the distance and the force define the formation of the new surface microtopography for the abrasive grains.

References

[1] Ando, M.; Sukumaran, J. (2012): Effect on Friction for Different Parameters in Roll–Slip of Polyamide–Steel Nonconformal Contacts, Tribology transactions 55:(1) pp. 109-116.

[2] Horváth, Á.; Csík, Z.; Sukumaran, J.; Neis, P.; Ando, M.(2012): Development of brake caliper for rally-car Sustainable construction & design 3: pp. 191-198.

[3] Horváth, R.; Palásti K., B.; Sipos, S. (2011): Optimal tool selection for environmental-friendly turning operation of aluminium, Hungarian Journal of Industrial Chemistry 39(2), pp. 257-263

[4] Jánosi, L.; Sárközi, E.; Földi, L.; Józsa, N.(2004): Kopásvizsgálatok növényi olajjal. XI. Nemzetközi Pneumatika-Hidraulika Konferencia. Miskolc, Magyarország, 2004.09.21-2004.09.23. Miskolc,pp. 155- 161

[5] G. Kalácska, L. Zsidai, R. Keresztes, A. Tóth, M. Mohai, J. Szépvölgyi. (2012): Effect of nitrogen plasma immersion ion implantation of polyamide-6 on its sliding properties against steel surface. Wear 290-291. pp. 66-73.

[6] Kalácska G (2013): An engineering approach to dry friction behaviour of numerous engineering plastics with respect to the mechanical properties. eXPRESS Polymer Letters Vol.7, No.2 pp. 199–210

[7] Kári-Horváth, A. ; Valasek, I.(2010): Demand of Energy for Chip Detachment, Materials Science, Testing and Informatics, pp.489-497

[8] Kári-Horváth, A.; Valasek I.(2009): Machining: some new aspects, R&D Mechanical Engineering Letters, pp.75-87

[9] Rodregues, V.; Sukumaran, J.; Ando, M. (2011): Roughness measurement problems in tribological testing, Sustainable construction & design 2:(1), pp. 115-121.

[10] Sipos, S.; Palásti K., B.; Horváth, R. (2010): Environmental-Friendly Cutting of Automotive Parts, Made of Aluminium Castings, Hungarian Journal of Industrial Chemistry 38:(2), pp. 99-105

[11] Sukumaran, J.; Ando, M.; Rodregues, V.; De Baets, P.; Neis, P. D.(2011): Friction torque, temperature and roughness in roll-slip phenomenon for polymer –steel contacts, Mechanical engineering letters: R&D : Research & Development 5, pp. 7-16

[12] Ungureanu, M., Ungureanu, N., Stoicovici, D., (2007): Study of wear of friction lining of break shoe, Scientific Bulletin, serie C, fascicle Mechanics, Tribology, Machine Manufacturing Technology, Volume XXI, 2007, ISSN 1224-3264, cod CNCSIS 610, pp. 707-712.

[13] Valasek, I.; Kári-Horváth, A. (2011): The action mechanism of minimum lubrication and the increase of its efficiency, Tribologie und scmierungstechnik, 58. Jahrgang 3/2011, pp.34-47

[14] Zsidai, L.; De Baets, P.; Samyn, P.; Kalácska, G.; Van Peteghem, A.P.; Van Parys, F. (2002): The tribological behaviour of engineering plastics during sliding friction investigated with small-scale specimens, Wear 253, pp.673–688

Dynamics of starting up of the mining elevator

Miorita UNGUREANU, Nicolae UNGUREANU

Engineering and Technological Management Department, Technical University of Cluj Napoca,
North University Center of Baia Mare, Baia Mare

Abstract

This study is focused on basic to develop the method of approaching the dynamic process in case of starting up the mining elevator. Starting from the general dynamic equation for the operation of the mining elevator one has studied the transitory processes start up, thus obtaining the differential equation of the movement of the driving element and the expression of the maximum moment when starting up the extraction machines.

Keywords

mining elevator, starting up moment, generalized coordinate, kinetic energy, potential energy.

1. Introduction

General dynamic equation of the mining elevator
The general dynamic equation is obtained by applying the d'Alambert principle, according to which the sum of the inertia forces and of the action forces the whole system, is considered to be in equilibrium. By replacing the forces with moments, the motor moment at the shaft of the winding organ (Fig.1) is balanced by the moments of the static forces, of friction, and of the dynamic ones. In this context one can write [1] [4]:
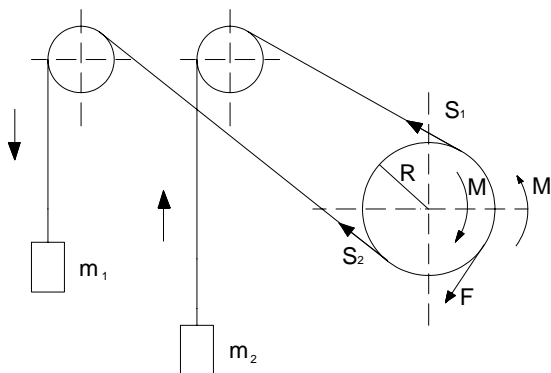
Figure 1. Basic scheme of a hoisting mining equipment

$$M = M_{st} + M_r + M_{din},$$

(1)

In equation (1): M is the motor moment, M_{st} - the static moment, M_r- the moment of the friction forces and M_{din} - the dynamic moment.

If we take into account the fact that the arm of the forces acting are the periphery of the winding element is its R radius, the expression (1) can be written according to forces as follows:

$$F = F_{st} + F_r + F_d$$

(2)

In equation (2) F_{st}, F_r, F_d are the static forces, the resistance forces and, respectively, the dynamic forces, reduced at the periphery of the winding element.

The dynamic forces are calculated as follows:

$$F_d = m_i \cdot a$$

(3)

In equation (3): - m_i is the reduced mass of the hoisting mining equipment related to the periphery of the winding element, and $a = \dfrac{d^2 x}{dt^2}$ is the linear acceleration at the periphery of the winding element.

The dynamic moment is calculated as follows:

$$M_{din} = \sum m_i \cdot R \frac{dV}{dt}$$

(4)

In equation (4): - R is the radius of the winding organ, $V = \omega \cdot R$ - linear movement speed, ω - angular speed of the drum.

Generally, both values ω and R are variable, thus it results:

$$\frac{dv}{dt} = \frac{d\omega R}{dt} = R \frac{d\omega}{dt} + \omega \frac{dR}{dt},$$

(5)

In (5) one can introduce the following notations:

$$\frac{d\omega}{dt} = \varphi$$

(6)

where φ is the angular acceleration,

$$\frac{dR}{dt} = u_R$$

(7)

where u_R is the speed on the radius direction, of the contact point of the cable with the drum, and

$$\omega \cdot u_R = \omega \frac{dR}{dt} = a_R$$

(8)

where a_R is the winding acceleration with variable radius.

Replacing the expression (5) in the expression (4) one obtains:

$$M_{din} = \sum m_i \cdot R^2 \cdot \varphi + \sum m_i \cdot R \cdot a_R$$

(9)

But:

$$\sum m_i \cdot R^2 = I \,,$$

(10)

where I represents the total inertia moment.

According to the expressions (1) (4) and (10) it results [2]:

$$M = M_{st} + M_r + I\varphi + \sum m_i \cdot R \cdot a_R$$

(11)

This equations represented in the most general form is called the general dynamic equation of the hoisting mining installations, and is valid both for constant winding radius and for variable winding radius.

Transitory processes when starting up the hoisting mining machines

Depending on the influence of the resistant forces, one can have the following situations:
  − Unloaded start, in which case the resistant forces are small;
  − Start under full load, in which case the resistant moment can be considered constant;
  − Unloaded start, followed by the sudden application of a constant load.

The display of the process of starting up the mining elevator depends on the dynamic characteristics of the machine, on the distribution of the masses and of the elastic elements.

In case of starting up the hoisting mining machine, we will use Lagrange's equations [3][5]:

$$\frac{d}{dt}\frac{\partial E}{\partial q_i} - \frac{\partial E}{\partial q_i} = Q_i$$
, (i=1,2,…..n)   (12)

Where:

– E – Kinetic energy of the system;

– q_i – Generalized coordinate;

– $\dot{q}_i$ – Generalized speed;

– Q_i – Generalized moment.

In this case the system has a degree of freedom, therefore k=1.

The following relation gives the kinetic energy of the system:

$$E = \frac{1}{2}\cdot\left(I_t - I\right)\cdot\varphi^2$$
                                                (13)

Where:

– I_t – Moment of inertia of all masses in movement, reduced at the axis of rotation of the motor;

– I – Moment of the inertia of the motor rotor;

– φ – Rotor rotation angle, considered as being the generalized coordinate, therefore $q = \varphi$ and $\dot{q} = \dot{\varphi}$.

The generalized moment is:

$$Q = M - M_r$$
                                                (14)

Where M is the driving motor moment, and M_r is resistant moment.

In the stage when the equipment is started up the motor moment is a variable value. For the non-synchronous motors it is calculated with the relation:

$$M = \frac{2M_{max}}{\left(\dfrac{S}{S_m} - \dfrac{S_m}{S}\right)},$$
                                                (15)

Where:

– M_{max} – overturning moment of the motor;
– S – slipping;
– Sm – slipping corresponding to the overturning moment.

The slipping is calculated with the following relation:

$$S = I_t - \frac{\omega}{\omega_0}$$

(16)

Where:
  – ω – the angular speed of the rotor at a certain moment;
  – ω_0 – the rotation speed of the stator magnetic field.

Taking into account what was said above, results the differential equation of the movement of the operation organ in the discharge stage:

$$(I + I_t) \cdot \frac{dS}{dt} = M_r - \frac{2M_{max}}{\dfrac{S}{S_m} + \dfrac{S_m}{S}}$$

(17)

Materials and methods

Dynamic stress at the start up of the mining machine
In order to determine the dynamic stress when starting up the hoisting mining machine we will consider the reduced scheme from figure 2 of a hoisting mining machine, where one has marked with J1 the reduced moment of inertia of the working element and of the transmissions, J2 the reduced moment of inertia of the rotor of the driving motor, K the elastic constant of the transmission main shaft, M1 the reduced resistant moment, and with M2 the motor moment, which is considered constant.

In the start up stage the following condition is met:

M2 >M1

The real operation scheme can be different depending on the type of the mining machine, but can be generally reduced to the presented scheme.
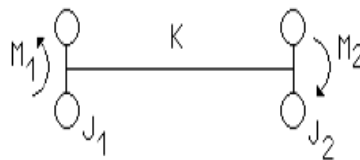

Figure 2. Reduced scheme for determining the stress when starting up
the hoisting mining machines [1]

In all kinematics schemes of the hoisting mining machines there are connections with clearance, due to the presence of the gear wheels, of the couplings, cables, etc.

The process of starting up of a hoisting mining machine can be divided into three distinct stages:

Idle acceleration of the rotor of the driving motor, as a result of the presence of the clearance from the kinematics scheme, without driving the working element.

Movement of the rotor of the driving motor in the presence of the force of elastic deformation of the transmission, the working element not being driven before the moment when the elastic deformation force becomes bigger than the resistant force.

Starting up the working element.

In order to calculate the maximum starting up moment the Lagrange equation is used. [3][5]:

$$\frac{d}{dt}\frac{\partial E}{\partial \dot{q}_i} - \frac{\partial E}{\partial q_i} + \frac{\partial W}{\partial q_i} = Q_i$$

$$(i=1,2\dots n) \qquad (18)$$

where the two generalized coordinates are q1=J1 and q2=J2, and W is the potential energy of the system that is determined with the relation:

$$W = \frac{E}{2}\cdot\left(\varphi_2 - \varphi_1 + \varphi_0\right)^2 - \frac{K}{2}\cdot\varphi_0^2 \qquad (19)$$

where:

– $\varphi_0 = \dfrac{M_r}{K}$ – is the preceding deformation that appears in transmission in the second stage of the starting up process;

– K – elastic constant of the shaft.

Kinetic energy, respectively, the generalized forces will have the shape:

$$E = \frac{1}{2}\cdot\left(J_1 \quad \varphi_1^2 \right) \qquad (20)$$

$$Q_1 = M_1 ; Q_2 = M_2$$

One bears in mind the fact that at the initial moment t=0 we have $\varphi_1 = 0; \varphi_2 = \omega_1$, where ω_1 is the angular speed of the rotor at the beginning of the displacement of the working element.

In these conditions the maximum moment will be calculated with the relation:

$$M_{max} = M_r + \frac{\Delta M \cdot J_1}{J_1 \cdot J_2} + \frac{\dfrac{k \cdot J_2 \cdot \omega_1^2}{\Delta M} + \dfrac{\Delta M \cdot J_2}{J_1 + J_2}}{\sqrt{I + \dfrac{\omega_1^2 \cdot k \cdot J_2 \cdot \left(J_1 + J_2\right)}{J_1 \cdot \left(\Delta M\right)^2}}} \qquad (21)$$

Conclusions

The transitory processes that appear when starting up the mining elevator are influenced by the type of the electric driving motor, by the size and the character of the variation of the external forces.

The maximum moment for starting up the mining elevator depends on the reduced inertia moment of the working element and of the transmissions, on the reduced inertia moment of the rotor of the driving motor and on the elastic constant of the main transmission shaft.

References

[1] Magyari, M.A.: Cercetări privind îmbunătăţirea parametrilor constructivi şi funcţionali ai instalaţiilor de extracţie miniere, Teză de doctorat, Petroşani 2001.
[2] Mereţ, N., Micheş Gh.: Instalaţii de extracţie, pompe, ventilatoare şi compresoare în industria minieră, Editura Tehnică , Bucureşti 1971
[3] Kecs, W.: Complemente de matematici cu aplicaţii în tehnică, Editura Tehnică, Bucureşti,1981.
[4] Popa, A., s. a.: Manualul inginerului de mine, vol V, Editura Tehnică, Bucureşti, 1989.
[5] Ridzi, M.: Contribuţii la diagnosticarea vibromecanică a maşinilor, Teză de doctorat, Universitatea din Petroşani, 2006.
[6] Ungureanu, M.: Contribuţii privind unele aspecte tribologice apărute în funcţionarea instalaţiilor de extracţie miniere, Teză de doctorat, Baia Mare 2004.

Destructive testing of metallic and non-metallic materials

István SEBŐK, György GÁVAY

Faculty of Military Sciences and Officer Training
National University of Public Service

Abstract

Combat vehicles and other bulletproof devices are protected by metallic and non-metallic armour. The ballistic protective elements are categorized by standards. Such examinations are needed to show the real capabilities of the armours after or near the end of the warranty period.

Keywords

APC, metallic armour, body armour, destructive testing

1. Introduction

The protection of soldiers, devices and supplies from the probable and increasingly often happening attacks is highly important in the foreign missions of the Hungarian Defense Force.

Various vests and their protective panels have been developed for personal protection, [MSZ K (1999)] military standards contains the regulations of their level of protection. Vehicles and other devices are protected by metallic and non-metallic armour, which are subsequently installed in some cases, like that of the „H" truck series produced by Raba Vehicle Ltd. [Burkus, (2011)], [Tóth, (2011)]. The capacities of the ballistic protective elements are categorized and examined based on standards – for example in town Táborfalva, by the HM VGH (Defense Economy Office, Ministry of Defense).

The experiences of the NATO missions in the past decade show growth in the level of protection on an international level. This article outlines methods of examination that can provide improvement of the protection capability of the above mentioned metallic and non-metallic body armour regarding metallographical basis. We plan to examine the actual behaviour of ballistic personal protective equipment under and after the warranty period when a bullet impact happens.

The subject of the examination is the ballistic and metallographical analysis of the metallic and non-metallic materials used by the Hungarian Defense Force for the personal defense and for the configuration of the monolithic armour of the armoured personnel carriers.

Planned examinations:
1. Changing of the protection capabilities of the composite materials used body armour and protective vest after the warranty period, what is specified by the manufacturer.
2. Behaviour of metallic materials at the impact and penetration of a bullet.

The examination of the metallic and non-metallic materials is a separate process. The results of the firstly mentioned analysis can be used for testing the status of the personal ballistic protection elements. The results of the second examination can be applied in respect of the additional armouring and the additional inner or outer strengthening of the inside of the vehicle.

2. Purpose of the examination

Regarding the non-metallic materials, the beahaviour of the bulletproof vests and their protective panels can be analyised with these examinations. The basis of protection of the vests is guaranteed by the soft panel, the protection level of which ranges from NIJ I to NIJ III/A. [NIJ (2008)] The protection against the bullets of bigger calibre guns can be achieved with hard, so called ceramic plats, the material of which is usually some kind of a composite material. Aramid strands (high solidity polyethylene [HPPE] strands) are used as strand-strengthening components in these materials. The hard layer is made of ballistic ceramics, the main ingredients of which are aluminium oxide, silicon carbide and boron carbide. Their level of protection usually ranges from NIJ.III to NIJ.IV.

On the basis of the NIJ standard, U.S. manufacturers still give 5 years warranty for the protective panel, but European manufacturers often raise this to 10 years. [Frank, (2009)] This can be traced back to the technological development and to the fact that the used materials are less sensitive to humidity or other external impacts than 10 years ago.

The warranty period of protective vests is 7 years in the Hungarian Defense Force. Hungarian Defense Force and the manufacturer can extend this to 10 years according the contract. The purpose of the examination is the analysis of the protective panel of the vest – how much the texture of the elemental strands changes during the 10 year lifespan.

In case of non-metallic materials the purpose of the examination is basically the analysis of the panel and its components after the warranty period. Our another purpose is the control of the warranty extension.

Metallic materials are homogeneous steel-plates of different thicknesses, which also contain the steel-plate that is equivalent or identical to that of the BTR 80 armoured personnel carrier. The basis of the examination is the grown demand for protection, which is generated by the handguns with bigger calibres and the so called AP bullets used with them. We are planning to collect data with the penetration of the plates, the metallographic analysis of the damaged surfaces and the measurement of the speed of the bullet before impact and after penetration. This data can serve as the basis of a research and development.

3. Description of the examined materials

Non-metallic materials:
– Kevlar ®: The registered trademark of the para-aramid synthetic fiber. It can be connected to other aramids such as Nomex and Technora. Developed at DuPont in 1965, this high strength material was first commercially used in the early 1970s as a replacement for steel in racing tires. Currently, Kevlar has many applications, ranging from bicycle tires and racing sails to body armor because of its high tensile strength-to-weight ratio; by this measure it is 5 times stronger than steel on an equal weight basis. It is mainly known as Kevlar ® 29, Kevlar ® 49 or Twaron ®. Twaron ® is a Dutch aramid type that is chemically and physically similar to DuPont's Kevlar®. Twaron ® HM (High modulus) has similar stretch properties to Kevlar 49, greater tensile strength and better UV resistance. [DuPont™(2013)]
– Kevlar ® 29: Strong, does not stretch, lightweight, but it does not resist flexion or UV. [DuPont™, (2013)]
– Kevlar ® 49: Very strong, its stretch properties are worse as that of the K29, lightweight, does not resist flexion or UV. [DuPont™, (2013)]
– Twaron ® SM is similar to Kevlar ® 29. Like Kevlar ® the fiber is a bright gold color. [Teijin Human solution, (2013)]
– Dyneema ®: Dyneema ® produced by the Dutch company DSM. It consists of high-molecular-weight polyethylene molecules. The high molecular weight polymers not liquid, they can be turned into strands with a complicated chemical process. Dyneema ®is just as strong as the high-solidity strands. It is a highly flexible, highly durable and has good stretch properties thanks to its long chain structure. The flexibility of the fiber is not affected by multiple folding, UV radiation or wearing. It can be used layed on a thin mylar ® layer like kevlar, but also as a separate material. Dyneema® is used in armored helmets, vests, shields and inserts to protect against a wide range of ballistics threats. Personal Armor, made with Dyneema®, help safeguard "everyday heroes"- such as soldiers, law enforcement officers, commercial pilots and high-profile civilians. Dyneema® Soft Ballistic (SB) armor solutions are used in vests and clothing to provide life-saving protection against handgun ammunition and knives. Dyneema® Hard Ballistic (HB) armor solutions are incorporated into ballistic inserts and helmets to protect against heavier and more penetrating threats such as rifles and high-speed fragments, such as those from IEDs. [Dyneema® in Personal Armor, 2013]
– The hard layer is made of ballistic ceramics, the main ingredients of which are aluminum oxide, silicon carbide and boron carbide. [Frank, (2008)]

In case of metallic materials the examination is limited to the analysis of homogeneous steels. The steel armour-plate has a hardness is 450-500 HB. [Frank, (2000)] We are planning to examine plates with different thicknesses (5-12 mm), in accordance with the armour presently used for combat vehicles.

4. The examination

The two examinations are almost alike, but the non-metallic target objects require significant preparation. The material replacing the human body needs to meet the requirements of the MSZ K 1114-1 standard. The samples need to be stored for at least four hours on 293 K ± 2K {20 ± 2 °C} temperature and 65 ± 5% relative humidity before the examination. In case of wet conditioning all elements of the protective equipment need to be put into a bowl containing water for 60 +/- 3 minutes and dipped to at least 200 mm below the water surface. The examination can to be started after taking out the equipment of the water and letting the water drop out of it for 3 minutes and the examination needs to be finished within 30 minutes. If the examination can not be finished within this time, the analysis needs to be restarted with a new protective equipment. The [MSZ K, (1992)] includes handling methods of the guns at the exhamination.

5. The process of the examination

The test is shown by the figure 1. Tested armour is fired from a fixed weapon. The bullet passes the speedometer gates and then slams into the target. The impact and the penetration of the bullet is fixed by the high speed camera. The velocity of the bullet is measured using the scale and with the help of the time parameter appearing on the high speed camera, from which the kinetic energy of the bullet can be calculated [Gávay, (2011)]. From the decrease in kinetic energy of the bullet can be deduced the quantity of the energy swallowed by the target.
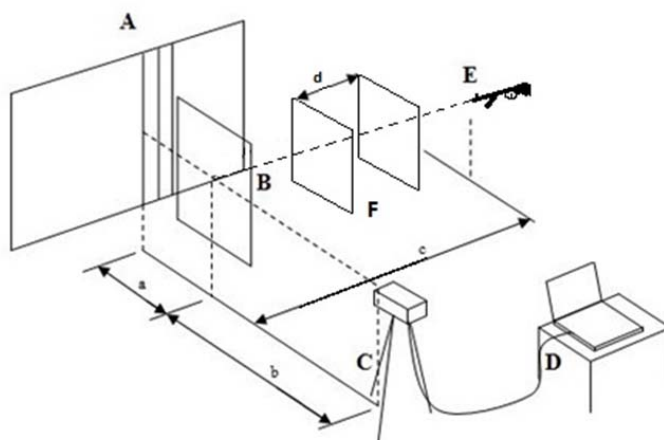

Figure 1. The area of examination (A – background with scale, B – target object,
C – speed cam, D – equipment for saving data, E – gun,
F – speedometer unit, a – distance between impact point and background,
b – distance between impact point and high speed cam,
c – distance between impact point and gun, d – distance between speedometer units)

6. Examination in case of not metallic ballistics substances

It is necessary to examine all of the parts of a protective equipment in aspect of the ballistic protection, first in a wet, and in a drily conditioned state too.

It is inadequate a penetration caused by a regular hit. The base on the standard we plan to examine to protective capability armour or plate in the level (L2, L3, L4, L5 L6). [MSZ K, (1999)]

It is necessary fired both side of body armour because the body armour front and back side contain protective panel.

Neighter a bullet with one single regular hit, nor one with lower speed under the lowest velocity value can cause penetration or a larger imprint depth than the allowed one.

All of the panel should be removed from the test sample. The wet-conditioned sample on the prepared and controlled-filling material surface should be fixed with belts, straps, bands, other aides that the ground side of test sample has to contact everywhere with the expletive subtance, and the impact of surface has to stay free as the shots can be placed on the sample in provided geometry and number.

The test risk factors reflected in the protective armours life.
  – Thermal (examination of the impact of the climate). The tensile strength of the protect element influenced by a longer air relative humidity on the environment and actual temperature. Tests in climate cabinet show that the longer warmer, dry temperature hardly ever causes a reduction of tensile strength in protect element, while the longer humidity does.
  – Chemical - the materials found in daily life during the lifetime of an armour exposed to texture examination of chemical substances for adverse effects.
  – High-energy radiation, in particular on UV radiation aging consequences of impact.
  – Examination of mechanical stress - in principle in daily use in the crease and other mechanical stress protection capacity of impact of changes in the material
  – Effect of protective power of biological causative agents to (used here primarily) the armours direct the human body and the effect of mating to the protective power changes of substance.

7. Examination in case of metallic ballistic substances

The test is basically the same but the difference is, that in this case, the metal destructed by punctures.

During the test designed for measurement parameters:
  – Definition of the bullet speed before the hit using speedometer gates,
  – Fixing of the movement of the bullet using high speed camera,
  – Calculating the impact speed of bullet (with puncture or repercussion) by a direct way, or the kinetic energy indirect way (in the background by using the scale)

- Estimation of the kinetic energy transform after the hit.
- Examination of behavior and deformation of targets,
- Metallographical test of deformed, destructed plate.

References

[1] MSZ K Standard 1114-1 (1999) Body armours. Bulletproof vests
[2] Burkus, Z. (2011) Honvédségi projekt: moduláris járművédelem a Rábától, http://www.autopro.hu/gyartok/raba-holding/Honvedsegi-projekt-modularis-jarmuvedelem-a-Rabatol/1883/
[3] Tóth, Gy. (2011) Páncélból lesz még a szélvédő is http://www. kisalfold.hu/gyori_hirek/pancelbol_lesz_meg_a_szelvedo_is/2210257/
[4] Frank, Gy. (2009) A Lövedékálló védőmellény alapanyagai és a degradáció veszélye Bolyai szemle XVIII. évf. 3. szám p. 95-114 ISSN 1416-1443
[5] NIJ Standard 0101.06 (2008) Ballistic Resistance of Body Armor
[6] Frank, Gy. (2000) Páncélozott pénz- és értékszállító biztonsági gépkocsik ZMNE 53. oldal
[7] MSZ K Standard 1018 (1992) Guns. Test methods at mass production
[8] Frank, Gy. (2008) Ballisztikai kerámia alkalmazása testpáncélokban karabély- és puskatöltények lövedékei ellen Bolyai Szemle XVII. évf. 3. szám p. 113-122 ISSN 1416-1443
[9] Gávay, Gy. (2011) Ütésálló Lexan védőpajzs vizsgálata nagysebességű film-felvételekkel rögzítve diplomamunka
[10] Dyneema® in Personal Armor (2013) http://www.dyneema.com/emea/applications/life-protection/personal-armor.aspx
[11] DuPont™(2013) http://www.dupont.com/products-and-services/fabrics-fibers-nonwovens/fibers/brands/kevlar.html
[12] Teijin Human Solution (2013) http://www.teijinaramid.com/aramids/twaron/

High temperature sliding friction response of ZrB_2-20%sic ceramic composite

Yeczain PÉREZ DELGADO[1], Koenraad BONNY[1], Mariana STAIA[1],
Vanessa RODRIGUEZ[1], Olivier MALEK[2,3], Jef VLEUGELS[2],
Bert LAUWERS[3], Patrick DE BAETS[1]

[1]Department of Mechanical Construction and Production, Laboratory Soete, Ghent University
[2]Metallurgy and Materials Engineering Department, Catholic University of Leuven
[3]Mechanical Engineering Department, Catholic University of Leuven

Abstract

Continuous sliding experiments on pulse electric current sintered (PECS) ZrB_2-20vol%SiC have been conducted at temperatures of 25 and 1000°C in dry atmospheric conditions according to the ASTMG99-95a standard. SiC balls of 5 mm diameter were used as stationary counterpart. The ZrB_2-20vol%SiC disc specimens were surface finished by polishing. The tests were performed using a sliding speed of 0.3 m/s and maximum Hertzian contact pressure of 2.5 GPa. The experimental results demonstrated that the friction response of PECS ZrB_2-20vol%SiC against SiC balls is significantly affected by the high temperature test condition. A reduction with a factor of up to ~ 2 on the friction level was observed in the test carried out at 1000°C.

Keywords

PECS ZrB_2-20%SiC, Coefficient of friction, High temperature, Ball-on-disc, SiC counterpart.

1. Introduction

In the last decades significant efforts have been addressed in the optimization of consolidation of materials. Ultra high temperature ceramics (UHTC) can be obtained employing pulsed electric current sintering (PECS) technique, by the combination of boride and carbide ceramic materials. UHTC are of great interest in aerospace industry for sharp leading edge applications, nose cones and engine cowls, see (Opeka et al. 2004). This advanced ceramic materials offer a unique properties combination of low density, compressive strength, high hardness, and high melting temperature (more than 3000°C). Based on a recent literature survey, most of the available information on ZrB_2-SiC ceramic composites is focused on processing and oxidation behaviour. It has been reported by (Rezaie et al. 2007) that ZrB_2 and SiC present negligible oxidation rates below 800 °C. At temperatures between 800-1200°C, ZrB_2 will oxidize in molten B_2O_3 and

solid ZrO_2 (see Reaction 1), whereas, SiC remains unoxidized. At higher temperatures above ~1200 °C, the oxidation of SiC will lead to molten SiO_2 and CO (see Reaction 2), additionally, evaporation of the molten B_2O_3 is expected (see Reaction 3).

$$2ZrB_2 + 5O_2(g) \rightarrow 2ZrO_2 + 2B_2O_3(l) \tag{1}$$

$$2SiC + 3O_2(g) \rightarrow 2SiO_2(l) + 2CO(g) \tag{2}$$

$$B_2O_3(l) \rightarrow B_2O_3(g) \tag{3}$$
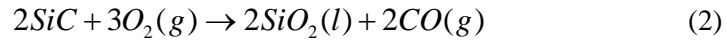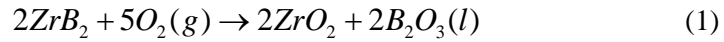
However, there is a lack of knowledge on the correlations between oxidation behaviour and friction response of such PECS ZrB₂-20vol%SiC advanced ceramics. Having understood the frictional response and surface transformation at high operating temperatures (up to 1000 °C) of UHTC will contribute to advances in material selection and design of components. This paper investigates the dry sliding friction and wear response of ZrB₂-20vol%SiC against SiC balls at room (25°C) and high temperature (1000 °C). The experiments were performed using a ball on disc configuration with a maximum Hertzian contact pressure of 2.5 GPa and a speed of 0.3 m/s. Worn surface morphologies were investigated by visual inspection and photomacrography.

2. Experimental

Materials
ZrB₂-20vol%SiC ceramic composite was developed by the MTM and PMA research partners of the Catholic University of Leuven (KU Leuven) without any additives by means of pulsed electric current sintering (PECS). Further information on its processing technique and characterization can be found elsewhere (Malek et al. 2013). Commercial available SiC balls were chosen as static counterpart. Properties of ZrB₂-20vol%SiC disc specimens and SiC ball counterparts are summarized in Table 1.

Disc specimens of ZrB₂-20vol%SiC were machined and surface finished by grinding and polishing to final dimensions of 40 mm diameter and 4 mm thickness. The grinding operation was executed using JF415DS grinding equipment (Jung, Göppingen, Germany) by means of a diamond abrasive wheel (type MD4075B55, Wendt Boart, Brussels, Belgium) with wheel diameter of 200 mm, average abrasive grain size of 54 µm, wheel speed of 22 m/s, table speed of 12 m/min and cutting depth of 10 µm. The polished surface finish was obtained using two consecutive polishing steps. The first step was performed using a Struers MD-Allegro 250 mm grinding disc with a 9 µm grade diamond paste, followed by a final step using a Struers MD-Dur 250 mm polishing cloth with 3 µm grade diamond paste. Both steps were performed with a load of 75 N and a rotational speed of 150 rpm during 10 minutes.

Surface roughness of ZrB_2-20vol%SiC discs was measured at 4 different locations (with 15 mm offset at every 90 ° in the radial direction) with the surface topography scanning equipment (Somicronic® EMS Surfascan 3D, type SM3, needle type ST305) using a cut-off wavelength $\lambda_c = 0.08$ mm, and a sampling length $l_m = 0.4$ mm. The surface roughness of the SiC balls was measured using a cut-off wavelength λ_c and sampling length l_m of 0.25 mm and 1.25 mm. The selection criterion for the λ_c and l_m was based on DIN 4768 and ISO 4288 standards. The roughness levels R_a and R_t of ZrB_2-20vol%SiC discs and SiC balls are also found in Table 1.

Table 1. Properties ZrB_2-20vol%SiC discs and SiC balls.

Material properties	ZrB_2-20vol%SiC	SiC
Density [g/cm³]	5.51	3.10
HV_1 [kg/mm²]	2004 ± 51	2806 ± 150
$K_{IC(1kg)}$ [MPa.m$^{1/2}$]	4.1 ± 0.6	2.7 ± 0.2
E-modulus [GPa]	488 ± 3.5	410
Poisson ratio [-]	0.148	0.140
Average Boride grain size [µm]	3.00	-
Average Carbide grain size [µm]	1.00	< 8.00
R_a [µm]	0.017 ± 0.004	0.035 ± 0.020
R_t [µm]	0.123 ± 0.044	0.216 ± 0.106

Tribological characterization

Wear tests were carried out at temperatures of 25 and 1000 °C employing a ball-on-disc high (point contact) temperature tribometer (CSM Switzerland). The tests were performed according to the ASTM G99-95a standard under atmospheric conditions with relative humidity (RH) 40 ± 5 %, maximum Hertzian contact pressure of 2.5 GPa (using 10 N load), sliding speed of 0.3 m/s and a total sliding distance of 150 m. SiC balls were used as static counterpart with a radius of 2.5 mm. The Vickers hardness ratio balls/specimens ~ 1.4.

3. Results and discussion

Friction behaviour

Fig. 1 shows typical curves of the coefficient of friction of ZrB_2-20vol%SiC ceramic specimens against SiC balls at 25 and 1000 °C for 150 m at a sliding speed of 0.3 m/s. At first, the coefficient of friction at the room temperature test exhibits a sharp increase to approximately 0.85 throughout the first meters of

sliding (this can be explained in terms of initial breaking of asperities) and, subsequently, decreases and evolves to a value of about 0.70 towards the end of the test. Finally, the coefficient of friction of the test performed at 1000 °C is initially ~ 0.4 but increases with sliding distance to a value of ~ 0.60 and, suddenly, decreases to a value around 0.40 and keeps fluctuating for more than ~ 80 m. This can be attributed to the presence of oxidized products in the surface at the sliding contact and will be further discussed.

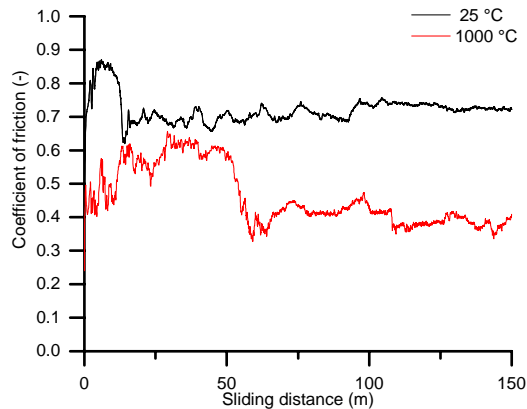*Figure 1.* Coefficient of friction versus the sliding distance and temperature
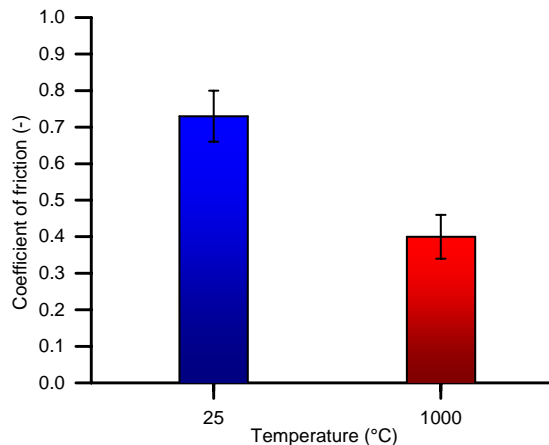(p = 2.5 GPa, v = 0.3 m/s).

Figure 2. Influence of temperature on the coefficient of friction
of polished ZrB2-20vol%SiC against SiC (p = 2.5 GPa, v = 0.3 m/s).

Fig. 2 shows the mean values of dynamic friction coefficient of polished ZrB$_2$-20vol%SiC in sliding contact against SiC applying a Hertzian contact

pressure of 2.5 GPa, a sliding distance of 150 m, a sliding speed of 0.3 m/s and temperatures of 25 and 1000 °C. Each reported value of the coefficient of friction is an average of at least 3 wear experiments performed under identical conditions for the last 75 m of sliding distance (steady-state), with 2 times standard deviation less than +/- 10 % and +/- 15 % for the room and high temperature experiments, respectively.

A significant reduction on the coefficient of friction with approximately a factor of 2 can be observed at 1000°C. The reduction in the coefficient of friction can be attributed to the presence of liquid boron oxide B_2O_3 (which starts to melt at approximately 450 °C), solid ZrO_2 and SiO_2 under the ball on disc contact, these oxides were reported by (Rezaie et al. 2007) as product of the oxidation of ZrB_2-SiC ceramic composites. Similar observations on reduction on the coefficient due to formation of oxide films (liquid and solid) on the surfaces has been reported by researches in monolithic ZrB_2, TiB_2 and TiN-TiB_2 ceramic composites, see (Tkachenko et al. 1984), (Senda et al. 1993) and (Yang et al. 2010).

It is well known that coefficient of friction is proportional to the critical shear stress of the interface, see Equation (4). In general, the critical shear stress of a formed oxide in the interface is lower than that one associated to the bulk. In other words, the formed solid rutile ZrO_2 and or SiO_2 possesses considerably much lower shear stress than the bulk, and it is also considered to be the responsible of the reduction on the coefficient of friction for the test evaluated at 1000 °C.

$$\mu \sim \tau_{\text{int}\,erface} \tag{4}$$

It is worth nothing that similar expression to the Equation (1) has been used in the literature for the understanding the high-temperature-lubricated effect of TiN-TiB_2 and Si_3N_4 based composites, see (Yang et al. 2010) and (Liu et al. 1993).

Worn surface morphologies
Post-mortem analysis of ZrB_2-20vol%SiC discs was carried out by means of photomacrography. At room temperature, visual inspections of worn surfaces after wear tests revealed the occurrence of wear debris particles, mainly located in the outer extensions of the wear track (referred as WT in Fig. 3), but also inside, along and adjacent to the wear scar. Moreover, adhesion of such particles and abrasion scratch marks are found and referred as ADH and ABR, respectively, in Fig. 3 (a). At high temperature tests (1000 °C), see Fig. 3 (b), the presence of re-solidified oxide liquid and/or oxide layer (referred as OL) after wear experiments can be evidenced over all the surface of the disc. Additionally, a kind of glassy/vitreous phase (referred as GP) can also be observed at the worn track, either by visual inspection or macrography. However, the precise nature of the oxidized surface and sub-surface at the interface of a sliding contact needs to be further investigated by means of scanning electron microscopy (SEM) coupled to energy dispersive X-ray (EDX) spectroscopy (point and mapping

analysis), XRD measurements and focused ion beam (FIB) for milling and imaging of sub-surface morphologies, for instance.
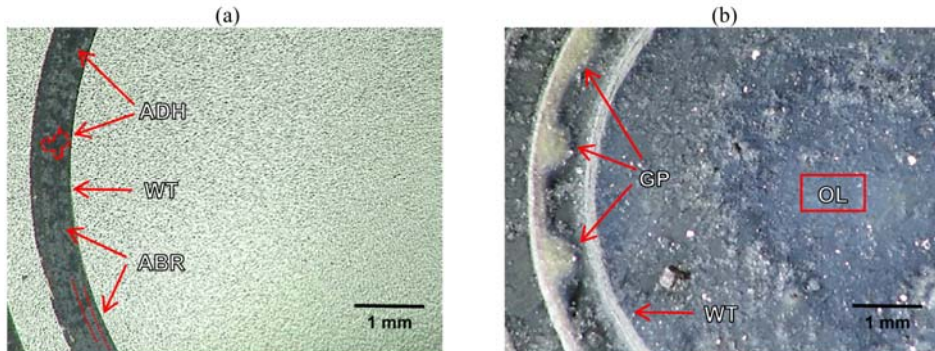

Figure 3. Macrograph of wear track of PECS ZrB$_2$-20vol%SiC
after sliding against SiC ball at: (a) 25 °C and
(b) 1000 °C (p = 2.5 GPa, v = 0.3 m/s).

Conclusions

Rotating ball-on-disc experiments on ZrB$_2$-20vol%SiC ceramic composites surface finished by polishing slid against SiC balls under a constant Hertzian pressure of 2.5 GPa and speed of 0.3 m/s at room temperature and at 1000 °C revealed that the friction response is significantly affected by the high temperature ambient conditions. The coefficient of friction was measured to vary within 0.73 ± 10 % and 0.40 ± 15 %, both within 95 % confidence interval, for tests performed on ZrB$_2$-20vol%SiC at 25 and 1000 °C, respectively. A friction reduction with a factor ~ 2 in friction coefficient can be observed at 1000 °C compared to room temperature (p = 2.5 GPa, v = 0.3 m/s). This high-temperature friction response can be attributed to the surface oxidation and the formation of liquid B$_2$O$_3$, solid ZrO$_2$ and/or SiO$_2$.The generated wear particles and the oxide compound layer and sub-surface in the wear track must be examined more in-depth in a near future investigation by means of FIB-SEM, EDX mapping and XRD measurements. Moreover, metallic static counterparts will be also implemented.

Nomenclature

μ	Coefficient of friction	-
$\tau_{\text{int }erface}$	Shear stress of the interface	MPa
p	Hertzian contact pressure	GPa
v	Sliding speed	m/s

Acknowledgements

References

[1] Liu, H., M. E. Fine, H. S. Cheng and A. L. Geiger (1993). "Lubricated Rolling and Sliding Wear of a SiC-Whisker-Reinforced Si3N4 Composite against M2 Tool Steel". Journal of the American Ceramic Society 76(1): 105-112.

[2] Malek, O., J. Vleugels, K. Vanmeensel, W. Van Renterghem and B. Lauwers (2013). "Electrical Discharge Machining of (Nb$_x$Zr$_{1-x}$)B$_2$-SiC Composites". Procedia CIRP 6(1): 186-191.

[3] Opeka, M. M., I. G. Talmy and J. A. Zaykoski (2004). "Oxidation-based materials selection for 2000°C + hypersonic aerosurfaces: Theoretical considerations and historical experience". Journal of Materials Science 39(19): 5887-5904.

[4] Rezaie, A., W. G. Fahrenholtz and G. E. Hilmas (2007). "Evolution of structure during the oxidation of zirconium diboride–silicon carbide in air up to 1500 °C". Journal of the European Ceramic Society 27(6): 2495-2501.

[5] Senda, T., Y. Yamamoto and Y. Ochi (1993). "Friction and wear test of titanium boride ceramics at elevated temperatures". Journal of the Ceramic Society of Japan 101(1172): 451-455.

[6] Tkachenko, Y. G., V. K. Yulyugin, G. A. Bovkun and D. Z. Yurchenko (1984). "High-temperature friction of borides of group IV–VI metals". Soviet Powder Metallurgy and Metal Ceramics 23(1): 85-88.

[7] Yang, Z.-L., J.-H. Ouyang, Z.-G. Liu and X.-S. Liang (2010). "Wear mechanisms of TiN–TiB$_2$ ceramic in sliding against alumina from room temperature to 700 °C". Ceramics International 36(7): 2129-2135.

Evaluation of results of measuring roundness with two-factor analysis of variance

Imre NÉMEDI[1], Miodrag HADŽISTEVIĆ[2], Janko HODOLIČ[2],
Milenko SEKULIĆ[2]

[1]Polytechnical College of Subotica,
[2]University of Novi Sad, Faculty of Technical Sciences

Abstract

Under contemporary conditions of the manufacturing process of parts and assembly the accuracy of production is of great significance. Accuracy does not refer only to dimensional but also to geometric precision. These characteristics are imposed by tolerance in dimension and form.

This paper treats a control analysis of a geometric property: roundness.

Measurements are done on a contemporary CNC controlled coordinate measuring machine using different conditions of measurement.

In the paper two-factor analysis of the variance belonging to method ANOVA is compared to the influences of qualitative variables.

Keywords

roundness, CMM, measuring, ANOVA method.

1. Introduction

A work piece from dimensions all work pieces have certain micro and macro geometrical surface characteristics [1]. For deviation from dimension and macro geometrical characteristics of form, location, and direction there are functional limitation which, if they are overstepped, this may endanger the functionality of the work piece. The tolerances on the drawings (PLANS, DESIGNS) have to completely ensure the dimensions and geometrical form, so that nothing is left to subjective evaluation of the factory staff or the control service.

The forms of the real surfaces regularly have a certain degree of deviation in comparison to the geometrically ideal surfaces. The causes of deviation basically match with the causes of inaccuracy of measuring work pieces. Functional dimensions are always done with a certain degree of tolerance that simultaneously limit the form deviation of that work piece. [3]

If one needs a greater degree of precision, than the one provided by the tolerance level formed by the tolerance of longitudinal dimensions, then the form must be separately tolerated. All this is true for location between two or more surfaces. The exceptions for this are: symmetricity and coaxiallity, as well

as precision of rotation, as they are independent of real dimensions, but they are determined in relation to the central plain and the axis.

Geometrical tolerances are determined only when necessary from the aspect of functional requirements, changeability and eventually from the aspect of production. However, this does not mean automatically that a special way of manufacture, measuring or control has to be used. One specific version of form tolerance is analyzed in this paper, namely roundness.

1.1 Definition of tolerance of roundness
The field of roundness tolerance in the regarded plain is restricted by two concentric circles on the distance *t*. (fig. 1)

If the section lines are tolerated, then all section points must lie between two concentric circles on the section plain, on a radial distance of *t*. This parameter *t* is the value of tolerance of roundness.
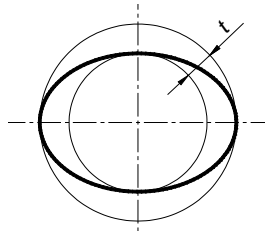
Figure 1. Definition of tolerance of roundness [2]

1.2 Possible form of deviation from roundness
Irregularities on the section of round machining bodies, including both the axis and openings are most often realized in: a) triangular, b) oval, c) multiangle, or d) eccentric forms. These irregularities of forms depend on number exterior effects, primarily on rigidity and a way of clamping [5].

Thus, for example, a triangular form of irregularity is mostly achieved with thin-walled pipes, if the clamping is done in three points. This means that with roundness control of such an work piece the appearance of a triangular form can be expected in advance. This is significant, because with classical ways of roundness control not all types of deviance can be measured. The most probable form of irregularity has to be assumed in advance.

Figure 2 provides a review of the most common roundness errors.

Figure 2. Possible versions of form irregularity of work pieces in cross section [2,4]

2. Measurements

2.1 Presenting of the used measurement machine

The measurement has taken place on an up-to-date directed coordinate measuring machine, produce of the firm DEA Hexagon Metrology, in the laboratory of Szent István University in Gödöllő. The technical characteristics of the measuring machine are the following:
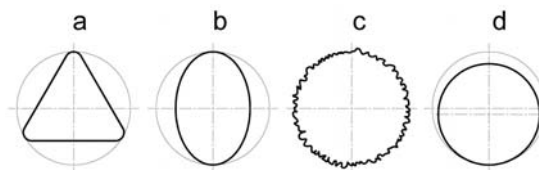
- the workspace of the machine (length x width x height) – 1000 x 700 x 600 mm,
- pneumatic bearing of the moving elements in the mechanism,
- measuring uncertainty (MPE$_E$): (0,9 + L/350) μm, where L is the length in mm,
- automatic compensation of the temperature for all kinas of steel between $19^o – 21^o$,
- maximal speed of the sensor's displacement (v_{max}): 520 mm/sec,
- maximal acceleration of the sensor's displacement (a_{max}): 3300 mm/sec^2,
- software machines: Quindos 7.

Measurements are carried out in five different places (locations) on the table, with the aim to exclude eventual errors which may have occurred due to an inaccurate motion mechanism of the carrier construction of the measuring machine. The locations are presented in Fig. 3.
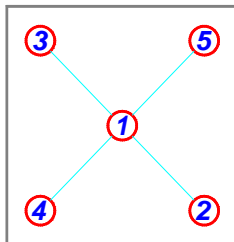
Figure 3. Setup of the measurement places
on the machine table [2]

The measurements are effectuated in all measuring positions with different numbers of measuring points. These numbers are: 310, 1150 and 2250. Each measurement is repeated three times in every measuring position. Out of the measuring data of importance are the widths of the tolerant fields of roundness. Table 1 presents the obtained results of these measurements.

2.2 Presenting of the used measurement workpiece

As measuring objects machine parts and measuring and control elements were used with outer and inner measuring surfaces. Out of that family of objects a master ring was chosen, the diameter of the hole 30 mm, made of high quality, heat-treated and polihed steel.

3. Presenting of the measurements results

Alter having done every measurement, the measuring machine produced a summary of the results. That survey was given in diagrams and tables. Picture 4 illustrates characteristic diagrammatic presentations from all the five measuring places in form of circuit diagrams.

| 1. | 2. | 3. | 4. | 5. |
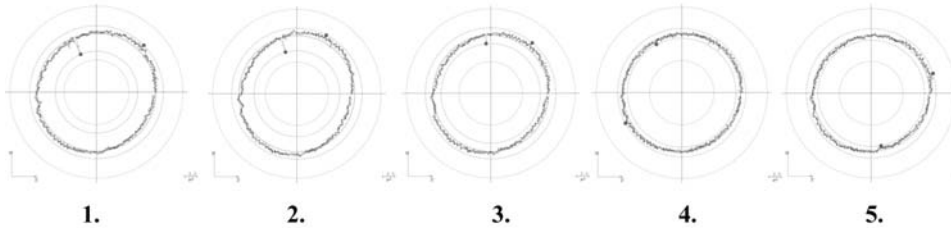
From the table of results at this place only relevant data appear about the most essential element – the dimension of the width of the field of roundness. (Table 1.) Measuring places are considered as factor A (a=5), while the different numbers of measuring points factor B (b=3).

Table 1. Width of the field of roundness in mm

factorA factorB	Measuring place *1*	Measuring place *2*	Measuring place *3*	Measuring place *4*	Measuring place *5*
	0,0055	0,0046	0,0043	0,0020	0,0021
Number of meas. points 310	0,0042	0,0034	0,0040	0,0031	0,0022
	0,0050	0,0041	0,0034	0,0022	0,0035
	0,0057	0,0039	0,0033	0,0035	0,0022
Number of meas. points 1150	0,0051	0,0045	0,0031	0,0022	0,0036
	0,0040	0,0040	0,0042	0,0018	0,0020
	0,0056	0,0044	0,0031	0,0033	0,0022
Number of meas. points 2250	0,0051	0,0041	0,0041	0,0030	0,0037
	0,0043	0,0035	0,0036	0,0021	0,0020

Considering the results, there is a rather significant dissipation of values, so we may wonder why it is so. The aim of the result-evaluation of the measurement of roundness is determining the influence of the measuring place on the table of the measuring machine and the number of the measuring points on the accuracy of the measurement in the same way as their mutual influence.

4. The use of two-factor analysis of variance

At the beginning of the analysis some hypotheses may emerge from behind factor A, factor B and their interaction AB (possible influence of the number of the measuring points onto the measuring place).

Hypotheses:

Factor A:

- H_0: various measuring places on the table of the measuring machine have identical influence on the measurement of roundness,
- H_1: at least one measuring place on the table of the measuring machine influences differently the results of the measurement of roundness.

Factor B:

- H_0: different numbers of measuring points have identical influence on the measurement of roundness,
- H_1: at least one number of measuring points influences differently the results of the measurement of roundness.

Interaction between Factors A and B:

- H_0: the number of measuring points does not influence the measuring place,
- H_1: at least one of the numbers of measuring points influences the measuring place.

A rouge table is to be composed as it is shown by table 2.

Table 2. Rough Table

		Measuring place - **factor A**					
		Measuring place *1*	Measuring place *2*	Measuring place *3*	Measuring place *4*	Measuring place *5*	Σ
Number of measuring points - **factor B**	Number of meas. points 310	n=3 Σy=0,01 47 y=0,004 9	n=3 Σy=0,01 21 y=0,004 03	n=3 Σy=0,01 17 y=0,003 9	n=3 Σy=0,00 73 y=0,002 43	n=3 Σy=0,00 78 y=0,002 6	n=15 Σy=0,05 36 y=0,003 57
	Number of meas. points 1150	n=3 Σy=0,01 48 y=0,004 93	n=3 Σy=0,01 24 y=0,004 13	n=3 Σy=0,01 06 y=0,003 53	n=3 Σy=0,00 75 y=0,002 5	n=3 Σy=0,00 78 y=0,002 6	n=15 Σy=0,05 31 y=0,003 54
	Number of meas. points 2250	n=3 Σy=0,01 5 y=0,005	n=3 Σy=0,01 2 y=0,004	n=3 Σy=0,01 08 y=0,003 6	n=3 Σy=0,00 84 y=0,002 8	n=3 Σy=0,00 79 y=0,002 63	n=15 Σy=0,05 41 y=0,003 61
	Σ	n=9 Σy=0,04 45 y=0,004 94	n=9 Σy=0,03 65 y=0,004 06	n=9 Σy=0,03 31 y=0,003 68	n=9 Σy=0,02 32 y=0,002 58	n=9 Σy=0,02 35 y=0,002 61	Σn=45 Σy=0,16 08 y=0,003 57

On the basis of the data from the rough table first the sums of squares are calculated, in fact the variation among groups SS_M, variation inside groups SS_E and the summing up variation SS_T, in the same way as the variation of the factors SS_A, factors SS_B and the interaction of the factors SS_{AB}. Later the degrees of freedom are determined. Finally quadratic mean (variances) are calculated, variances of factor A – MS_A, variances of factor B – MS_B, variances of interaction of factors MS_{AB}, variances inside the group MS_E and all the variances MS_T.

The results of the calculations are presented in table 3.

Table 3. Table of the results

	DF	SS	MS	F_0	P
Factor A	4	0,0000363636	0,0000090909	19,9362	<0,05
Factor B	2	0,0000000333	0,0000000167	0,0365	
Interactions AB	8	0,0000004711	0,0000000589	0,1291	
Rest (error)	30	0,0000136800	0,0000004560		
Total	44	0,0000505480			

For interpreting the acquired values we use the table of limits F distribution – Snedecor's distribution. In this case a distribution with 95% reliability (α=0,05) was used.

$$F_{A(a-1,\Sigma n-1),a}=F_{(4,44),0,05} = 2,61 \tag{1}$$

$$F_{B(b-1,\Sigma n-1),a}=F_{(2,44),0,05} = 3,23 \tag{2}$$

$$F_{AB((a-1)(b-1),\Sigma n-1),a}=F_{(8,44),0,05} = 2,18 \tag{3}$$

Conclusion

Relying upon these findings we can conclude the following:

The acquired results point out that the hypothesis H_0 on the level of significance α=0,05 can be discarded, which means that different measuring places on the table of the machine do not influence equally the measured roundness, in fact the place of the measurement on the table is the most important factor. The numbers of the measuring points and the interaction have not any influence on the value of roundness. But by means of this method we cannot determine the reason of the measuring places influence. It must be the theme of some other analysis.

Acknowledgement

methods and approaches in manufacturing of dental recoveries with the application of modern technologies and computer aided systems" – TR 035020, financed by the Ministry of Science and Technological Development of the Republic of Serbia.

References

[1] Fledrich G., Pálinkás I., Keresztes R., Szabadi L., Kalácska G.:Turning of zirconium-dioxide ceramics. Mechanical Engineering Letters. 2011. Vol.5. pp 44-57.

[2] Nemedi, I., Hadžistević, M., Hodolič, J.: Results of measuring roundness on the coordinate measuring machines, Seria C, Volumul XXIII, Scientific Bulletin, Fascicle: Mechanics, Tribology, Machine Manufacturing Technology, Editura Universitatii de Nord din Baia Mare, 2009., pp 129-136., ISSN 1224-3264

[3] Stević, M.: Povećanje tačnosti merenja numerički upravljanih mernih mašina, monografija, Fakultet tehničkih nauka, FTN Izdavaštvo, Novi Sad, 2006.

[4] Szilágyi, L.: Gépipari hosszmérések, Ipari szakkönyvtár, Műszaki Könyv-kiadó, Budapest, 1982.

[5] Gadelmawla, E.S.: Simple and efficient algorithms for roundness evaluation from the coordinate measurement data, Measurement, Volume 43, Issue 2, February 2010, Pages 223-235.

Pneumatic cylinder positioning system realised by using on-off solenoid valves

László FÖLDI, Zoltán BÉRES, Eszter SÁRKÖZI

Institute for Mechanical Engineering Technology,
Faculty of Mechanical Engineering
Szent István University, Gödöllő,

Abstract

This paper presents a novel control design, developed to realise fast and accurate position control of a pneumatic actuator using inexpensive on/off solenoid valves. In contrast to conventional control methods, the proposed control method operates chatter free, based on air compression. The control principle was developed by investigating the dynamics of a pneumatic actuator with an identified mathematical model. This new approach is applied to a pneumatic double acting cylinder, controlled by a pair of 5/3 way directional single solenoid valves. The described closed-loop circuit copes with the discontinuities associated with the valve's switching dynamics, and relatively long response time. The experimental apparatus uses an analogue displacement encoder for metering the piston's position and velocity, and doesn't incorporate pressure sensors thus ensuring a low cost system design. The results of experiments with various step responses show that the proposed control method performs well. The measured steady-state position errors are equal to the used potentiometer's travel resolution, which is 0,01 mm. Therefore this novel control and the related pneumatic system design could be a cost effective alternative to the servo-pneumatic positioning systems.

Keywords

Position Control, Solenoid Valve, Pneumatic Cylinder, Control Method, Actuator

1. Introduction

In order to achieve linear motion, pneumatic, electromagnetic and hydraulic actuators are typically used. Due to their advantageous characteristics in position control applications the latter two are more widespread. Though using hydraulic actuators high velocity and great force is achievable, and their position control can also be relatively easily solved, a handicap is that the leaking of hydraulic fluids might contaminate the workpiece. Electromagnetic actuators on the other hand are clean and reliable in their operation but often require a mechanical

transmission, both to convert high speed and low torque to a more useful combination and to convert rotary motion to linear motion. While linear motors overcome the need for transmission, they can be expensive [9].

Pneumatic actuators have several advantages: they are fast, cheap, have an outstanding power-to-weight ratio, are easily maintainable and they don't contaminate the work piece. The challenge to the use of pneumatic drives is that due to piston friction and the characteristics of compressed gas flow their behaviour is non-linear. As a result their industrial use is only widespread in applications which require linear motions between end positions.
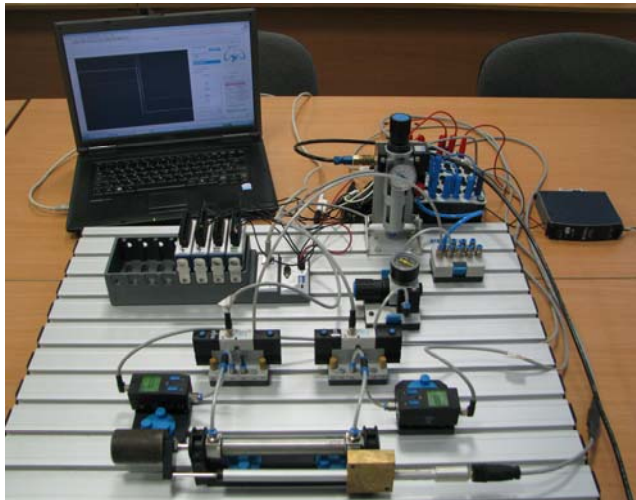
Figure 1. The experiment apparatus

In the last decade such industrial controllers became available which have adequate computing capacity for real-time usage. Thus there is now opportunity to develop pneumatic systems which don't require costly proportional valves for positioning and hence the usage of the more cost-efficient solenoid valves became possible (Figure 1.). These simple on/off valves are cheap and easily maintainable. Their drawback however is that as yet the required control method is not appropriately elaborate: the solutions offered in the scarce publications on the topic consist of applying conventional control methods (PID, sliding mode, fuzzy logic) or their hybrid versions, with varying success.

A review of the papers on the topic is given in Table 1, where the applied control methods, the number of required valves and the highest positioning accuracy is shown. Even though it is not indicated in the table, in some cases certain speed or force decreasing solutions (eg. throttle valve, reduced pressure) were used, which naturally may have an effect on the operating range of the positioning system and the steady-state error. The employed valve's switching time is also omitted from the table.

Table 1. A review of the papers on the topic

Number in References	Authors	Control method	Number of required valves	Positioning accuracy
[9]	Thomas, M.B.; Maul, G.P.; Jayawiyanto, E.	Modified PD + PWM control	3	±0,1 mm
[1]	Ahn, K.; Yokota, S.	MPWM + neural network (LVQNN)	8	±0,2 mm
[7]	Parnichkun, M.; Ngaecharoenkul, C.	hybrid of fuzzy and PID + PWM control	1	±3,5 mm
[6]	Nguyen, T.; Leavitt, J.; Jabbari, F.; Bobrow, J.E.	Sliding mode control	4	±0,1 mm
[8]	Shih, M.-C.; Ma, M.-A.	Fuzzy + modified differential PWM control	2 + Proportional pressure valve	±0,075 mm
[5]	Messina, A.; Giannoccaro, N.I.; Gentile, A.	Individual control + PWM	2	±0,1 mm
[3]	Barth, E.J.; Zhang, J.; Goldfarb M.	Individual linear continuous + PWM	2	N/A
[2]	Akdağ, F.N.; Kuzucu, A.	Sliding mode control	2	±0,05 mm
[10]	van Varseveld, R.B.; Bone, G.M.	PID with friction compensation + PWM	2	±0,21 mm

2. Control method

Designing the control method we determined to apply two solenoid valves (one for each chamber), the biggest benefit of which is that the number of control signals is thus raised to the second power.

Table 1. Available variations using two solenoid valves

Number of variation	Signal of solenoid valve 1	Signal of solenoid valve 2	Movement of the cylinder piston
1	fill	empty	positive direction, fast
2	fill	close	positive direction, slow
3	fill	fill	immobile
4	close	empty	positive direction, uncontrolled
5	close	close	first immobile, then uncontrolled
6	close	fill	negative direction, slow
7	empty	empty	accidental direction, uncontrolled
8	empty	close	negative direction, uncontrolled
9	empty	fill	negative direction, fast

Out of the variations presented in Table 2, we ignored the uncontrolled ones (where pressure in both chambers changes in an uncontrolled way) which thus leaves us with five useful solenoid valve variations. However, in order to stop the movement of the cylinder piston in variation number 3, a complementary element had to be introduced (due to the asymmetric construction of the cylinder we used). Using a pressure regulator, the positive chamber was filled with supply pressure decreased in proportion to the surfaces of the piston.

As a first step we started out from a graph representation, where time and position were placed on the axes. This way the most important control parameter, the error (difference between a measured process variable and a desired set-point) can be visualized easily if we represent both the ideal and the actual position values (reference signal and measured output respectively) plotted against the elapsed time.

Based on the scale of the error we might form predictions as to which valve variation has to be realized by the control method in order to decrease the absolute value of the error.

Table 2. Realized valve variations

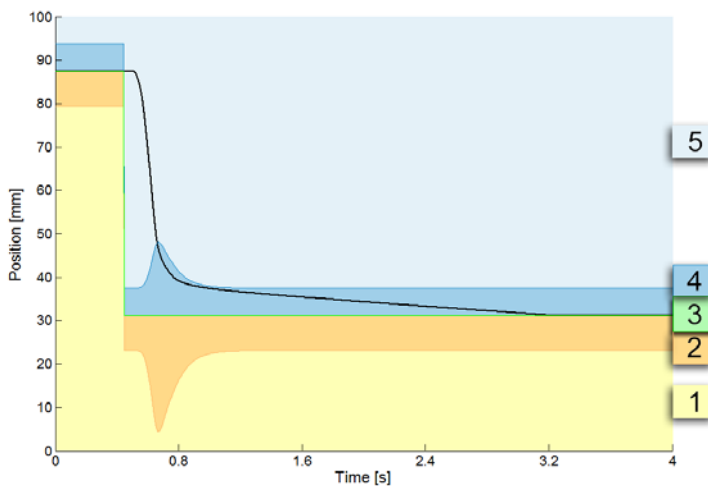| Number of control signal	Relation between reference signal and measured output	Desired piston movement	Number of variation in Table 2
1	$r \gg y_m$	positive direction, fast	1
2	$r > y_m$	positive direction, slow	2
3	$r \approx y_m$	immobile	3
4	$r < y_m$	negative direction, slow	6
5	$r \ll y_m$	negative direction, fast	9

Figure 2. Control Strategy

The variations in Table 3 can be easily indicated in the graph representation we have already created (Figure 2.), since control signal number 3 has to take effect within the close vicinity of the ideal position, namely in a predefined tolerance band where further changing of position is unnecessary. Nearby, above and below this band we can assign the zones where the piston is relatively close to the ideal position, thus slow movement is required (control signals number 2 and 4). Outside these bands those parts of the stroke length are situated which are relatively far from the ideal position, hence a fast piston movement is needed in order for a fast decrease in the absolute value of the error to take place (control signals number 1 and 5). Since the width of the tolerance band is a parameter given during utilization, the control method only has to determine the width of bands number 2 and 4 in a given moment. By rendering the respective valve variations to the given bands, the solenoid valves can be controlled harmoniously and in an essentially discrete way, with few valve switches, i.e. chatter free.

In order to determine the width of the bands we can set up the following equation based on the work-energy theorem:

$$0 - \frac{1}{2} \cdot m \cdot v^2 = -(\frac{p_b \cdot A \cdot (q+z)}{R \cdot T} \cdot R \cdot T \cdot \ln \frac{p_a}{p_b}) \qquad (1)$$

Of the terms of the equation p_a and p_b are the initial and final pressures of the closed chamber, q is the distance needed to stop the piston while z is the remaining distance. Setting up the equation we regarded the process to be isothermal, thus we overestimated the necessary distance to stop the piston, this way compensating for the losses which appear in the positioning system.

After reducing the values regarded as constants and expressing q from the equation, we come to the following relation:

$$q = c_2 \cdot v^2 - z \qquad (2)$$

The equation shows that the ideal deceleration distance of the piston (q) changes according to a second-degree function of piston speed. It follows that the widths of the deceleration bands of the piston have to be adjusted in a given moment proportional to the square of the measured output's first derivative; at this point a proportional coefficient (c_2) has to be introduced. Furthermore, it is also necessary to set a constant c_1 bandwidth which guarantees the slow movement near the ideal value.

As the next step, we have to assign the adequate control signs to the bands. This is done in a similar way to the operation of a relay, by sign functions, which decide whether the piston's measured output is below or above the band limit set. Summing up the values of these sign functions we arrive at 4 discrete numeric values which unequivocally determine which band the measured output falls into (e.g. we get -3 if it is below all band limits, i.e. in band number 1). By

assigning the adequate control signs to these numeric values and to the tolerance band around the ideal position we achieve a control method which satisfies the criteria set.

In accordance with notations of control engineering, the mathematical description of the control method is as follows: r stands for the reference signal, while ym is the measured output, t means tolerance and F;C;E are respectively the filling, closing and emptying switch states of the first and second solenoid valves:

$$sign\left\{y_m - \left[r - (c_1 + c_2 \cdot (\dot{y}_m)^2)\right]\right\} + sign\,(y_m - r) + sign\left\{y_m - \left[r + (c_3 + c_4 \cdot (\dot{y}_m)^2)\right]\right\} = k$$

$$if\ |y_m - r| < t,\ then \qquad \Rightarrow \qquad cont = [F;F]$$

$$if\ |y_m - r| > t,\ then \begin{cases} if\ k = -3 \Rightarrow cont = [F;E] \\ if\ k = -1 \Rightarrow cont = [F;C] \\ if\ k = 1 \ \Rightarrow cont = [C;F] \\ if\ k = 3 \ \Rightarrow cont = [E;F] \end{cases}$$

(3)

The constants c3 and c4 figuring in the equation have the same function as the already known c1 and c2 constants; their introduction into the equation is necessary because of the asymmetric setting options which reflect the asymmetry of the cylinder.

The behaviour of the system is calculable and compared to the examples in the specialized literature the command signal operates at a lower frequency; thus, due to the smaller amount of gas let into the environment the efficiency of the overall system is increased. It is worth noting that the system is capable of adjusting itself to the reference signal even if per chance we have chosen too high parameters at the control settings. In this case the balance of force required to stop the cylinder piston sets in earlier than necessary, but since we only fill one of the chambers (see bands number 2 and 4) in the other chamber the pressure will slowly decrease, which is a consequence of the ever-present cylinder loss. The force arising from this pressure difference will always slowly move the piston to its ideal position. This is advantageous because this way, as far as the positioning systems most significant quality factor, the steady-state error is concerned, we can say that our system operates without predefined working-positions. Another great advantage is that in spite of the low frequency and delays of the solenoid valves we are able to make the piston stop with a high accuracy thanks to the slow movement around the reference signal.

3. Apparatus

The circuit diagram of the pneumatic positioning system is presented on figure number 5. As an actuator we applied a Festo DSNU-20-100-PPV-A P606 cylinder of 100mm stroke length, to which we attached a Festo MLO-POT-225-

LWG analogue displacement encoder, which has a 0,01 mm travel resolution. The applied encoder is a potentiometer which provides a voltage signal in proportion to the displacement. In order to move the cylinder we applied two Festo VSVA-B-P53C-H-A2-1R2L 5/3 way solenoid valves, but we only used one output connection each and the remaining output ports were plugged. We measured the mentioned solenoid valve's ON and OFF switching time at 6 bar supply pressure; in case of switching on it was 14 ms (Figure 3.) while at switching off 36 ms (Figure 4.).
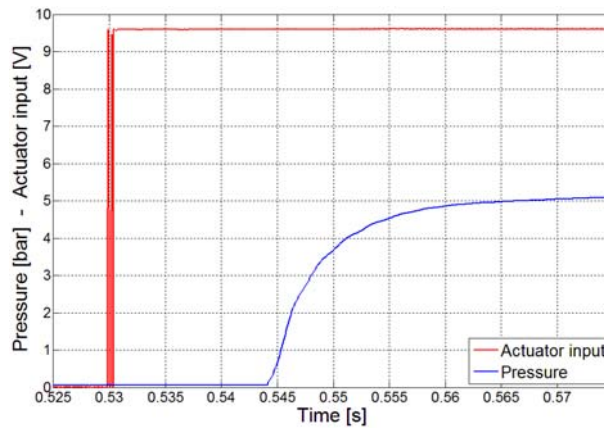

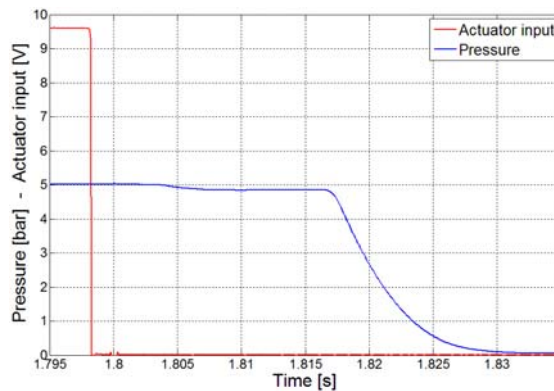*Figure 3.* Valve switching – On

Figure 4. Valve switching – Off

A further constituent is a Festo D:LR-1/8-0-MINI pressure regulator, and we also connected a Festo SDE1-D10-G2-H18-C-PU-M8 pressure sensor to both chambers to serve as feedback, which however we did not use in the control process in order to minimize the number of sensors necessary for the operation of the system. This system was constructed to test the planned control method

but by changing the different elements of the scheme, it can be freely scaled to achieve a faster operation or the movement of heavier loads.
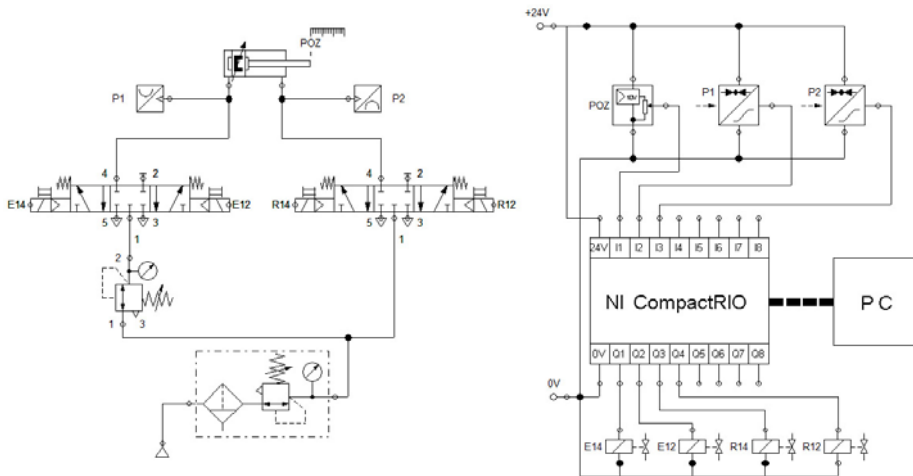

Figure 5. The circuit diagram of the pneumatic positioning system

The major elements of the electronic system are a 0-24 V direct current power supply (NI PS-15), an electronic instrument board (Festo), a NI CompactRIO™ (cRIO 9073) programmable automation controller and the already mentioned electro-pneumatic elements (displacement encoder, pressure sensors and solenoid valves). The applied NI CompactRIO™ programmable automation controller is a modular system; out of its modules we used the analogue-to-digital converter (NI 9201), for a dual purpose. On the one hand we applied it in the controlling process to measure the voltage signal (which is in proportion to the displacement) provided by the displacement encoder. On the other hand we used it in collecting data about the voltage signals corresponding to pressure values (expressed in bars) provided by the analogue pressure sensors. We controlled the two solenoid valves with the help of the digital output module (NI 9472). The communication between the CompactRIO™ and the computer was ensured by an Ethernet connection. We realised the real-time control based on equation number (8) by applying the FPGA module of CompactRIO™ programming it in the LabVIEW 2009 software. Due to the relative high prices of FPGA systems, later on it would be advisable to elaborate embedded DSP electronics developped for this purpose. [4].

4. Measurement results

The testing of the compiled system was done by determining the quality factors of the control method. During this process we have determined the settling time for

step responses from end positions, overshoots and steady-state error graphically based on measurement results. Under settling time we conventionally understand the time required for the measured output to finally reach the $\pm$ 5% vicinity of the reference signal.

The moved load was m=0.542 kg, the value of supply pressure in the case of the negative chamber was p2=6·105 Pa, and accordingly the decreased supply pressure of the positive chamber was $p_1 = \dfrac{A_2}{A_1} \cdot p_2 = 5,04 \cdot 10^5\, Pa$. The measurements were carried out at room temperature.

The control setting parameters were c1=18 [mm], c2=950 [-], c3=18 [mm], c4=250 [-]; based on previous experiences with the system the width of the tolerance band was set to be $\pm$ 0.025 mm, we regarded the position as adequate within this range.
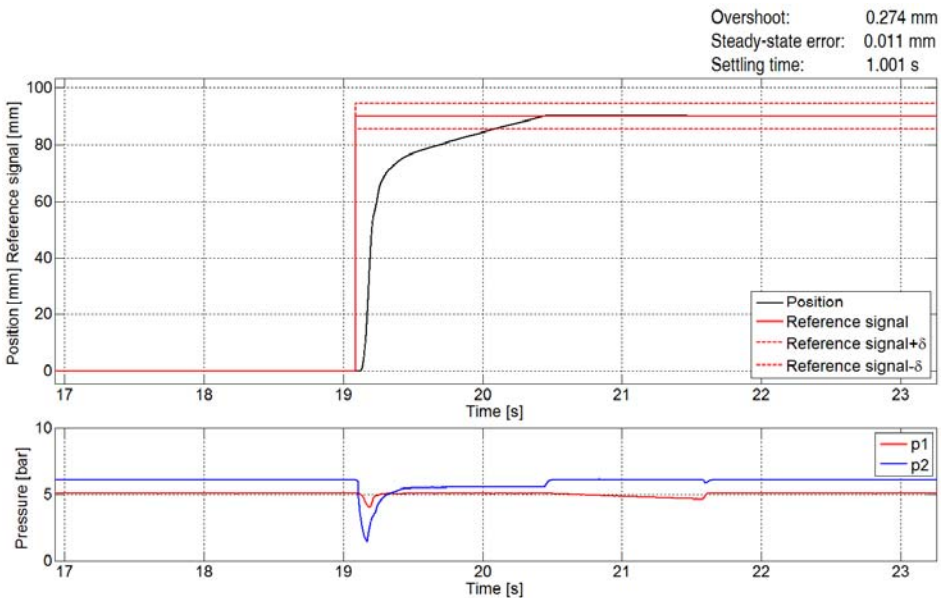

Figure 6. Step response – 0-90 mm

At the first measurement (Figure 6.) we have examined a displacement which is long compared to the stroke length of the cylinder by setting the reference signal at 90 mm. It is visible that in the case of large step size the control method is able to follow the dynamics of the cylinder, the overshoot is minimal while the settling time is 1 second. The steady-state error is again equivalent to the travel resolution of the displacement encoder.

After this we examined the movement of the piston in the negative direction, namely when it moves backwards into the cylinder.
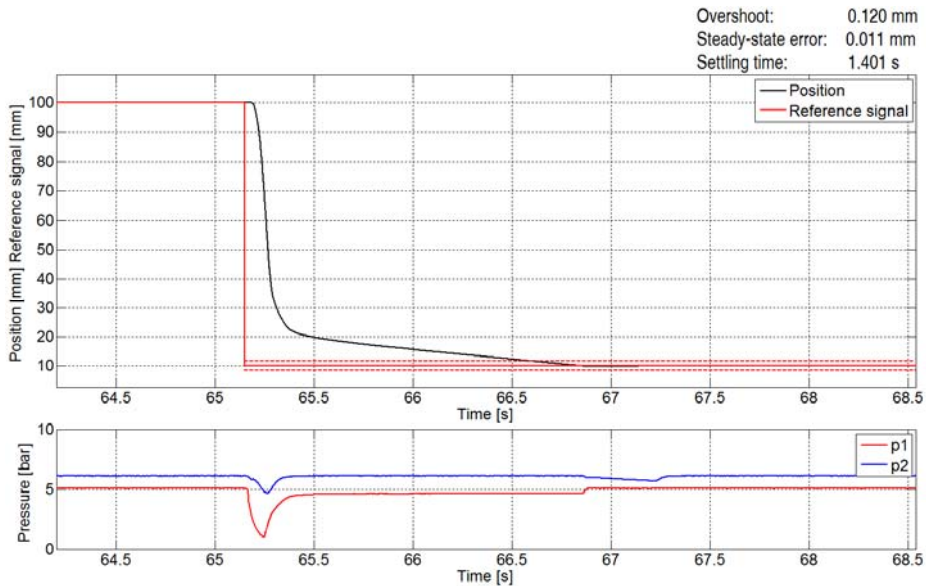
Figure 7. Step response – 100-10 mm

In the course of the fourth test at Figure 7. we can see a displacement similarly great to the previous experiment, but in the negative direction. The overshoot is minimal, and the settling time is still under 2 seconds. The steady-state error is once again equivalent to the resolution of the displacement encoder.

Conclusions

A novel control strategy and the according experimental apparatus to achieve accurate positioning of a pneumatic cylinder using solenoid valves is presented. The most significant features of this pneumatic positioning system are the following:
  – it substitutes the costly proportional valve with the conventional solenoid valve
  – thanks to a novel control design, the system operates in a chatter free way
  – the maximal operating velocity and force of the applied pneumatic actuator is not decreased
  – it contains the least amount of sensors and the least expensive electro-pneumatic elements possible

Thanks to all these, the system can achieve an adequately high positioning accuracy and reach a favourable price/value ratio at the same time. The paper also sheds light on the fact that the system's steady-sate error is highly dependent on the displacement encoder's travel resolution. This holds out the promise that the application of more advanced technology in the area (e.g. using

digital sensor with higher travel resolution, or a fast-switching solenoid valve to reduce the overshoot) will further improve the system's positioning accuracy.

References

[1] Ahn, K., Yokota, S., Intelligent switching control of pneumatic actuator using on/off solenoid valves, Mechatronics,15, 683–702, 2005.

[2] Akdağ, F.N., Kuzucu, A., Highly accurate pneumatic position control, Istanbul Technical University Mechanical Engineering Department, http://digital.ni.com/

[3] Barth, E.J., Zhang, J., Goldfarb, M., Control Design for Relative Stability in a PWM-Controlled Pneumatic System, Journal of Dynamic Systems, Measurement, and Control, 125, 504-508, 2003.

[4] Gergely, Z., Judák, E. (2008): „Automatizált paprikaválogatás beágyazott alakfelismerő rendszerrel" Mezőgazdasági technika, XLIX. évf. 2008/11. HU ISSN: 0026-1890

[5] Messina, A., Giannoccaro, N.I., Gentile, A., Experimenting and modelling the dynamics of pneumatic actuators controlled by the pulse width modulation (PWM) technique, Mechatronics, 15, 859–881, 2005.

[6] Nguyen, T., Leavitt, J., Jabbari, F., Bobrow, J.E., Accurate Sliding-Mode Control of Pneumatic Systems Using Low-Cost Solenoid Valves, IEEE/ASME Transactions on mechatronics, 12(2), 216-219, 2007.

[7] Parnichkun, M., Ngaecharoenkul, C., Kinematics control of a pneumatic system by hybrid fuzzy PID, Mechatronics, 11, 1001-1023, 2001.

[8] Shih, M.-C., Ma, M.-A., Position control of a pneumatic cylinder using fuzzy PWM control method, Mechatronics, 8, 241-253, 1998.

[9] Thomas, M.B., Maul, G.P., Jayawiyanto, E., A Novel, Low-Cost Pneumatic Positioning System, Journal of Manufacturing Systems, 24(4), 377-387, 2005.

[10] van Varseveld, R.B., Bone, G.M., Accurate position control of a pneumatic actuator using on/off solenoid valves, IEEE/ASME Transactions on Mechatronics, 2(3), 195-204, 1997.

About the instantaneous carrying force of
narrow sliding radial bearing under hard shocks

Marius ALEXANDRESCU, Radu COTEȚIU,
Nicolae UNGUREANU, Adriana COTETIU

Engineering and Technological Management Department, Technical University of Cluj Napoca,
North University Center of Baia Mare, Baia Mare

Abstract

The paper presents the determining relationship of carriage in non-dimensional form for narrow radial bearings exposed to shocks and vibrations, as well as the determining relationships of the lubricant minimum thickness in relation to the dynamic loading. Due to the very short time of loading radial bearings exposed to shocks and vibrations, of about 0.5-1 ms, we consider only the approaching motion between spindle/axle and bushing on the direction of the center line, without the rotation of the spindle/axle (the case of the non-rotating bearing), so that the effect of the lubricant expulsion be prevalent in the achieving of the self-carrying film.

Keywords

impulse loading, squeeze film, radial hydrodynamic bearing

1. Introduction

The behavior study of radial bearings with hydrodynamic lubrication, functioning under conditions of shocks and vibrations, is carried out from a tribological point of view, observing under the aspect of friction and lubrication, the lubricant film, by which the shock is damped. In the case of bearings exposed to heavy loading (shocks) the difficulty occurring stays in the solution to Reynolds' equation, the equation of energy, the equation of elastic deformations of the axle and bushing surfaces, and the equation of lubricant viscosity and density variation with pressure, and all these together form a non-linear integral and differential system (Bowden and Tabor, 1950).

That is why I consider useful a systemic approach to these problems, with the conviction that the results obtained will contribute to the finding of new solutions, in the qualitative understanding of the phenomena that occur in the functioning of sliding bearings (Alexandrescu and Pay, 2003).

We consider the closing motion between spindle and bushing on the direction of the center line, without the rotation of the spindle (the case of the non-rotating bearing), so that the lubricant expulsion effect be prevalent in the achieving of the squeeze film.

The modeling of the lubricant expulsion effect (squeeze) starts from Reynold's equation, in which we have to consider the terms that contain the closing speed of the two surfaces ($V = -\dfrac{\partial h}{\partial t}$) (Moore, 1993).

Analytically expressed, the Reynolds equation corresponding to this study, within an isothermal approach is (Khonsari and Booser, 2001)

$$\frac{\partial}{\partial x}\left(h^3\,\frac{\partial p}{\partial x}\right) + \frac{\partial}{\partial z}\left(h^3\,\frac{\partial p}{\partial z}\right) = 12\eta\,\frac{\partial h}{\partial t}, \tag{1}$$

where: η – viscosity of lubricant (Ns/m^2); p-pressure (Pa); h- fluid film thickness (m).

The scheme of a narrow hydrodynamic radial bearing with circular bushing exposed to shocks, modeled in 4 areas, is presented in Fig. 1. (Alexandrescu, 2005).
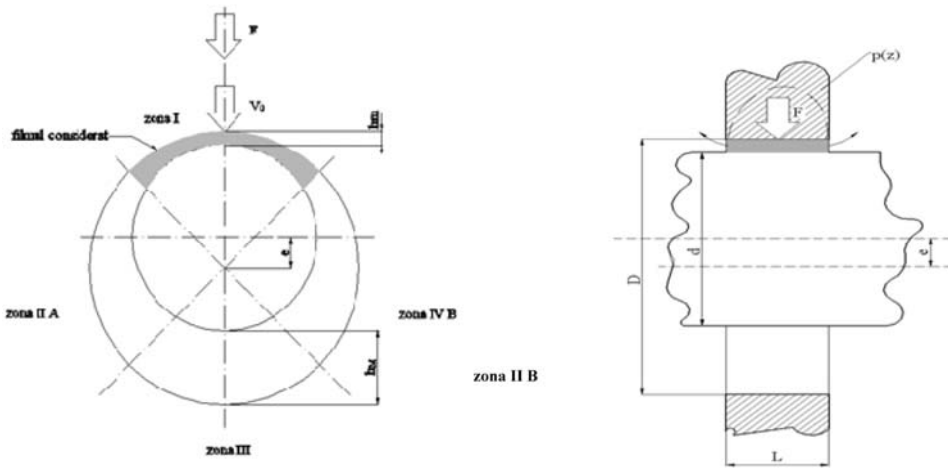

*Figure 1.*The effect of lubricant expulsion under shock for narrow radial bearing

The simplified modeling of the lubricant film thickness and carriage under the conditions of a closing motion of the spindle/axle and bushing surfaces for the narrow radial bearing exposed to shocks (Figure 1.) has as starting point the following hypotheses:
- in zone III the motion is of separating surfaces, pressure decreases, it can be practically considered constant under the conditions of cavity occurrence;
- in zone II A and II B the section remains "approximately" constant and thus the pressure remains constant;

- zone I represents the only area that really opposes the closing motion: the geometry of the lubricant film will be approximated with a constant thickness surface, equal to the minimum thickness of the lubricant film under the condition of static loading, on the basis of the rectangular model of infinite length.

We can write (Alexandrescu, 2005b):

$$h_m = \frac{1}{\sqrt{\dfrac{1}{h_{m0}^2} + \dfrac{8F\sqrt{2gH}}{\eta\pi DL^3 g}}} \,, \tag{2}$$

where h_{m0} represents the minimum thickness of lubricant under static regime, and h_m represents the minimum lubricant thickness in the dynamic regime.

The instantaneous squeeze force has the following expression (Alexandrescu, 2005).

$$\overline{F}_s = \frac{1}{A}\left[\overline{H}_s^{\,3}(1+A) - \overline{H}_s^{\,5}\right], \tag{3}$$

where

$$A = 4\overline{F}\Pi, \quad \overline{H}_s = \frac{h_{m0}}{h_m} = H_{s-ad} \tag{4}$$

and the parameters of lubricant film expulsion Π have the expression

$$\Pi = \frac{H}{h_{m0}} \tag{5}$$

H being the height from which the weight dynamically loading the bearing is launched).

2. Teoretical results

The minimum variation of lubricant thickness of the bearing in a dynamic running regime, for three rotations of spindle n= 370 rot/min and n= 600 rot/min, loading pressures ranging from 0,5 bar to 3 bar, and two static loadings, G=2250 N respectively G=4500 N, are presented in Figures 2.1 and 2.2 (Alexandrescu, Pay and Pascovici, 2005).

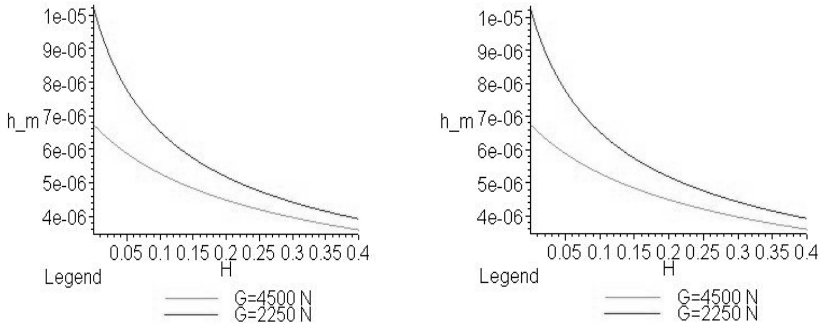*Figure 2.* The variation of the minimum lubricant film thickness
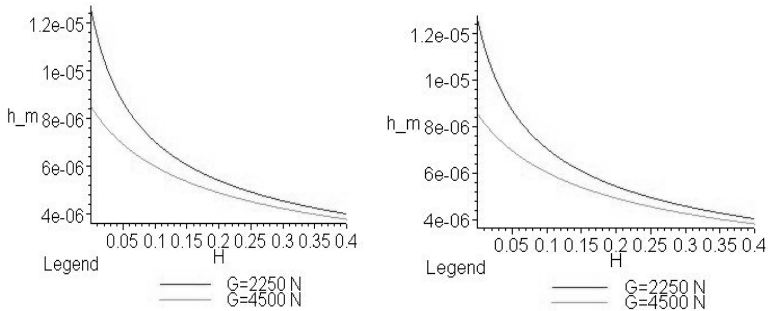in a dynamic regime in relation to H (n=370 rot/min)

Figure 3. The variation of the minimum lubricant film thickness
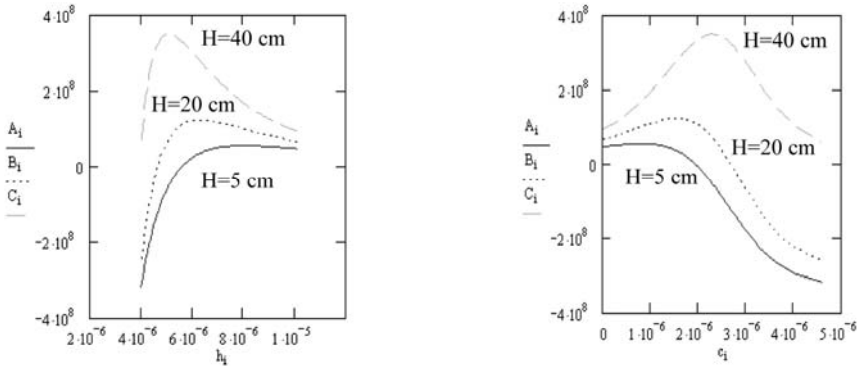in a dynamic regime in relation to H (n=600 rot/min)

Figure 4. The instantaneous carrying force in relation to the dimensional thickness of the lubricant
film (n=370 rot/min, pin=0,5 bar, G=2250 N, hm0=10,175 μm)

The variations of the instantaneous carrying force, in relation to the dimensional thickness of the lubricant film and in relation to the time of shock, for the three weight launching heights H are presented in Figures 4 - 7 (Alexandrescu, 2005).
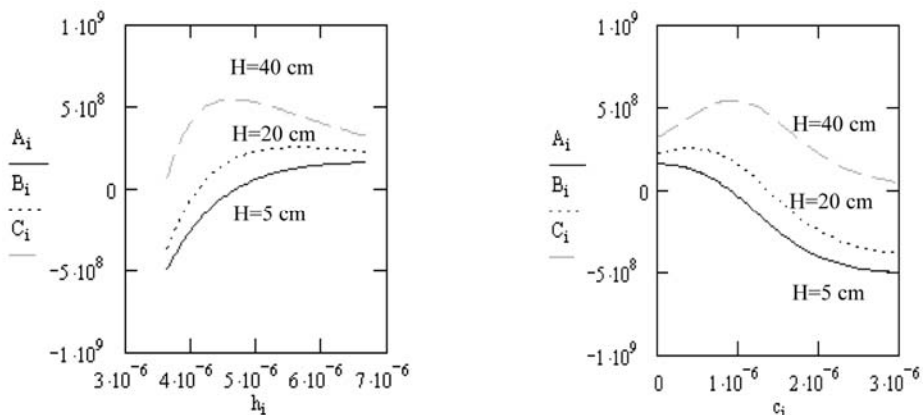
Figure 5. The instantaneous carrying force in relation to the dimensional thickness of the lubricant film (n=370 rot/min, p_{in}=0,5 bar, G=4500 N, h_{m0}=6,723 μm)

Figure 6. The instantaneous carrying force in relation to the dimensional thickness of the lubricant film (n=600 rot/min, p_{in}=1,5 bar, G=2250 N, h_{m0}=12,554 μm)

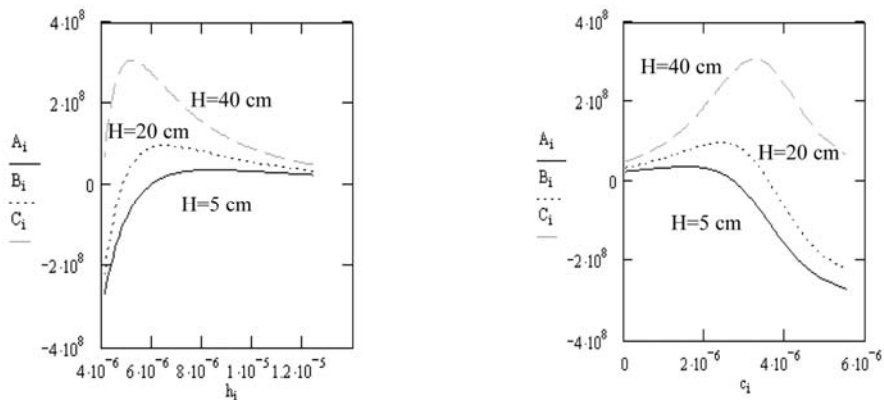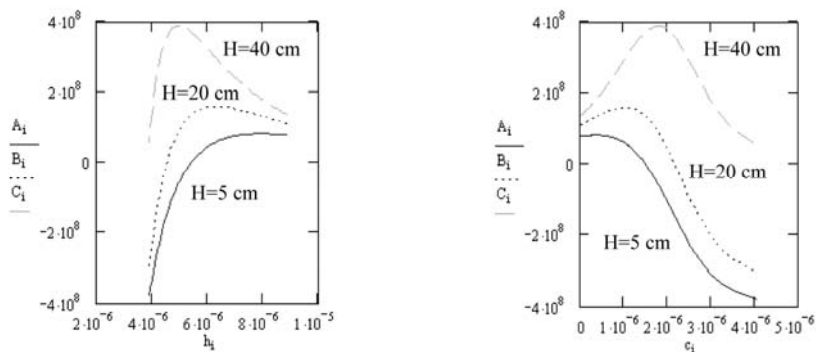*Figure 7.* The instantaneous carrying force in relation to the dimensional thickness of the lubricant film (n=600 rot/min, p_{in}=1,5 bar, G=4500 N, h_{m0}=8,493 μm)

Conclusions

From the analysis of the theoretical results, the following observations can be stated:
- the drastic decrease of the lubricant film minimum thickness along with the increase of dynamic loading (decrease ranging between 50% for the rotation of 370 rot/min and 75% respectively for the rotation of 600 rot/min);
- the decrease of the lubricant film minimum thickness along with the increase of static loading;
- the insignificant influence of the feeding pressure on the minimum thickness of the lubricant for the same rotation of the spindle;
- the decrease, for high dynamic loading (over 2250 N) of the lubricant film thickness under the admissible acceptable value on the basis of rugosity of spindle surfaces, of the bushing respectively ($h_{min,a} \geq 5$ μm);
- the ratio of film thickness Hs_ad sensitively influences carriage: once the area of maximum is outrun, the carriage rapidly decreases;
- the existence of an optimum point from the viewpoint of carriage: any change in the functional parameters of the bearing leads to straying from the optimum value from the viewpoint of carriage;
- in all these situations the following fact is to bare in mind: the short time for pressure variation in dynamic charging (under 0,5 ms).

Nomenclature

L	length of bearing	m;
H	viscosity of lubricant	Ns/m^2;
G	static loading	N;
p	pressure	Pa;
F	dynamically loading	N;
H	fluid film thickness	m;
D	journal diameter	m;
A_i, B_i, C_i	instantaneous squeeze force in dimensional form	N;
H	weight launching height	m;
c_i	time of shock	sec.

References

[1] Alexandrescu, I. M. and Pay, E. (2003) Some Theoretical Aspects Applicable to the Radial Hydrodynamic Working Bearings Under Hard Shocks. Scientific Bulletin, Serie C, Vol. XVII. Fascicle: Mechanics, Tribology. Technology of Machine Manufacturing. Part II. International Multidisciplinary Conference, 5-th Edition, North University of Baia Mare, pp. 25-30, ISSN 1224-3264

[2] Alexandrescu, I. M., Pay, E. and Pascovici, M. D. (2005) The effect of lubricant film expulsion under shock in the case of the narrow sliding radial bearing. Scientific Bulletin, Serie C, Vol. XIX. Fascicle: Mechanics, Tribology, Machine Manufacturing Technology. Part I. International Multidisciplinary Conference, 6-th Edition, North University of Baia Mare, pp. 1-6, ISSN 1224-3264, ISBN 973-87237-1-X

[3] Alexandrescu, I. M. (2005) Studiul comportării lagărelor radiale cu ungere hidrodinamică în condiţiile funcţionării cu şocuri şi vibraţii. Universitatea Tehnică Cluj-Napoca.

[4] Bowden, F. P. and Tabor, D. (1950) The Friction and Lubrication of Solids. Oxford at the Claderendon Press, pp. 259-283

[5] Khonsari, M. M.and Booser, E. R. (2001) Applied Tribology. Bearing Design and Lubrication. John Wiley & Sons, INC., New York

[6] Moore, D. F. (1993) Viscoelastic Machine Elements. Elastomers and lubricants in machine system. Oxford, Butterworth-Heinemann Ltd., pp. 139-163.

Development and evaluation of hybrid aluminium
matrix syntactic foams

Kornél MÁJLINGER[1,2] , Imre Norbert ORBULOV[1,3]
[1]Department of Materials Science and Engineering,
Budapest University of Technology and Economics
[2]Institute of Engineering Sciences, College of Dunaújváros,
[3]MTA–BME Research Group for Composite Science and Technology

Abstract

A special class of metallic foams, the so called metal matrix syntactic foams was produced by pressure infiltration technique. Metal matrix syntactic foams consist of a light-weight metal matrix and a set of hollow spheres. Microstructural investigations were done on polished specimens. The results showed almost perfect infiltration and thin interface layer between the matrix and the reinforcement. Quasi-static compression tests were also done to get basic information about the mechanical properties of metal matrix syntactic foam. The results showed outstanding mechanical properties among other metallic foams. The tests were performed in order to prepare pin-on-disc wear tests.

Keywords

metal matrix composite, aluminium matrix syntactic foam, hybrid composite, compressive behavior, wear

1. Introduction

Metal matrix syntactic foams are particle reinforced composites that consist of light-metal matrix and hollow sphere particles. Metal matrix syntactic foams have outstanding mechanical properties among metallic foams. Their compressive strength and plateau strength are extremely high compared to 'conventional' metallic foams. They have significant damage localizing properties and due to this can bear high amount of mechanical energy during plastic deformation. The capability to absorb significant mechanical properties makes the metal matrix syntactic foams excellent material for collision dampers. Metal matrix syntactic foams are also promising materials for low-weight structural parts especially in applications were the original parts have high moment of inertia and exposed to sliding wear. Their low density can ensure low moment of inertia (this is energy saving) and the hollow spheres can serve as reservoirs for lubricating media such as different oils and greases (this can increase operation time). The mechanical and microstructural properties of metal matrix syntactic foams have been more or less widely studied and published in

the professional literature; in contrast the wear properties are marginally investigated. Our aim in this paper is to give a short insight into the mechanical properties of metal matrix syntactic foams and to present a basic plan for the future investigation of tribological properties.

2. Experimental

The production of metal matrix syntactic foams
Metal matrix syntactic foams were produced by commercial purity Al99.5 (Al1050) or near eutectic AlSi12 alloy (Al4047) matrices due to their low melting point and low viscosity. The measured chemical composition of the matrix materials were: 0.29 wt% Fe and the remaining was Al for Al99,5, and 12.830 wt% Si, 0.127 wt% Fe, 0.002 wt% Cu, 0.005 wt% Mn, 0.010 wt% Mg, 0.007 wt% Zn and the remaining was Al for the AlSi12 alloy. The compositions were in the range of the standardised nominal values. The total amount of reinforcement was maintained at high level (~64 vol.%) that corresponds to randomly closed packed structure. For reinforcement three grades of hollow spheres were used, two ceramic and one metal. The hollow spheres with larger diameter were manufactured by Hollomet GmbH. The ceramic hollow spheres were manufactured by Envirospheres Ltd.

The ceramic hollow spheres with larger diameter (Globocer, GC) had the average diameter and wall thickness of $\varnothing 1450$ μm and t=60 μm respectively, while their density was $\rho=0.816$ gcm^{-3}. The chemical composition of the hollow sphere's wall material was 33 wt% Al_2O_3, 48 wt% SiO_2 and 19 wt% $3Al_2O_3 \cdot 2SiO_2$.

The ceramic hollow spheres with smaller diameter (E-sphere SLG, SLG) had the average diameter and wall thickness of $\varnothing 130$ μm and t=6 μm respectively, while their density was $\rho=0.637$ gcm^{-3}. The chemical composition of the hollow sphere's wall material was the same as in the case of GC spheres.

The metallic hollow spheres (Globomet, GM) had the similar average diameter but lower wall thickness, while the density was $\rho= 0.4$ gcm^{-3}. The fracture force of GC and GM grade hollow spheres between polished plates was 22.1±1.18 N and 5.1±0.18 N (50-50 measurements) respectively, so the GC grade hollow spheres proved to be significantly stronger. The GC grade spheres showed brittle fracture while the GM grade hollow spheres proved failure due to large plastic deformation. The ratio of the hollow spheres was varied from 100% GC and 0% GM to 0% GC and 100% GM, in 20% steps.

The ASFs were produced by inert gas (Ar) assisted pressure infiltration (see Fig. 1).

The hollow spheres were poured into a 360 mm height, graphite coated carbon steel mold (cross section: 40×60 mm) to the half and they were densified by gentle tapping to get randomly close packed spheres (64 vol.%). Subsequently, a layer of alumina mat separator was placed on the hollow spheres and a block of matrix material was put on the mat. The mold was situated into the infiltration chamber; the furnace was closed and evacuated by a vacuum

pump (rough vacuum). The heating was ensured by three heating zones and the temperatures of the matrix block and the hollow spheres were continuously monitored by two thermocouples. After melting the molten sealed the mold above the separator layer. The vacuum pump was switched off and Ar gas was let into the chamber with a previously set 400 kPa pressure. The pressure difference (400 kPa in the chamber and vacuum under the liquid cork) forced the molten metal to infiltrate into the space between the hollow spheres. After solidification the mold was removed from the chamber and water cooled to room temperature. Then the ASF block (~40×60×180 mm) could be removed from the mould. For further details about the production process please refer to (Orbulov I.N. and K. Májlinger, 2013).
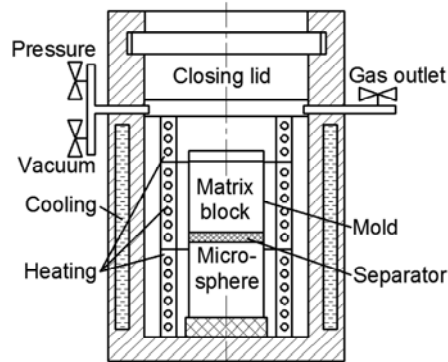

Figure 1. Schematic sketch of the infiltration chamber

Two kinds of hybrid composite blocks were produced: (I) with two different reinforcement material but with the same hollow sphere size range (GM and GC), (II) with pure ceramic reinforcement but very different size range (SLG and GC). In the first case the blocks were designated after their constituents: e. g. 80GM-20GC stands for an ASF block with ~64 vol.% of hollow spheres that is mixed from 80 vol.% GM and 20 vol.% GC grade hollow spheres. In the second case the blocks were also designated after their constituents but without the number for volume fraction. The measured densities (ρ_m) of the blocks, determined by Archimedes' method, are listed in Table 1. The produced ASF blocks to be investigated and the main mechanical properties are also listed in Table 1.

Investigations of the syntactic foams
Scanning electron microscopy (SEM) investigations and energy dispersive X-ray spectroscopy (EDS) along lines were performed by a Phillips XL-30 type electron microscope equipped with an EDAX Genesis EDS analyzer on metallographically polished surfaces. The measurement started from the matrix materials and crossed the wall of the hollow sphere perpendicularly. Each point was excited for 15 s with 35 μs detector amplification time.

The compressive properties were investigated in quasi-static conditions on cylindrical specimens. The aspect ratio (height to diameter ratio, H/D) of the specimens was varied: the diameter (D) of the specimens was 14 mm and the height (H) of the specimens was 14, 21 or 28 mm (H/D 1, 1.5 and 2 respectively). The compression tests were performed on a MTS 810 type universal testing machine in a four column tool with polished surface at room temperature. The specimens and the tool were lubricated with Locktite anti-seize material. The strain rate was 0.01 s^{-1}. Five specimens were compressed from each specimen group up to 25% engineering strain to get representative results and to verify repeatability. The results were evaluated according to the standard (DIN50134) about the compression tests of cellular materials and the characterizing properties (compressive and yield strength, fracture strain, structural stiffness and absorbed energies) were monitored.

3. Results and discussion

The microstructure of the syntactic foams

First the microstructure of the ASFs was analyzed from the point of view of pressure infiltration (see Fig. 2). The ceramic and the metal hollow spheres can be easily separated in the photos. The micrographs show almost perfect infiltration, the smallest cavities between the hollow spheres were fulfilled completely by the matrix materials. The uninfiltrated void content between the hollow spheres remained well below 3% for all the ASFs.
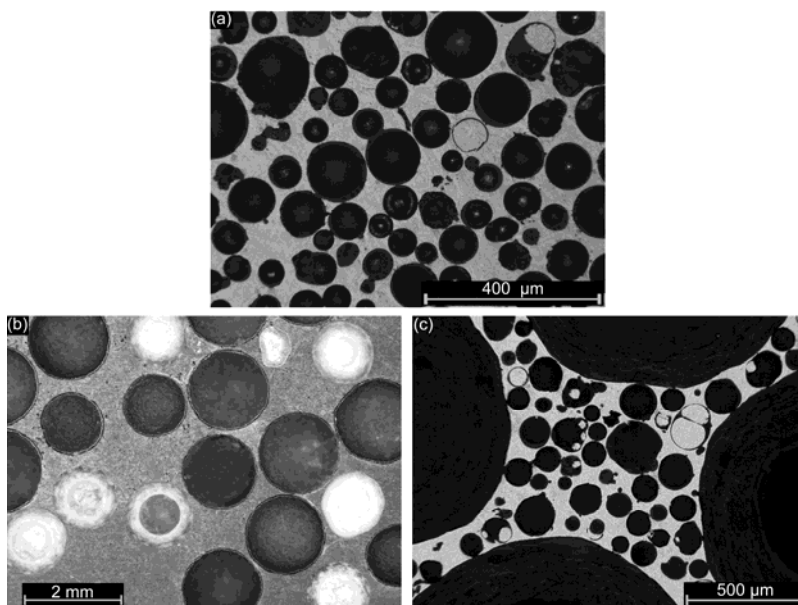

Figure 2. Micrographs of typical areas in the ASFs (a) Al99.5-SLG, (b) AlSi12-80GM-20GC, (c) AlSi12-SLG-GC

Some broken and therefore filled hollow spheres can be observed in Fig. 2a and c, which can occur if the hollow sphere brakes during the infiltration or if it has already broken before the infiltration. In most cases the broken spheres were GM grade, because the molten AlSi12 – as chemically aggressive medium – can dissolve pure Fe from the wall and it can leads to the breakage and infiltration of the hollow spheres. In the case of ceramic hollow sphere the Al content of the matrix could dissolve Si from the wall of the spheres.

The other important point of view is the interface layer between the reinforcement and the matrix material. This layer is responsible for the proper load transfer between the constituents and therefore has determinative effect on the mechanical properties. In the case of ceramic hollow sphere the Al content of the matrix could dissolve Si from the wall of the spheres according to Eq. 1.

$$4Al_{(liq.)}+3SiO_{(sol.)} \rightarrow 2Al_2O_{3(sol..)}+3SiO_{(sol.)} \tag{1}$$
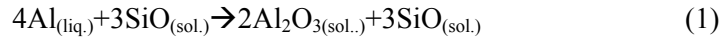
This diffusion reaction is induced by the Si concentration mismatch between the material of the hollow spheres and the matrix. However, this exchange reaction is suppressed by the high Si amount in the matrix. The presence and thickness of the interface layer between the constituents has been investigated by line EDS analysis. A typical site of AlSi12-40GM-60GC ASF is shown in Fig. 3. The SEM micrograph of a GM (left) and GC (right) hollow spheres near to each other and the path of the line EDS analysis (arrow) are shown in Fig. 3a, while the chemical composition along the investigated line is plotted in Fig. 3b.
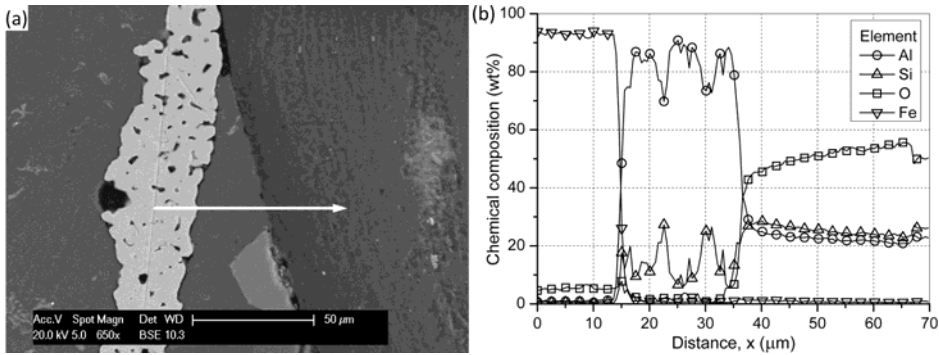

Figure 3. BSE image (a) of a GM (left) and a GC (right) grade hollow sphere
and EDS line-scan profile (b) of AlSi12-40GM-60GC ASF

The SEM micrograph also confirms the perfect infiltration: the less than 10 μm gap between the GM and GC grade hollow sphere is completely fulfilled. The chemical composition along the path of the analysis changes according to the composition of the wall and the matrix materials. The first few microns were measured in the GM grade hollow sphere and shows mainly Fe and some O due to the slight oxidization of the surface. Between the spheres the Al and Si

content is dominant, but Si peaks can be also observed due to the near eutectic composition of the matrix material. In the GC grade hollow spheres the Al-Si-O ratio set to the corresponding constitution of the ceramic wall material. In the interface layers between the GM and GC hollow spheres and the matrix material sudden changes can be observed in the chemical composition. These short transient zones indicate thin interface layers. The thickness of the layers can be estimated from the slope changes of the differentiated Fe and O curves and by the AlSi12 matrix it was 7 μm, 5 μm and 5 μm in the case of GM, GC and SLG hollow spheres respectively. For the Al99.5 matrix alloy the thickness of the interface layers due to the lower Si content were about 1-2 μm thicker, but for all the samples it remained under 10 μm.

The compressive behavior of the syntactic foams

Typical compressive stress-strain curves of the series of the GM-GC ASFs with H/D=1 are shown in Fig. 4, the amount of GC hollow sphere content improved the mechanical properties significantly. In Fig. 5 the structural stiffness values (S, the initial slope of the stress – strain curves) can be observed. It is clear that the mechanical properties are also dependent on the specimen's height to diameter aspect ratio. For our samples general the following dependence of H/D ratio can be made: the structural stiffness values increase with higher H/D ratio, all the other important mechanical properties like compressive strength (σ_c, the first stress peak of the stress – strain curve), yield strength (σ_y, at ε=1%), fracture strain (ε_c, at σ_c), and absorbed energy (W) values decrease with the higher H/D ratio. The main mechanical properties for the investigated ASF's (H/D=1.5) are listed in Table 1.
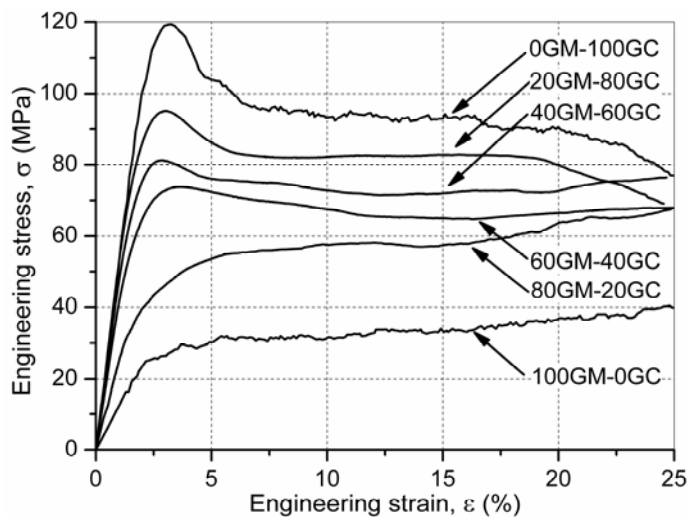

Figure 4. Typical engineering stress – engineering strain curves of GM-GC hybrid ASFs (H/D=1)
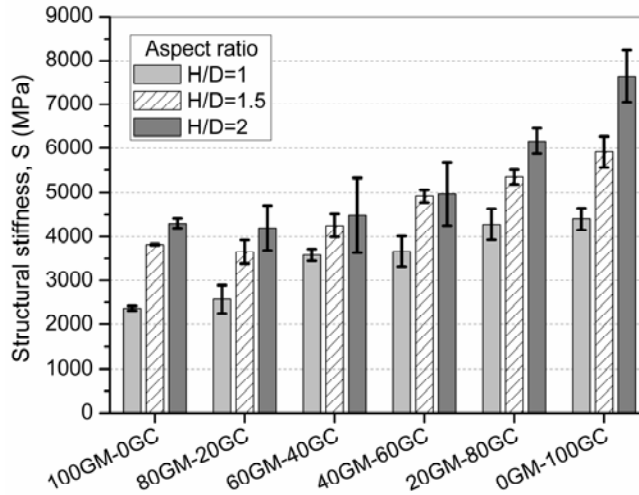
Figure 5. The structural stiffness of GM-GC hybrid ASFs as the function of hollow sphere grade and aspect ratio

GM-GC hybrid ASFs: The compressive strength increased with the amount of GC reinforcement. The gradient of the latter increment was constant and moderate in the case of these ASFs. As the amount of the weaker, plastically deformable GM fraction decreased, the compressive strength increased. In the case of pure GC reinforcement a higher increment can be observed: the stronger GC hollow spheres and the lack of plastically deformable GM hollow spheres ensured higher strength levels. In Fig. 4 the comparison of the curves confirms this trend. The ASFs with pure GM grade reinforcement behave like conventional metallic foams. They had no pronounced compressive strength, but a long, slowly increasing plateau region and completely plastic deformation. In the case of pure GM reinforcement, pronounced compressive strength cannot be determined. As the amount of the GC hollow spheres increased the pronounced compressive strength became more and more emphasized. As the amount of the GC hollow spheres increases, the fracture strain decreases and the failure mode became brittle. The total absorbed mechanical energies had a local minimum in the case of 40GM-60GC reinforcement.

SLG-GC hybrid ASFs: To determine the effect of the sphere size, ASFs were made with pure SLG or GC reinforcement, and also hybrid ASF were produced with SLG and GC reinforcement. ASFs with SLG reinforcement had ~40% higher compressive strength and fracture strain, but ~50% less structure stiffness than the ASFs reinforced with GC hollow spheres. ASFs with SLG and GC reinforcement had about the same compressive properties than those of GC reinforcement, but at lower density.

Effect of matrix material: as it is anticipated ASFs with Al99.5 matrix had higher fracture strain, ASFs with AlSi12 matrix were more brittle but the compressive strength, structural stiffness and total energy values were higher.

Table 1. Main mechanical properties for the ASFs (H/D=1.5)

Matrix material	Reinforcing material	ρ_m (gcm^{-3})	σ_c (MPa)	S (MPa)	ϵ_C (%)	W (ϵ=25%) (Jm^{-3})
AlSi12	100GM-0GC	1,33	*n.a.*	3800	*n.a.*	1200
AlSi12	80GM-20GC	1,64	66	3650	5,0	1550
AlSi12	60GM-40GC	1,65	65	4250	3,7	1500
AlSi12	40GM-60GC	1,69	72	4900	2,7	1400
AlSi12	20GM-80GC	1,74	83	5350	2,6	1650
AlSi12	0GM-100GC	1,83	110	6000	2,7	1650 /2700*
Al99.5	0GM-100GC	1,81	105	5000	3,8	2800*
AlSi12	SLG	1,34	180	2700	6,5	5000*
Al99.5	SLG	1,48	160	2500	6,7	4000*
AlSi12	SLG-GC	1,60	100	5600	2,4	2300*

*corresponds to ϵ=50%

Future plans for wear test: Several studies on the tribological behaviour of common engineering materials e.g. (Keresztes and Kalácska 2010) and (Zsidai et al., 2002) in contact with steel have been published. But the wear properties of aluminium matrix composites have been studied e.g. (Ramachandra M. and K. Radhakrishna 2005), but wear properties of ASFs are not widely studied. Therefore pin-on-disc wear tests are planned to be performed on the specimens listed in Table 1. The investigation of GM-GC hybrid ASFs can give insight to the wear properties of ASFs with different reinforcement in the same size range (with the high strength but brittle ceramic GC and low strength but ductile GM) hollow spheres. The effect of sphere size can be investigated and compared to GC reinforcement by the ASFs with SLG reinforcement. The size of the hollow spheres could have a large influence under lubricated conditions. If ASFs, reinforced with small diameter ceramic hollow spheres are mechanically machined, the hollow spheres will be opened and they can serve as lubricant reservoirs for sliding parts similar to the non-communicating oil reservoirs at laser treated cast iron cylinder blocks (Májlinger and Szabó, 2012). The expected low friction results in lower wear rate, combined with light-weight structure can replace a lot of sliding machine parts like the mentioned cylinder bores in engine blocks. The influence of the matrix material could be also observed by the Al99.5 and AlSi12 specimens. The tests on steel counterparts are planned at 2, 3, 4 ms^{-1} speed like in (Mondal D.P., et al., 2009)) under dry and lubricated conditions (Jha N. et al., 2011). So called small-scale tests are planned to be used because of the simple test rig with low forces and power, reduced cost for preparing test specimens, easy of control of environment. Moreover many small-scale results are available in literature to be referenced, e.g. (Zsidai et al., 2004), (Samyn, 2007), (Keresztes et al., 2008).

Conclusions

From the above detailed investigations, the following conclusions can be drawn:

– Pressure infiltration is a convenient method to produce hybrid ASFs with high hollow sphere content and low uninfiltrated porosity.
– Solution of Fe from GM grade spheres into the AlSi12 matrix occurred, that cause damage to the spheres wall and lead in some cases to infiltrated hollow spheres. An exchange reaction between the Al99.5 and AlSi12 matrices and the GC and SLG grade spheres occurred. In the case of AlSi12 matrix this exchange reaction was suppressed by the high Si amount of the matrix alloy. The interface layers proved to be thin; the average layer thickness was less than 10 μm for all the samples.
– In the case of GM-GC hybrid ASFs the compressive strength as well as the structural stiffness were increased, while the fracture strain was decreased as the GC grade hollow sphere fraction increased, respectively.
– In the case of GM-GC hybrid ASFs the absorbed mechanical energies had a local minimum in the case of 40GM-60GC reinforcement. In the case of higher GC content the compressive and the plateau strengths were higher and therefore the absorbed energies became higher. In the case of lower GC content the strengths became lower, but the ductility of GM grade hollow spheres could balance and overcame this effect.

Acknowledgements

References

[1] Jha N., A. Badkul, D.P. Mondal, S. Das and M. Singh (2011) Sliding wear behaviour of aluminum syntactic foam: A comparison with Al–10 wt% SiC composites

[2] Keresztes R. and G. Kalácska (2010), Research of machining forces and technological features of cast PA6, POM C and UHMW-PE HD 1000, Sustainable Construction & Design, 1, 136-144.

[3] Keresztes R., G. Kalácska, L. Zsidai and O. Eberst (2008) Abrasive wear of polymer based agricultural machine elements in different soil types, Sereal Research Communications, 36, 903-906.

[4] Májlinger K. and P.J. Szabó (2012), Investigation of the surface of a laser-treated cast iron cylinder bore, International Journal of Materials Research, 103/10, 1223-1227.

[5] Mondal D.P., S. Das, N and Jha (2009), Dry sliding wear behaviour of aluminum syntactic foam, Materials and Design, 30, 2563–2568

[6] Orbulov I.N. and K. Májlinger (2013), Mcrostructural aspects of ceramic hollow microspheres reinforced metal matrix composites, International Journal of Materials Research, 9, 903-911.

[7] Ramachandra M. and K. Radhakrishna (2005), Synthesis-microstructure-mechanical properties-wear and corrosion behavior of an Al-Si (12%) – Flyash metal matrix composite, Journal of Materials Science, 40, 5989–5997.

[8] Samyn P., G. Kalácska, R. Keresztes, L. Zsidai and P. De Baets (2007) , Design of a tribotester for evaluation of polymer components under static and dynamic sliding conditions, Proceedings of the Institution of Mechanical Engineers Part J Journal of Engineering triblogy,221 (J6), 661-674.

[9] Zsidai L., P. De Baets, P. Samyn, G. Kalácska, A.P. Van Peteghem and F. Van Parys (2002), The tribological behaviour of engineering plastics during sliding friction investigated with small-scale specimens, Wear, 253, 673–688.

[10] Zsidai L., P. Samyn, K. Vercammen, K. Van Acker, M. Kozma, G. Kalácska and P. De Baets (2004), Friction and thermal effects of engineering plastics sliding against steel and DLN-coated counterfaces, Tribology Letters, 17/2, 269-288.

Scratch evaluation on a high performance polymer

Vanessa RODRIGUEZ[1], Jacob SUKUMARAN[1],
Yeczain PEREZ DELGADO[1], Mariana STAIA[1], Alain IOST[2],
Patrick DE BAETS[1]

[1]Department of Mechanical Construction and Production, Laboratory Soete, Ghent University
[2]Laboratory of Mechanics, Surfaces and materials processing, Université Lille,

Abstract

The scratching process is a well know concept and is usually defined as a kind of surface abrasion, where plastic deformation is promoted by relative friction between soft phase and a hard intender. It is necessary to reduce material loss to minimum or even to reach zero to have an efficient and effective functionality of the materials. Polymers being highly sensitive to wear and scratch damage, their various modes of deformation such as, tearing, cracking, delamination, abrasive and adhesive vary with a narrow range of contact variables like applied normal load, sliding velocity, interfacial lubrication and testing temperature. This is particularly important when these materials are used to improve the tribological performance by adding various types of fillers such as, carbon fibers, graphite, PTFE, TiO_2, and ZnS are added. The polymers with nanocomposites have the advantages over micro- composites from the viewpoint of wear and scratch damage, the underlying mechanism of damage in the single asperity mode is still unclear. The goal of this study is to experimentally evaluate the deformation modes and the friction processes involved during the scratching of polymer reinforced with nanocomposites. The scratches were produced on the semi-crystalline polyetheretherketone (PEEK) surface using a Rockwell C diamond indenter was pressed onto the flat surface of each sample, until a complete load-indentation depth-curve was achieved. These scratched surfaces were assessed with optical microscope and scanning electron microscope (SEM) for prevailing deformation mechanism and the geometry of damage.

Keywords

1. Introduction

When two materials are sliding against each other under the influence of a normal force, usually, the surface of the sharper material loses mechanical cohesion and debris is formed that is dislodged from the contact zone resulting in wear or scratch damage. It is necessary to reduce material loss to minimum

amount or even to reach zero to have an efficient and effective functionality of the materials. However, polymers are highly sensitive to wear and scratch damage, their exhibit various modes of deformation such as, tearing, cracking, delamination, abrasive and adhesive even with a narrow range of contact variables like applied normal load, slider velocity, interfacial lubrication and testing temperature. This is particularly important when these materials are used to improve the tribological performance of bearings, coatings, optical, and plastics engineering applications for consumer products.

The advantages to use scratch damage in polymers is because their usage can be expanded to other applications such as electronic, household and automotive, where long term esthetics is important of scratch. Another advantages is that they can obtain the deformation characteristics for a range of imposed conditions (load, speed, temperature, etc) by a simple test (Briscoe, Evans et al. 1996; Jardret, Zahouani et al. 1998) and still to understand the friction models such as plowing and sliding contributing to friction (Briscoe and Sinha 2003).

A scratch damage is a mark that forms visible grooves and/or surface damage; this is the typical damage mode for surfaces that withstand heavy moving loads by swivels or ball bearings. The complexity of the subject is underlined by the numerous others factors that influence the material response of polymers to scratches; these include scratch loads and speed, coefficients of friction, geometry, and number of scratch tips, amount and types of fillers or additives (Wong, Lim et al. 2004).

In this investigation, various types of nanocomposites are added in a high performance polymer to improve the tribological properties and the effects of nanocomposites in the scratch damage. These nanocomposites often have a deleterious effect on the surface appearance of the polymer due to the poor scratch resistance it imparts. The reason for such an effect is still poorly understood and it will be shown in this work the usefulness of the current method in investigating this effect (J. Jancar 1999). Previous researches (R.A. Vaia 2002; A. Sviridenok 2007; Z.Z Yu 2007) generally defined three major characteristics and form the basis of performance of polymers fillers such as: nanocospically confined matrix polymer chains; nanoscale inorganic constituents, and nanoscale arrangement of these constituents. The full use of these fundamental characteristics of nano-reinforcements in polymers facilitates the achievement of enhanced properties in polymer nanocomposites, which are not displayed by their macro- and microcomposites counterparts. Furthermore, interfaces between nanofillers and matrix in polymers nanocomposites constitute a very high-volume fraction of the bulk material, which is important for bonding of filler to matrix. From the tribological aspect, the benefit of polymer nanocomposites is that the material removal is expected to be less than the micro-sized particle composites since the nano-additives have similar sizes to the segments of the surrounding polymers chains. However, for polymers nanocomposites, there are diver's parameters that may control the friction, wear and scratch damage and include size, aspect ratio, hardness, nature of

polymer/particle interface and transfer films that may arise due to the interaction of the particles and counterface, leading to the complexity in understanding the tribological behaviour of these materials. In this work we are investigated one of the previous parameters mentioned to understand the scratch behaviour of a polyetheretherketone (PEEK) polymer filled with nanocomposites, such as, carbon fibers, graphite and PTFE and to determine if the effects of the those nanocomposites affect the scratch behaviour and the material surface, using simple scratch test with a progressive load and assessed with optical microscope and scanning microscope (SEM) for prevailing deformation and geometry damage.

2. Experimental thecniques

Scratch test device
Scratch experiments were performed in a scratch tester Millennium developed by Tribotechnic with the standard ISO/EN 1071-3, ASTM G171, this test method consists of scratching on the surface with a diamond tip on which is applied a constant or progressive load. The main criteria are that the scratching process produces a measurable scratch in the surface being tested without causing catastrophic fracture, or extensive delamination of surface material. It is applicable to a wide range of materials. These include metals, alloys, and some polymers. Because the degree and type of surface damage in a material may vary with applied load, the applicability of this test to certain classes of materials may be limited by the maximum load at which valid scratch width measurements can be made. When the scratch is concluded, the sample moves under the video system, to examine the different finds of damage done by the tip and correlate it with load applied. A Rockwell C diamond tip indenter with a radius of 0.2 mm was pressed onto the flat surface of each sample until a complete load-indentation was achieve as it can be observed in the figure 1. The scratcher moves across the samples with a scratching speed of 10mm/min while simultaneously applying a progressive load of 50N. After testing, an optical microscopy (OM) and scanning electron microscopy (SEM) was used to investigate the scratch surface characteristics.

Figure 1. Scratch test device

Materials
The semi-crystalline PEEK has found a special interest, as it is characterized by a comparatively good processability as well as outstanding mechanical

properties such as toughness and strength. Whereas PEEK has been identified as a good tribological polymer in general, have clearly highlighted the influence of morphological parameters such as crystallite size and degree of crystallinity as well as orientations on the resulting friction and wear performance. In addition, few fibers are incorporated in the PEEK matrix to increase the mechanical properties, reduced the friction and providing significant enhancement of stiffness and strength.

We have chosen this polymer in the present study to determine the effect of the fibers in the evaluation of scratch deformation, two different PEEK semi-crystalline polymers commercially supplied by INM- Leibniz Institute in Germany proprietary materials were selected based on their characteristics: (i) a wear grade, 10%vol short carbon fiber reinforced PEEK + 10%vol graphite as solid lubricants identified by the name of PEEK-S01 and; a self-lubricating grade PEEK with 10%vol PTFE+10%vol graphite + 10%vol short carbon fiber identified with the name of PEEK-E02. The mixture of the PEEK with various fillers was achieved by twin-screw-extruders by injection moulding with standard screw configurations, the polymers samples were presented in sizes of 70x70x4mm plates and it has been cut to the size of 40x40x4mm in a square shape. The average diameter of the particles was 300nm. In the Table 1 presents mechanical properties of the studied materials.

Table 1. Mechanical and thermal properties of the materials used in this work.

Materials properties	PEEK+CF+Gr (PEEK-S01)	PEEK+CF+Gr+PTFE (PEEK-E02)
Tensile strength (MPa)	126.8	145
E- modulus (MPa)	4696.8	11500
Impact strength (KJ/m^2)	7.5	6
Fracture toughness (MPa $*m^{1/2}$)	4.6	2
Density (g/cm^3)	1.36	1.45
Melting point (°C)	343	343

3. Results and discussion

Various properties were observed in this study such as penetration depth, tangential force, surface damage as a function of load, there are plotted in the figure 2 and 5 for the two PEEK filled with composites were shows the experimental results of scratching test. In both figure, it can be observed that the scratch force is increased as the load increased. From the Coulomb's law, it is evident that there is a linear relationship between scratch force and applied load. In previous investigations by Sujeet Sinha (Sinha and Lim 2006) founds that the scratch forces for all polymers that their investigated such as polypropylene,

polycarbonate, polyvinylchloride, polyetheretherketone etc, were very close to each other for lower loads, but friction forces increases as the normal load (or scratch depth is increased) similar to our results. And they concluded that the interfacial friction effects are larger for softer polymer as the depth of scratch and hence the real contact will be greater for softer polymer than for harder polymer. Thus, the scratch force is adjusted by the indenter tip based on the interfacial friction and yield properties of the polymer. This is applicable to all polymers which deform in ductile manner.

The figure 2 is a typical testing curve for polymers under progressive load scratch test of the PEEK-E02 sample, where the tangential force curves show small magnitude of fluctuations at the beginning and at the middle of the test due to the inertial effects of instantaneously accelerating the scratch head to the designated scratch speed. But after this, the tangential force increase slightly and in a digressive manner to its final level, influences at the end by the movement of the indenter.
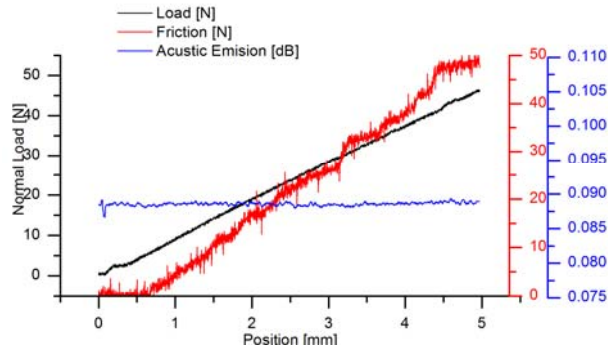

Figure 2. Typical course of the scratch loads versus scratch length measure in PEEK-E02 with a progressive load of 50N
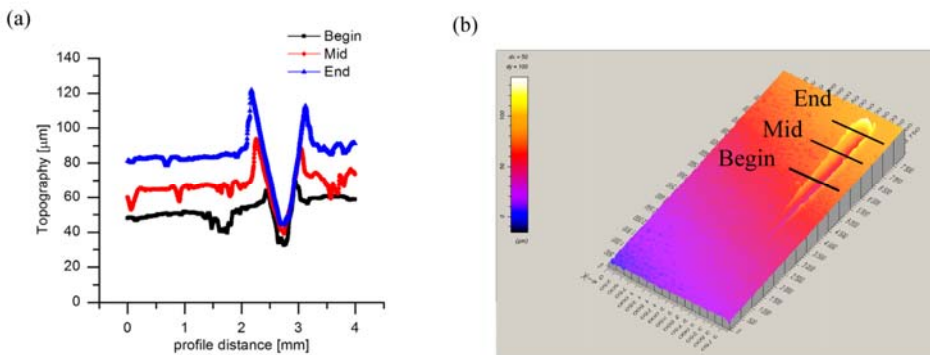

Figure 3. Profilometer results of a typical scratch on a PEEK-E02 surface: (a) depth profile with clear evidence of the scratch with different positions of the scratch; beginning, middle and end (b) 3D view of the scratch test

An evaluation of the scratch produced using profilometry leads to the profiles shown in figure 3 (a) the penetration depth with less material deformation at the beginning and a progressively increasing residual scratch towards the end of the scratch. At this position the scratch depth is also slightly deeper from the normal scratch course, due to the back-movement of the scratch head. In the figure 3(b) a corresponding a 3D view of the scratch following the original scratch direction, so that the deeper valley and the pushed-up hills at the rim of the scratch are more visible.

Additionally a few analysis of scanning electron microscopy images for the PEEK-E02 polymer figure 4 and figure 7 for PEEK-S01, were performed to understand how material deformation and removal processes take place during scratching. This has indications in the understanding of abrasive wear process for polymers because abrasive wear mechanism takes places by hard asperities or loose debris particles.

In figure 4, the sample of PEEK polymer filled with carbon fibers, graphite fibers and PTFE shows that the surface deforms with the formation of noticeable cracks, microcracks, materials removal and some detached debris particles within the scratch zone for PEEK-E02 material. In some cases depending upon the type of the materials and the severity of the contact, the material deformation can take place around the scratch tip with or without wear debris formation (Rajesh and Bijwe 2005).
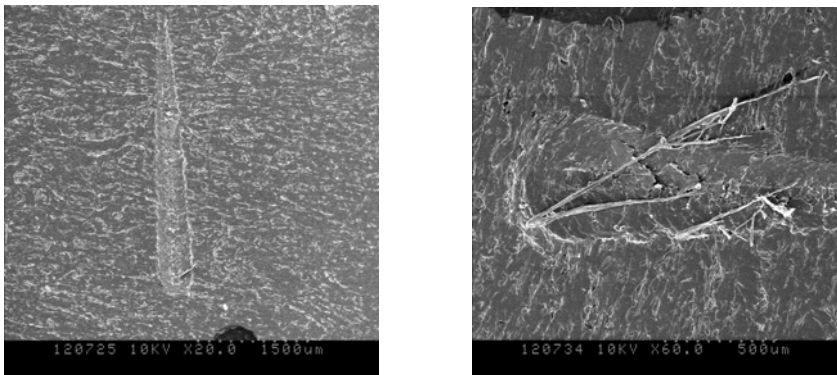

Figure 4. The scratch surface damage observed using scanning electron micrographs on PEEK-E02 under the scratching load of 50N and scratching velocity of 10mm/min

For the PEEK-S01 material filled with carbon fibers, graphite fibers shows smaller differences in the curve under the progressive load of the scratch test compared with the PEEK-E02 polymer as it can be seen in the testing curve under load scratch test figure 5, the appearance of the scratches on the both materials is rather similar but in this case with less fluctuations and smooth changes during the scratching test. The scratch frictional force, and contact zone size increased almost linearly with applied load.
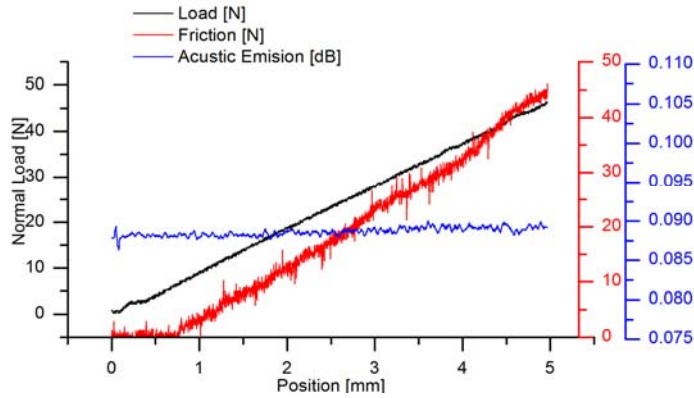
Figure 5. Typical course of the scratch loads versus scratch length measure
in PEEK-S01 with a progressive load of 50N.

The depth profilometry allows obtaining more precise information on the remaining penetration depth during scratching test. In the figure 6 (a) we can see the variation of the penetration in the bulk of polymer for the PEEK-S01 filled with carbon fibers and graphite it can be seen how is slightly deeper and smoothly in the beginning until the end of the scratch test. And it can be notice in the figure 6 (b) the 3D images and the penetration depth and the grooves formation during the scratching test in the material tested.
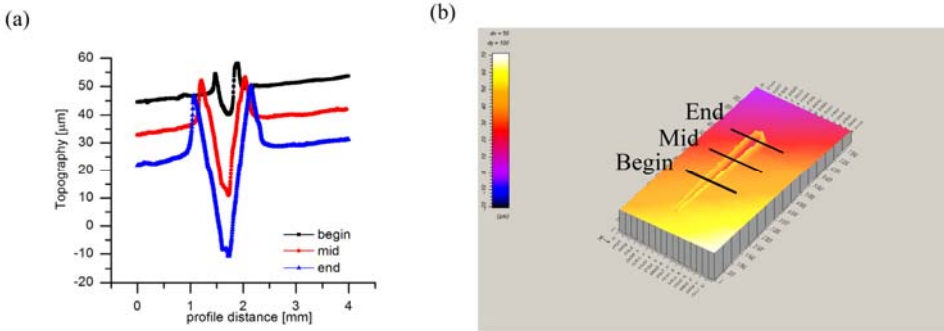

Figure 6. Profilometer results of a typical scratch on a PEEK-S01 surface: (a) depth profile with clear evidence of the scratch with different positions of the scratch; beginning, middle and end (b) 3D view of the scratch test.

Also, by scanning electron microscopy (SEM) of the PEEK-S01 polymer in the figure 7 we can see the contour of the scratched surface when the load was further increased. The PEEK-S01 surface deforms with the formation of noticeable cracks within the scratch. A regular crack formation was seen, which can be due to surface stresses that the microstructure in the semi-crystalline polymer were subjected. Comparing SEM images of the PEEK-S01 with the

material PEEK-E02 it can be observed there is not clear formation of debris of the PEEK-S01 than in the SEM images of the PEEK-E02. A well-defined edge on the two sides of the scratch groove and a smooth scratch surface are formed after scratch pattern.
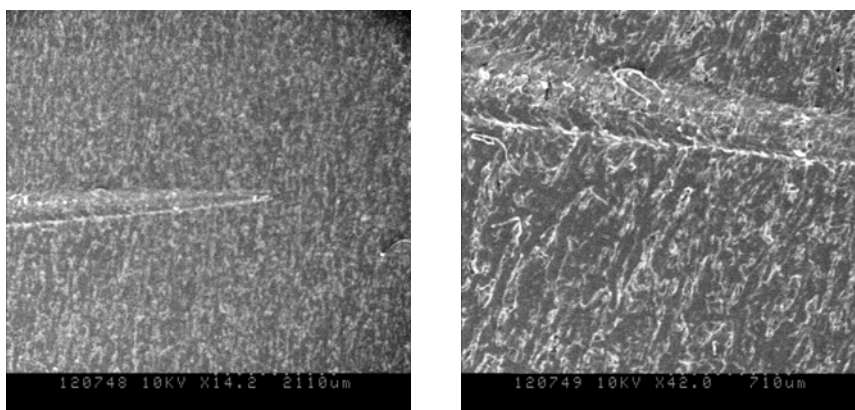

Figure 7. The scratch surface damage observed using scanning electron micrographs on PEEK-S01 under the scratching load of 50N and scratching velocity of 10mm/min

Conclusions

In this paper a scratch test method has been evaluated into a polymers filled with nanocomposites to determine the effect of the filler into the scratch resistance. The progressive load that was applied was 50N at 10mm/min of scratching speed. The scratch force was study the trends with increasing normal load and the penetration depth of scratch. Further scanning electron microscopic was carried out on the scratched polymer surface to investigate the deformation material and the removal characteristics. From this investigation we can draw the following conclusions:

Adding different fillers in the matrix of PEEK polymers it do not have significantly change in the scratching test and the penetration depth is slightly more deeper for the PEEK-S01 than PEEK-E02 this can be attributed that the PTFE the solid lubricant its accumulated around the carbon and the graphite fiber acting as a smoothing material.

Observing the SEM micrographs of the scratches on the material illustrates cracks, microcraks, material removal and debris in the contour of the scratch zone for both types of polymers.

Acknowledgements

References

[1] A. Sviridenok, M. I., T.Kovalevskaya (2007). Carbon nanotube-filled Polyamide:physical and mechanical properties. Micro-nano technologie. Vienna, Austria: 73.

[2] Briscoe, B. J., P. D. Evans, et al. (1996). "Scratching maps for polymers." Wear 200(1â€'2): 137-147.

[3] Briscoe, B. J. and S. K. Sinha (2003). "Scratch Resistance and Localised Damage Characteristics of Polymer Surfaces – a Review." Materialwissenschaft und Werkstofftechnik 34(10-11): 989-1002.

[4] J. Jancar, R. H. R. (1999). Mineral fillers in thermoplastics I. New York.

[5] Jardret, V., H. Zahouani, et al. (1998). "Understanding and quantification of elastic and plastic deformation during a scratch test." Wear 218(1): 8-14.

[6] R.A. Vaia, R. K. (2002). in Polymers Nanocomposites:Synthesis, Characterization and Modeling. ACS Symposium Series. 804.

[7] Rajesh, J. J. and J. Bijwe (2005). „Investigations on scratch behaviour of various polyamides." Wear 259(1â€'6): 661-668.

[8] Sinha, S. K. and D. B. J. Lim (2006). "Effects of normal load on single-pass scratching of polymer surfaces." Wear 260(7â€'8): 751-765.

[9] Wong, M., G. T. Lim, et al. (2004). "A new test methodology for evaluating scratch resistance of polymers." Wear 256(11â€'12): 1214-1227.

[10] Z.Z Yu, A. D., Y.-W.Mai (2007). Polymer-clay nanocomposites-A review of mechanical and physical properties. Singapure, Processing and properties of nanocomposites

Analysis of the defects of couplings for fire hoses

Nicolae UNGUREANU, Cornel BABUT,
Miorita UNGUREANU, Mihai BANICA
Engineering and Technological Management Department,
Technical University of Cluj Napoca,
North University Center of Baia Mare, Baia Mare

Abstract

This paper presents a part of a research on different elements of coupling for fire hoses. These are very important components of the hydraulic systems used by firefighters to deliver one or more suppression agents into the fire. Damaging of these connecting items may lead to serious delays of the fire extinguishing process. This may have serious effects on the rescue operations of the persons and goods threatened by fire. This paper presents the defects of the couplings that appear during fire suppression operations.

Keywords

Fire hoses, couplings, defects, firefighters.

1. Introduction

General presentation and background
Romanian, and not only, firefighter units have seen an exponential increase of their missions's complexity during the last two decades and especially since 2004, after the merger with the civil protection units, to form the departments for emergency situations. Their tasks, as first responder units, cover a wide range of events, that stretch from extrication of car accident victims to earthquake effects. Nevertheless, one of their basic missions remains fire suppression.

In order to accomplish this task, firefighters use a wide variety of equipment such as tanker trucks, pumper trucks, ladder trucks, fire extinguishers and fire hoses. These are ment to deliver one or more suppression agents into the fire. Most common for dosing fires are water and foam, [Ba93] which are delivered through a chain that starts with the fire truck, pumps and continues with the fire hoses, ending with the nozzle that delivers the supression substance into the fire. Fire hoses are manufactured in standard lenghts, usualy 20 liniar metres. They are conected to the fire truck or to the hydrants with couplings(hose tails). When needed, one or more sections can be extended with couplings, which makes these components very important parts of fire control operations. This type of connectors is used also for suction purposes, for adapters and caps. Damaging of the coupling parts [Had12] leads to serious delays of the fire extinguishing

actions. This may have serious effects on the rescue operations of the persons and goods threatened by fire.

Analysis of the defects of couplings and their causes
Romanian firefighters are using the couplings/hose tails so called „Storz" type, which are also known as the „sexless" or „quarter-turn" couplings as they have no „male" or „female" parts and the connection is made by inserting the lugs of each part into the slots in the flange of the other, then rotating them with a quarter of a turn.

The basic design of a Storz type coupling is shown in fig. 1. An exploded view is given in fig.2. Connected couplings are shown in fig. 3.

D$_1$ – distance between lugs
D – inner diameter of the pipe
D – external diameter of the pipe
1 – body with hooking lugs
2 –pipe/tail piece
3 –safety ring for pipe's position locking
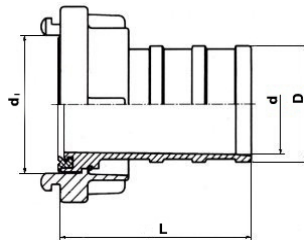4 –sealing ring/gasket

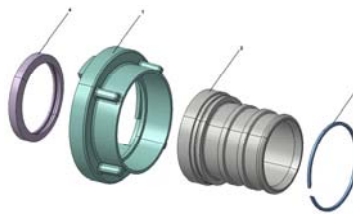*Figure 1.* Storz type fire hose coupling basic design

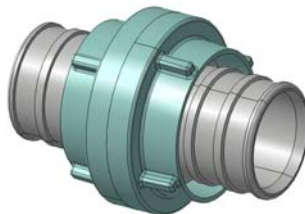*Figure 2.* Fire hose couplings- exploded view

Figure 3. Connected couplings in operating position

The characteristics of delivery and suction couplings given by Romanian standards are shown in table 1. An analysis of the risk factors for fire hose coupling damaging led us to a specific Ishikawa (fishbone) diagram, shown underneath.

Table.1. Delivery and suction couplings characteristics according to [MA92]

Type	A	B	C	D
Diameter d (mm)	96	62	43	18
Mass (kg)	2,1	1,67	0,86	0,24

Fire hose couplings used by Romanian firefighters are made of cast aluminum; more specifically- AlSi5Cu1 alloy, which has Si=[5-6]% and Cu=[1-1,5]%, according to [Ni10].

According to[Wi05], the alloy's main mechanical properties are:

R_m=[299 – 346]   [Mpa]

K_{ic}=[22,05 – 26,50] [Mpa]

Where:

  – R_m- tensile strength
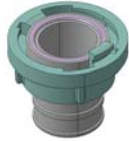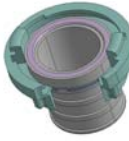 – K_{ic}- plain strain fracture toughness

While in use, fire hoses couplings are subjected to important strains that often lead to critical damage. Cracks, wear of the flanges, breaking of the locking lugs, wear of the gasket and breaking of the safety/snap ring are the usual defects recorded. Empirical observations led to a pattern: the most frequent damage that occurs is breaking of the hooking lugs. The defect occurence is linked to working and environment conditions of the firefighter units which implies mechanical and hydraulic shocks, uneven distribution of the strains, fretting wear and fatigue.
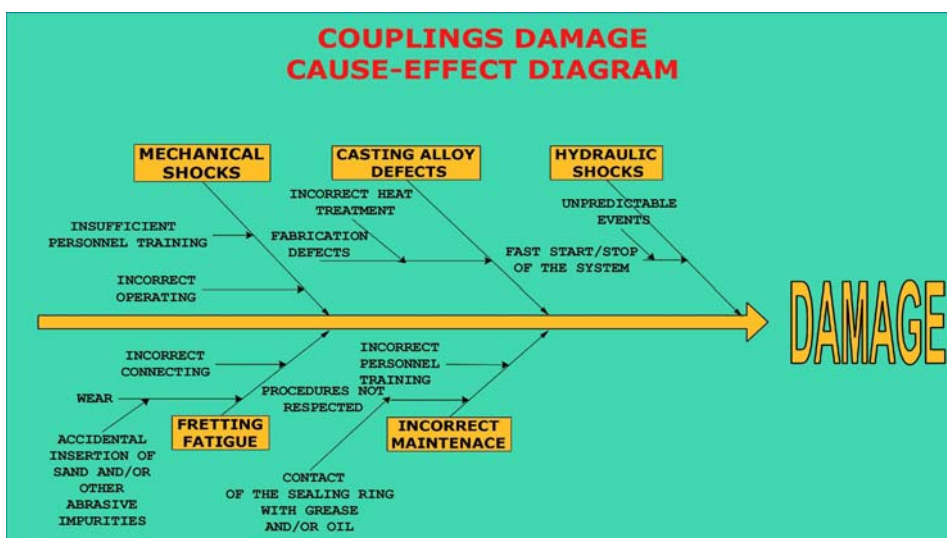
On the basis of the diagram, we attempted to identify the main defects of the couplings, describing them and identifying their possible causes, as shown underneath, in table 2.

Table 2. Couplings defects and their causes

Current number	Defect description	Figure	Probable cause
1	Breaking of the lugs		Hydraulic shock Mechanical shock Fretting fatigue
2	Cracking of the body ("Storz head")		Mechanical shock Incorrect heat treatment
3	Fretting wear marks on the flanges		Incorrect connecting Ingestion of sand and/or ther abrasive materials in the coupling
4	Wear of the gasket		Rubber fatigue Contact with grease and/or oil
5	Breaking of the safety/snap ring		Fabrication defects Incorrect assembly

Conclusions

This paper presents the most important damages of the couplings that occur while operating a fire suppression system with flexible lines, i.e. fire hoses. Tis paper presents also the graphic description of the analysed defects. This damages have a great impact on firefighter missions, as they may lead to delays or even hault the fire control operations, thus imperiling properties and goods, with tremendous economic impact and even lives of persons caught in the fires or those of the firefighters themselves.

Therefore, a further study is needed and should aim to creating a database that would allow damage probability calculations, creating a mathematical model of the defects occurence, and a photographic database of the identified defects.

References

[1] Bălulescu P., I. Crăciun: Agenda pompierului, Editura Tehnică, Bucureşti, 1993 [Ba93]

[2] Miodrag Hadžistević, Imre Nemedi, Milenko Sekulić, Martin Bosak, Janko Hodolič: Multi-Aspect Value of Measuring Systems and Methods Based on the Results of Roundness Measurements. Journal of Mechanics Engineering and Automation. Volume 2, Number 8, August 2012 (Serial Number 14). pp 514-520. [Had12]

[3] Manual pentru cunoasterea accesoriilor,utilajelor si autospecialelor de stingere a incendiilor Editura Ministerului de Interne 1992[Ma92]

[4] Niţu, Margareta Iulia: „Cercetări privind îmbunătăţirea unor proprietăţi fizico-mecanice la aliajele de aluminiu turnabile prin intermediul tratamentelor termice", Teză de doctorat,Universitatea „Transilvania" Braşov, 2010[Ni10]

[5] Ungureanu, N.S.: Fiabilitate şi diagnoză, Editura Risoprint, Cluj Napoca, 2003[Un03]

[6] Wierzbińska M, Sieniawski J, Effect of morphology of eutectic silicon crystals on mechanical properties and cleavage fracture toughness of AlSi5Cu1 allo, Journal of Achievements in Materials and Manufacturing Engineering. 01/2005[Wi05]

The effect of MQL to the tool life

Attila KÁRI-HORVÁTH

Institute for Mechanical Engineering Technology
Szent István University, Gödöllő

Abstract

The lubrication method (MQL) applied during cutting will meet the requirement of minimum quantity lubrication, when the amount of lubricant does not exceed 50 mg per hour [1], occasionally even less than that. The German term MMS for this lubrication method is derived from 'Minimal Menge Schmierung', the English MQL from 'Minimum Quantity Lubricant' [2]. MQL is often referred to as semi-dry lubrication [3], or micro lubrication [4]. MQL-lubrication, however, is not a precise term for the lubrication applied with minimum lubricant in everyday practice. Minimum lubrication can be applied for:
- lubrication of machine and machine parts
- machining

Keywords

machining, minimum quntity Lubricant

1. Introduction

For more than 60 years there has been a great effort to minimalize the amount of lubricant used with machines and machine parts [5]. Minimum lubrication has been widely used under well-defined conditions in the misting lubrication of high-speed ($v_k \geq 25$ m/s) cogwheels, aerosol lubrication of chains and cable-ropes, or the drip feed lubrication of valves and cylinder barrels in aerosol and air-compressors, the injection lubrication in screw gears and screw compressors, or with drip feed lubricators controlled by a magnet valve. While the application of this method has not spread beyond this narrow scope, the lubricators have been remarkably improved. The idea of the minimum lubricant method is that the amount of lubricant, which was developed for the lubrication of a particular case, is minimized considering the circumstances. Hence the term **minimized** lubrication.

It is possible to minimize the amount of cooling lubricant in cutting technology as well. In this case, however, the excess heat that is generated has to be removed, which limits the minimizing process. Here it is the molecular behaviour of the particular material, and not the physico-chemical and thermodynamic properties of the lubricating mass, that is exploited, when MQL lubrication technology is applied.

At the moment, the terms used in both laboratory studies and the practice are confusing. Some researchers carry out experiments with two-phase colloid systems, although MQL, by nature, is best used with homogeneous materials.

2. The Tribological aspects of cutting

The chisel penetrates the material to be machined during cutting, and separates pieces, the chips, most of which slide off from the front end of the tool, while leaving melted particles and residue between the back side of the tool and the freshly cut edge (virgin surface). The particles slide along the shearing action causing internal friction, while the chips and melted particles generate external friction (Figure 1), but in case of ceramit cutting the method run not in the same process [6].

Friction, either internal or external is a dissipative process during which energy transfer takes place. It is a well established fact that 97% of the energy used for cutting off a piece of material turns into heat, while the remaining 3% stays in the machined piece as internal tension. Deformation in metal working is often limited to a narrow strip of material, where the temperature rises in a nearly adiabatic fashion due to the deformation work. In this narrow strip the deformation results in both formation hardening and thermal softening. The energy needed for cutting can be effectively reduced if the thermal plasticity at the cutting edge and the rigidity at the cutting stem are increased. Both requirements cannot be meet at the same time by the method of general lubrication that is used today. Localized thermoregulation has to be used.
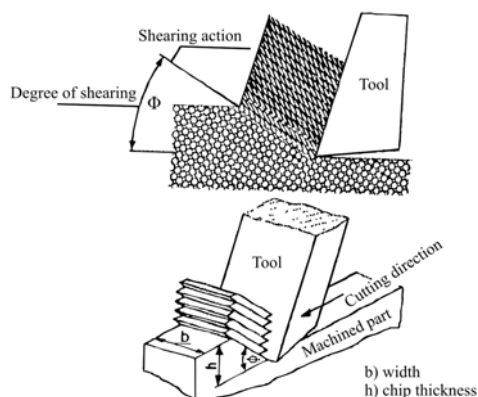

Figure 1. Cutting detachment process

3. Function of the cooling lubricant in cutting

The friction between the chisel and the machined piece depends primarily on the following factors: the parameters of the cutting process, the shape and material of the chisel, the forces created during cutting, the pressure between the chisel

and the cutting surface, the generated heat, the temperature of the touching surfaces, the cutting liquid and the cooling method.

The cooling lubricant has three functions in metal working. One is the removal of the excess working and frictional heat, in other words, cooling. The other is lubrication, which is the reduction of wear at the touching surfaces, between the chisel and chips and the chisel and the machined piece. Since it also helps remove the chips, it has a washing effect. [7]

Where the emphasis shifts in these three basic functions depends on the technology, material, and other factors.

The literature around 2000 frequently mentioned the need to re-examine the multifunctional role of cooling lubricants [1, 2, 9, 10, 12]. The debate was about whether the prevailing system should be developed according to certain functions or whether there should be a total change and the high-speed, high-temperature dry machining, yielding small surface-size chips, should be introduced. Neither the theoretical nor the practical, technological conditions for total change are present yet, but there exists a transitory stage between the two, as shown in Figure 2. Since the reduced amount of cooling lubricant stands between dry and wet working, attempts have been made to reduce the amount of cooling lubricant. These attempts were successful and the method spread widely within a short period of time (five years). Today it is called MQL cooling, lubricating. The benefit of the quick success is that less cooling lubricant, which is highly polluting, is being used, the drawback is that studies of the new method have not started. The researchers have been limiting their efforts to trying to find out which one of the cooling lubricants on the market was right for their purposes.

Over a period of time expectations developed.
- On the one hand, lubricant developers were waiting for the mechanical engineers to provide them with guiding parameters for developing the new types of cooling lubricants.
- On the other hand, mechanical engineers and cutting experts were expecting new products from the developers.
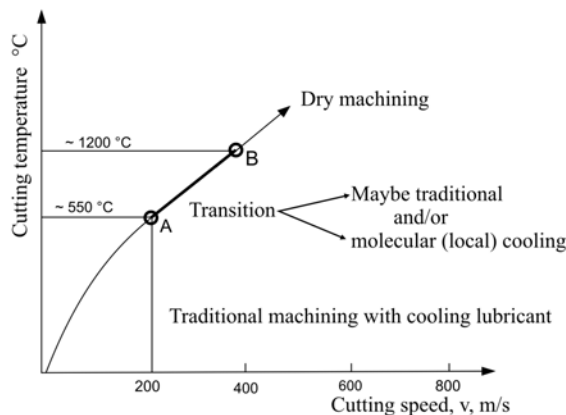

Figure 2. Cutting temperature change as a function of cutting speed in the case of steel and heavy metal tools

The prevailing methods of cooling and lubricating technology in metal working make it possible to avoid the formation hardening or to keep it within reasonable limits. However, if the surroundings of the chip cutting are over-cooled, the energy requirement is increased. That the whole system can be easily over-cooled was proven in studies from the 1970s, in which the measured temperatures during cutting were about 300 °C lower than what had been anticipated by the thermodynamically calculated temperature. Physicists at the time believed that part of the fluids (lubricants and air) at the cutting temperature and pressure become ionized and the emitted photons create electric wind [11]. This is the Peltier effect.

The key point in MQL lubrication is that while the thermoplasticity in the shearing action can be maximized, the formation hardening is delayed until the chips start to slide off on the front of the lathe tool, creating separate chips.

4. Discerning a numerical value to represent wear

The datas of experiment:

Experimental data	Technological data
Normal ambience DIN50014 and ISO554-1970 feed: f (h) = 0.25 mm/rev	Feed: f (h) = 0.025 mm/rev. Feed: f (h) = 0.067 mm/rev.
Lathe: HC/TiN, CNMG 1204 08 PF 4015 by DIN/ISO 513	Grip depth: a (b) = 1 mm
Quality of workpiece: 42CrMo4 (matter number: 1,7225)	Revolution: n = 1730 min^{-1}
Machine tool: C11A type lathe	
MQ-Lubrication applicator: Cobra 2000	

Wear is defined by the DIN50321 standard. According to the definition, the amount of wear is measured by the „numerical value of wearing", which depends on

- the total use and
- the tribological system

It can be grouped by:

- the type of wear
- the extent of wear

Before the use of coated heavy metals in the 1980s, tool wear was measured by the width of VB-crater wear and the depth of KT-crater wear. More recently wear has been obsereved to spread spontaneously on the edges of tools. The typical process of wear can be seen in Figure 3. It closes on a horizontal axis in a straight line then in a given moment an enormous tangent directional process may be observed. Forty-one of 60 experiments had the graph depicted in Figure 3.
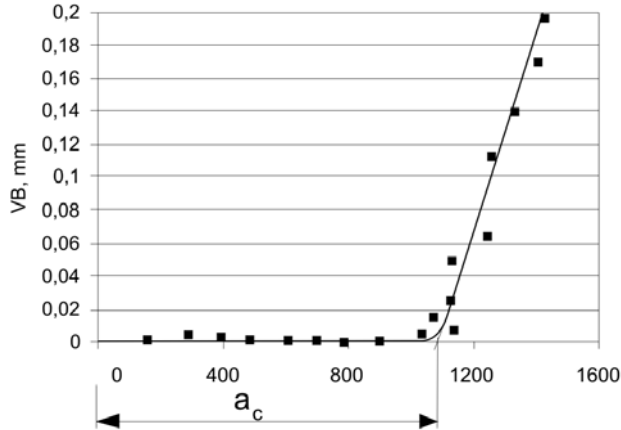
Figure 3. Standard wear curve of ceramics and heavy metals
(E-lubricant, induced emission, 50 g/h)

Various types of wear are superimposed on normal tool wear during machining which is parallel to the horizontal axis. The action mechanism of these types of wear depends on the cutting speed and could be adhesion, decay or diffusion at high speeds.
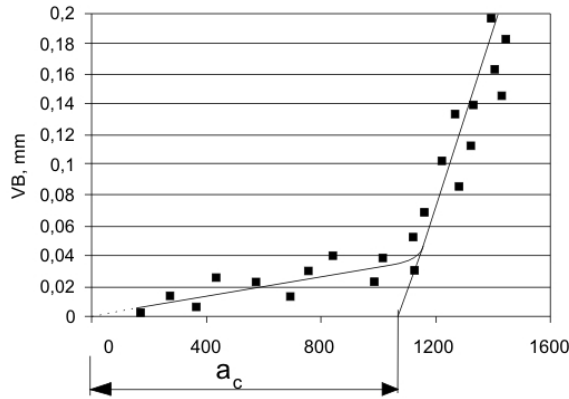

Figure 4. Standard ceramic wear with initial adhesive wear

On coated heavy metal tools the base wear happens on a molecular level as metal transfer. At 400m/min (if there is metallurgic affinity between the tool and the work piece) diffusion takes place. Other types of wear do not develop. Wear appears as luminescence. The constant use of a tool results in accumulated energy, which over a period of time through the use of a "third" body instantly creates brake wear. The amount of work (measured in mass, time etc.) put in over a period of time is the known as the lifespan of a tool. The lifespan of ceramics can be called a_c. After this point the quality of the surface of workpiece

dramatically goes down. With this surface monitoring deal many researcher, who shows the behaviour of these surfaces. The filtering technology and the roughness parameters help to describe the modifications of the surface microtopography modifications [13].

The wear procedure can be seen in some of the cases shown in Figure 4. In theory this is similar to the previous cases with the exception that these cases start out with slight adhesive wear. This wear decreases with the increase of cutting speed.

After the first breaking point, the break wear becomes more intense. This leads to a decrease in surface quality. The first breaking point is a system-related and not parameter-related. This is in reverse proportion to the cutting detachment's energy level.

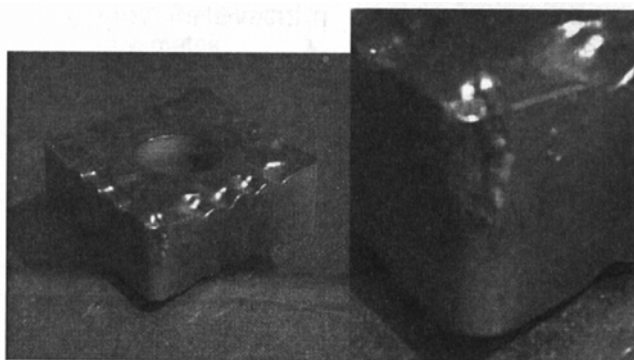Figure 5. indicates the resulting wear (changes) in the lathe tools.

Figure 5. The lathe tools that were used

5. Analysing the oil retention factor of the tool surface

The analysis of the energy levels of modern tool coatings show that their polar energy quotients were similar. The differences were mainly due to aggregate residue (chemically modified) impurities, usually decreasing the quality. The surface's profile finishing factor is $K_h \sim 96\%$, which means that the surface's ABBOTT oil retention factor is near zero. The surface moistening ability was tested with the well-known cigarette paper test, which was supplemented by a 45º tilted experiment for oil-run. These unfavourable circumstances must be compensated for by lubricant quality, setting the technological parameters, etc. This compensation is needed so that the effects of molecule manipulation can be seen.

6. Basic requirements for lubricants

Multiple experiments and examinations show that the MQL (basic lubricant) and its accessory requirements differ greatly from traditional emulsive and cutting

oil requirements. (4-6) s lifespan oil's time dependant properties need not be taken into calculation.

It has been proven that MQL lubricants have a very good spread. They need very good moistening properties (α <30º) and strong absorption cooling to connect to a tool's surface (σ = 32 mN/m).

Better results were observed in the case of MQL lubrication with lubricants that are made up of a polar-group (-OH, -COOH, -NH$_2$, etc.) and saturated, linear, apolar hydrocarbons of the same length (amphiphiles). Such lubricants will allow the needed oriented polymolecular lubricant layers to build up on a surface.

MQL lubrication is most effective if it completely disappears from the surface within less than four or five seconds of evapoation and ionization.

During these experiments it has been made clear that the initial boiling point of lubricants and their properties in the destillation graph are the most important in the case of MQL lubrication. The experiments so far have reinforced our expectations that mineral-based oils and ester oils are most suitable for MQL cooling and lubrication. MQL oils require a stable refraction coefficient in the magnitude of n = 1,5l.

Conclusions

A modified lathe was used as the equipment for the experiment. The measuring equipment was secured. A parallel light emitting LED lamp was used, as was a small output (P < 1mw, 630< λ < 680nm) laser and a 'Cobra 2000' drip feeder. A theoretical method based on comparing the k_c value of the chips' thickness was created for assessing the experimental results.

It has been proven with in the boundary of the experiment that local cooling can be achieved at a molecular level. Thermoplasticity (reduction of internal friction) and chip base rigidity can be increased by the use of molecules manipulated by induced emission and the Doppler effect, which is how internal friction can be decreased. The internal stress created by the cutting energy is decreased by 3%. This way the crystallite changes in the layers near the surface become more favourable.

The action mechanism of MQL lubrication has been clarified, and the specific requirements for MQL lubricants has been determined. The surface oil retention ability of coated heavy metals has been examined as have the properties and amounts of the tool wear process.

More research still needs to be done, however. Experiments are being conducted, which are expected to provide more and clearer information on localized cooling. This is why γ-photon experiments have also been added to the programme. More MQL lubricant-specific experiments will be carried out as a result of the current test results.

The results summed up in the article and the results of tests that are currently underway supplement the presently existing knowledge of MQL lubrication,

which is important not only for immediate use; it creates the basis for a paradigm shift in cutting technology.

References

[1] Weinert, K.:Trockenbearbeitung und Mineral Menge Kühlschmierung, Springer, Berlin, 1999

[2] Avila, R. F. – Abrao, A. M.: The Effect of cutting fluids on the machining of hardened AISI 4340 Steel. Journal of Materials. Processing Technology 119pp 21-26. 2001.

[3] Klocke, F. – Eisenblatter, G.: Proceedings of the Opening Session of the Dry Cutting. Annuals of the CIRP. Vol. 46/2 pp 519-526. 1997.

[4] Ma Clure, T. F. – Adams, R. – Gugger, M.D.: Comparison of Flood vs. Micro-lubrication on Machining Performance, htp://www.unitcom techsolve. Htm1 (accessed. Jan 23.) 2006.

[5] Valasek, I.: Ipari tribológia. Tribotechnik Kft. Budapest, 2003.

[6] Gellert Fledrich, Robert Keresztes, Gabor Kalacska: Evaluation of the machined surfaces of ZrO_2 ceramics, International Multidisciplinary Conference 10th Edition, Nyíregyháza 2013. 51-55.pp

[7] Valasek, I. – Tóth, I.: Megmunkálás tribológia. Tribotechnik Kft. Budapest, 2003.

[8] Bartz, W. J. und 70 Mitarbeiter. Kühlschmierstoffe und Zerspanung. Remingen Malmsheim, Expert-Veréag 2000-

[9] Valasek, I.: Tribológiai kézikönyv, Tribotechnik Kft. Budapest, 1996.

[10] Walter, A.: Potenzial von Kühlschmierstoffen gezielt nutzen. Trocken oder nass -wohin geht die Metallbearbeitung? VDI-Berichte 1635 VDI-Verlag Düsseldorf, S 33-47p. 2001.

[11] Leonard, P.: über die lichtelektrische Wirkung. Annalen der Physik 8. pp149-198.

[12] Jánosi L, Sárközi E, Földi L, Józsa N. Kopásvizsgálatok növényi olajjal. XI. Nemzetközi Pneumatika-Hidraulika Konferencia Miskolc, Magyarország, 2004.09.21-2004.09.23. Miskolc: 155-161. o.

[13] Barányi I, Czifra Á, Kalácska G: Height-independent topographic parameters of worn surfaces, Sustainable Construction & Design. Conference proceeding.Gent: Ghent University Laboratory Soete, 2011. pp.35-41.

Morphological algorythm for fast contour characterisation in white paprika sorting process

Zoltán GERGELY, János BEKE

Szent István University, Faculty of Mechanical Engineering,
Szent István University, Gödöllő

Abstract

This technical development can reduce the damage of agricultural products while the contamination and abrasive wear of the applied machine elements is lower. The most of the sorting machines is suitable for selecting roundish, sub-spherical vegetables and fruits (tomato, potato, apple, apricot, cantaloupe etc.) by applying the weight measurement. The function of the system is to qualify the paprika of which most important parameters are its size and shape – measuring them and processing the measured data have to be solved. The record of shape is realized by CCD photoelectric linear array sensors with the help of which the processing with regular accuracy can be provided.

Keywords

morphological algorithm, measurements, image processing, mechatronics

1. Introduction

The image processing starts with shooting and recording pictures. There are several usable options for this – conventional or infrared cameras, X-ray images and ultrasonic detectors as well. The image is usually an intensity picture or map which certain luminance values assigns to the individual points of the objects; the recorded picture may be analogous or digital. The picture analysis is useful, but induces many problematic effects [4].

A super-rapid pattern recognition system differing from the earlier practice is shown in the following paragraphs; it facilitates the picking processes of the sweet white paprika with acceptable accuracy.

2. Method

For achieving a suitable picking performance, the complete recognition of 3 or 4 peppers has to be provided in a second (that is 10,800 to 14,400 bell peppers per hour at a travel speed of 1 m/s). It requires an extremely high-speed picture processing system and, in addition to this, the amount of data to be processed is also multiplied according to the multi-directional mapping. The complete image processing and recognition process shown in Figure 1.
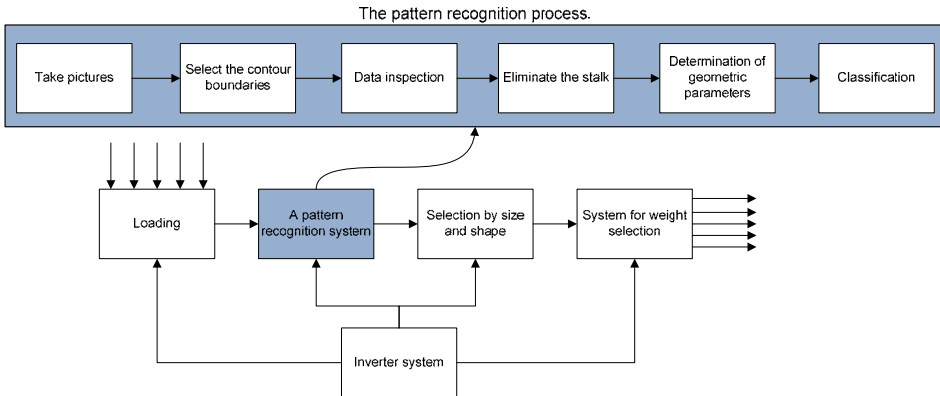
The pattern recognition process.

Figure 1. The complete paprika sorting process

It turned out during the investigations that the above demands can be satisfied only by the CCD sensor with a low pixel number – by the line CCD sensors (with the type used by us), the complete pixel data can be read out in 102 µs at the maximal read-out rate (Figure 2). An additional advantage is that the record of contour directly can take place; accordingly, the search of contour through software can be avoided and the recognition algorithm will be speeded up. To measurements used a general problem or target specific measurement system. Choosing the right solution is not always trivial [5].
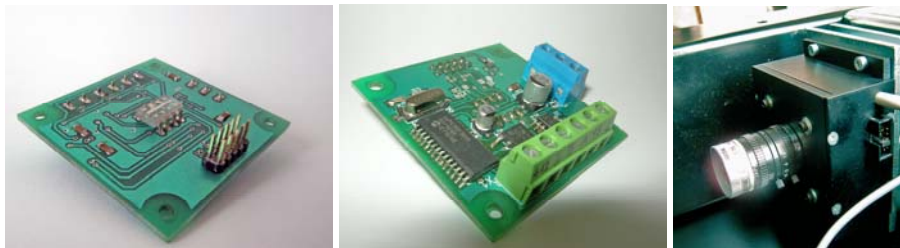

Figure 2. The used line CCD (left), the camera processor (middle)
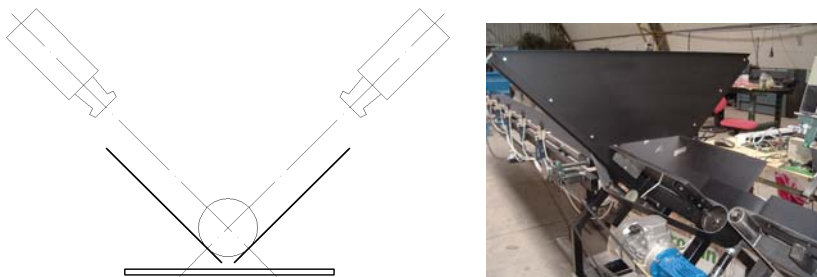and the boxed design (right)

Figure 3. Projection from two directions

To avoid the time-consuming rolling and moving of the crops, the projection has to be provided from several directions (Figure 3). It has been found in the course of our investigation that using more than two cameras does not improve significantly the accuracy, but greatly decreases the rate of processing.

3. Results

Under industrial conditions it is difficult to ensure that a good picture be created. There are many problems to be solved in the preparation and processing of images. The biggest problem is a low contrast ratio. This problem caused by shadows and dust. Both effects cause a significant reduction of the contrast. The standard, commonly used threshold algorithms have increased sensitivity of the shadows and dirt. This results in a significant reduction in accuracy. During this process it is very important to the strength and direction of illumination. In addition to these effects, the lighting inequalities need attention.

To resolve this problem, I created a self-developed algorithm for performing the analysis of images (Figure 4). This algorithm is based on the morphological analysis of image slices. Morphological analysis algorithm continuously analyzes the image slices from the cameras, and on the intensity function searches the key points. Faults can be due to the intensity difference can be eliminated completely (ideally). The figure shows that the morphological analysis algorithm finds very high accuracy to the actual edges. Test results of the composite image slices algorithm are shown in Figure 5.

Not only are the shadows and dirt can cause problems: The paprika color and the light source color temperature affects the accuracy of the algorithm, it requires additional tests and inspections. These tests are expected to be performed the near future.
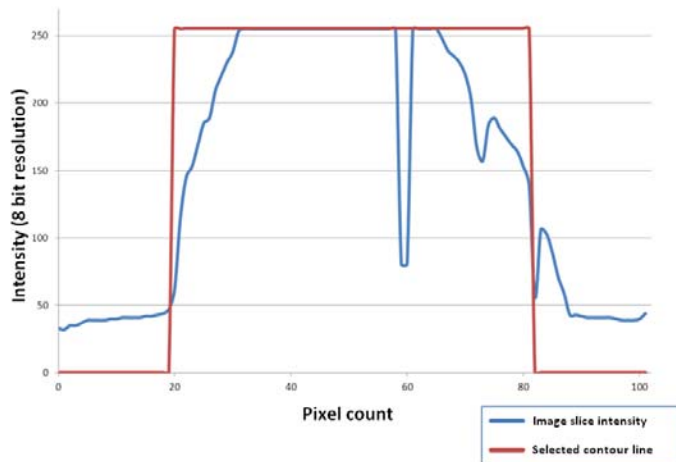

Figure 4. Results of self-developed morphological analysis of image slices
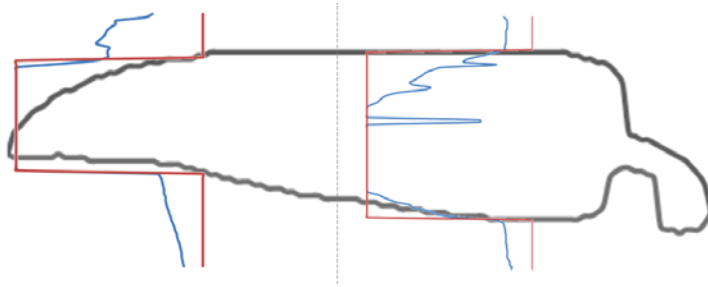
Figure 5. Result of the contour recording process

Not only the pepper dimensions are relevant, very important to specify the degree of deformation as well. The working of the determining the malformation algorithm in a very simplified form is as follows: As it was mentioned above, only the contour of the pepper is recorded during the measurement. The elimination (image rejection) of the stalk is a serious problem; it is solved by differential map identification process.

The first step for determining the malformation: The centre-line (purple line) is constructed and its length is accurately computed with small triangles. The values gained in this way are compared to the length of the line drawn between the first and the last centre points of the paprika body (black line). The quotient of the two length values is the centre-line curvature degree. By this method, the curvature invisible in profile also can be filtered out.
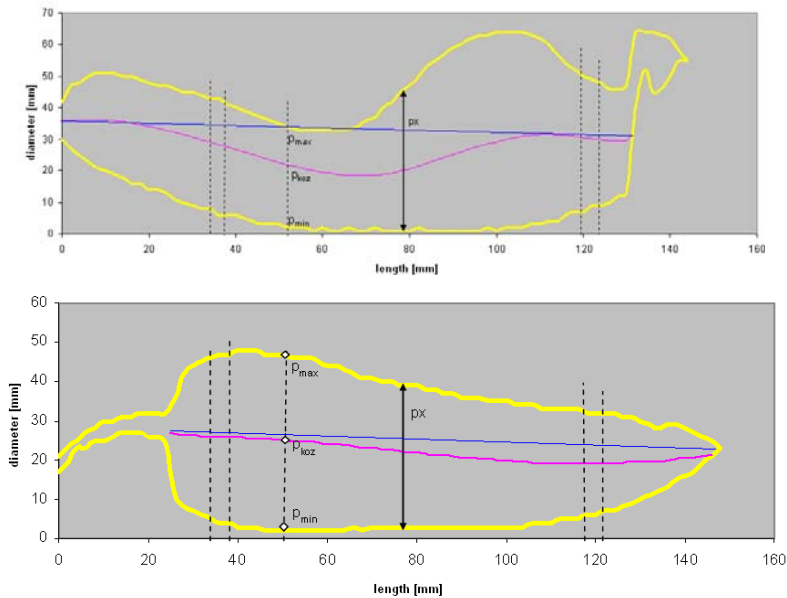

Figure 6. The contour recording process of a malformed
and an un-deformed bell pepper

If that is done, there is second step for determining the deformation: Determination of malformation continued by calculating the centre of gravity of plane figure. After that will be assigned to P_1, P_2, P_3 points, are defined in the γ_1 and γ_2 angle (Figure 7).

The ratio of the two angles determines the degree of deformity (G quotient), and direction. With this method, the small malformations are also determined (this is mainly important for long paprika, e.g. green hot peppers). For regular paprika (without malformation) the value of the coefficient is 1.

Because the determination of the center line length and direction does not give a clear result for malformation, so comparing the two quotient of these two steps is essential. In this way, the deformation rate gives us very quickly identify and accurate results.
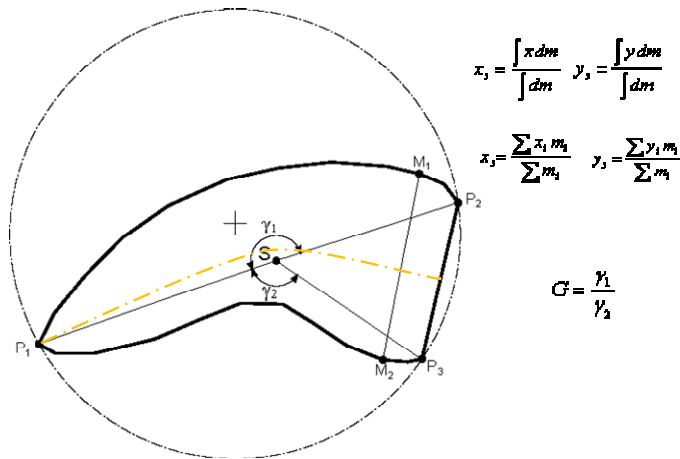

Figure 7. Determination of deformation.

Conclusions

The development of the measuring system was completed; the morphological analysis-based pattern recognition seems viable for the further applications as well. The correct determination of the parameters required by the standard is provided by the algorithm.

The designed measuring system and the algorithm very well performed its part during the long-term tests. The prototype system is working continuously at present as well; the evaluation of the data is also continuous.

Credits

References

[1] Gergely, Z., Judák, E. (2008): „A microcontroller based algorithm for sorting white paprika", Hungarian Agricultural Engineering, No. 2007-20. pp. 37-39. HU ISSN: 0864-7410

[2] Gergely, Z. – Judák, E. (2008): „Automatizált paprikaválogatás beágyazott alakfelismerő rendszerrel" Mezőgazdasági technika, XLIX. évf. 2008/11. HU ISSN: 0026-1890

[3] Gergely Z., Madár V., Judák E. (2007): Paprikaosztályozó rendszer kialakítása (Development of Paprika Classifying System) -MTA Agrárműszaki Bizottsága, Kutatási és Fejlesztési Tanácskozás XXXI. Gödöllő.

[4] Zsidai L., Keresztes R. (2010): Tribological behaviour and surface quality of polymeric industrial sealing materials. In: Jeroen Van Wittenberghe (cor.) Sustainable Construction & Design. Gent, Belgium, 2010.02.10, pp. 212-218. Paper 1.

[5] Földi L., Jánosi L. (2011): Test of the electro-rheological attributions of silicon oil without additives under flow mode. R & D Mechanical Engineering Letters, 2011.Vol 5., Hungary, pp. 121-127. HU ISSN 2060-3789, CD-ROM ISSN 2060-3797

[6] Gergely Z., Madár V., Judák E. (2006): Paprikaosztályozó berendezés a növényházi termesztésben - MTA Agrárműszaki Bizottsága, Kutatási és Fejlesztési Tanácskozás XXX. Gödöllő

On the influence of laser surface texture
in fretting fatigue testing

Jan DE PAUW, Wim DE WAELE,
Patrick DE BAETS

Department of Mechanical Construction and Production,
Ghent University

Abstract

One possible way to increase the lifetime of contacts subjected to fretting fatigue is to clear out wear particles from the contact. Therefore, the surface can be textured with small cavities capturing wear particles moving inside the contact. At Ghent University we designed a novel surface texture pattern specifically for mixed stick slip contacts in coupon scale fretting fatigue experiments. The influence of the new pattern on the fretting fatigue lifetime is compared to one other surface pattern and the virgin surface. Although the likelihood of capturing wear particles is increased, the lifetime of the new surface pattern is lower.

Keywords

Fretting fatigue, lifetime, surface modification, laser texture

1. Introduction

Fretting occurs when a small relative motion takes place between two prestressed bodies. Fretting causes surface degradation including small surface cracks in the contact and wear debris generation. Fretting in combination with ordinary fatigue accelerates the crack initiation and leads to a significant reduction in lifetime (Waterhouse 1972). The reduction in lifetime due to fretting fatigue can be counter by several palliatives. Common palliatives for fretting fatigue are: coatings (Fouvry, Kubiak et al. 2006), laser and shot peening (Liu and Hill 2009), deep rolling (Majzoobi, Azadikhah et al. 2009), low plasticity burnishing (Prevey, Ravindranath et al. 2006), micro topography (Volchok, Halperin et al. 2002).

The latter palliative, micro topography, increases the lifetime by evacuating the wear particles from the contact. Wear particles remaining in the contact participate in the fretting process and accelerate the damage process. By clearing the particles from the contact this acceleration will be tempered. Particles are cleared from the contact if they fall into the provided surface cavities. These cavities are made in a structured way on one surface at the contact area. This palliative is commonly seen in the field of gross sliding (Vilhena, Podgornik et al.) and fretting wear (Varenberg, Halperin et al. 2002) contacts. The large

sliding amplitudes during gross sliding (>300µm) and fretting wear (>30µm) ensures that all particles eventually fall into a cavity. However, the sliding amplitude during fretting fatigue is significantly smaller (<30µm) compared to the latter. This reduces the motility of the particles and decreases the likelihood of capturing particles. Anyway, the palliative of micro topography is used successfully in fretting fatigue research without taking into account the reduced mobility of the particles. The aim of this research is to design a new surface texture specifically for contacts dealing with small sliding amplitudes e.g. fretting fatigue.

2. Experimental details

Surface topography
Micro topo graphy as a palliative for fretting fatigue is successfully applied by Volchok et.al. (Volchok, Halperin et al. 2002). A similar pattern is used as a reference texture for this research. The contact area is laser textured with small spherical caps (cavities) in an organized manner, see figure 1, left. The shallow spherical caps have a diameter of 124µm and a depth of ~7µm. The coverage of the cavities is approximately 20%. The cavities are structured as shown in figure 1, left.

   Fretting wear particles move in the direction of the relative slip, horizontal in figure 1 (Diomidis and Mischler 2011). Particles between cavity 1 and 2 can fall into one of both cavity. However, particles below cavity 1 and 2 and above cavity 3 will never fall into a cavity. The likelihood of capturing a particle is not uniform and dependents on the position of the particle.
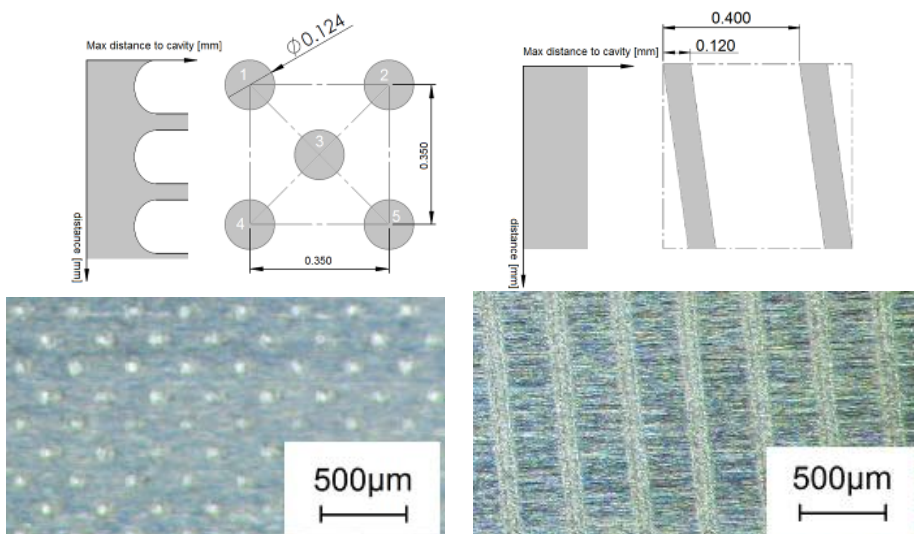

Figure 1. Surface patterns on specimens.
Left: point pattern; right: line pattern

A new pattern is designed with a more uniform likelihood of capturing particles, see figure 1, right. The new pattern is a line pattern with a coverage of 30%. The width of the lines is 120μm (spot size of laser) and the spacing is 400μm. The lines are under a small angle of 10°. Every particle can be captured with the line pattern, independent of the location of the particle. The line pattern shows a more uniform likelihood of capturing particles compared to the point pattern.

The surface textures are applied with a commercial laser texture machine Trumpf Trumark 5040. The YB-YAG fiber laser has an average power of 33 W and a peak pulse power of 20 kW. The pulse frequency was set at 28 kHz leading to a pulse width of ~230 ns. The spot size of the used laser is ~114μm without defocus or additional optics. The point pattern is applied by a single shot ablation process which is repeated twice in order to obtain the desired depth. The line pattern is applied with the same parameters what leads to a marking speed of ~1000m/s.

Fretting fatigue test setup and sample material
Twenty-three fretting fatigue experiments are performed on three types of specimens. The specimens are finished with three different surface textures: a virgin surface, a laser textured point pattern and a laser textured line pattern. The general geometry of all the specimens (dogbone and pad) is identical and shown in figure 2, right.

The fretting fatigue experiments are performed on a custom test rig, see figure 2 left. (De Pauw, De Baets et al. 2013). During a test are the cylindrically ended pads prestressed against the dogbone specimen with a constant normal load $F_N = 543N$. A fatigue force F_{fat} is applied on the dogbone specimen with a frequency of 10Hz, a load ratio $R_\sigma = 0.1$ and seven maximum forces (*4; 4,6; 5,4; 6,4; 7,6; 8,2; 8,8 kN*). The experiments are performed in 'dry' contact conditions and in ambient conditions.
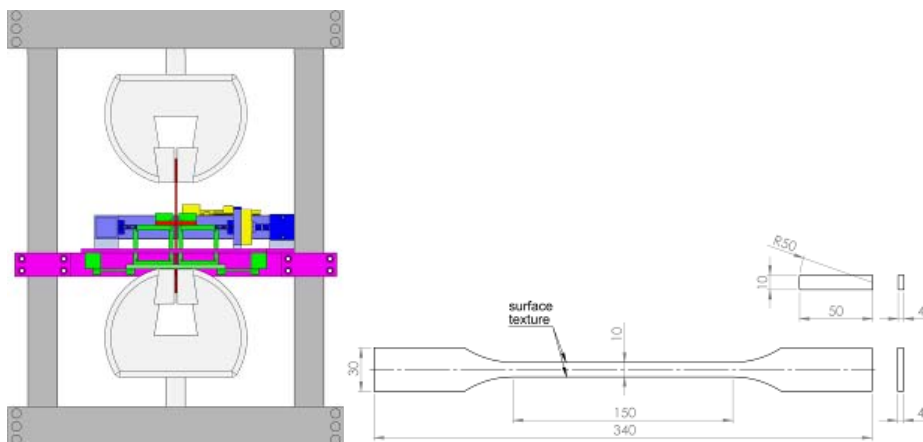

Figure 2. Schematic overview of the fretting fatigue test setup and specimens [mm]

3. Results and discussion

Surface texture
The surface topography of the line pattern is characterized with a 3D profilometer (Somicronic EMS Surfascan 3D). The laser ablation process made the desired cavities (figure 3, *w* and *d*), but also has a side effect. Adjacent to the cavities are high protrusions of material formed (figure 3, *h*). These high peaks give high stress concentrations in the contact and hinder the fretting wear particles to fall into the cavities. The height of these surrounding peaks is reduced by very superficial sanding of the surface with steel wool.
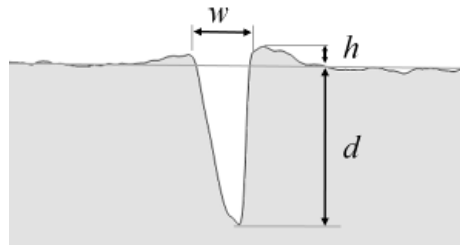

Figure 3. 2D Surface cavity after laser texturing and grinding

The influence of the superficial sanding can be seen in figure 4 and table 1. Before sanding is the height of the peaks (7.06 ± 0.72 µm) comparable to the depth of the cavities (7.11 ± 0.48 µm). After sanding is the height of the peaks reduced with a factor five to the value of 1.47 ± 0.06 µm which is lower than the total surface roughness $R_T = 1.96 \pm 0.63$ µm of the virgin surface.

The line pattern and the point pattern are textured with identical laser parameters. The equal laser spot size gives rise to a similar width of the line pattern and diameter of the point pattern (~124µm). The same energy per pulse and similar amount of repetitions (two) leads to a comparable depth for the line pattern and the point pattern (~7µm).

Table 1. Micro geometrical dimensions of the laser textured specimens

Pattern type	Surface condition	Depth d [µm]	Height h [µm]	Width w [µm]
Point pattern	As laser marked	7.41 ± 0.39	2.80 ± 0.10	128.14 ± 7.84
	As tested	7.27 ± 0.28	1.30 ± 0.22	126.14 ± 5.67
Line pattern	As laser marked	7.11 ± 0.48	7.06 ± 0.72	121.47 ± 7.14
	As tested	7.68 ± 0.32	1.47 ± 0.06	119.13 ± 8.15

The used laser has a pulse width in the range of nano-seconds to limit the amount of heat input in the specimens. A large heat input would cause

microstructural changes under the ablated volume, locally weakening the material. Figure 5 shows the microstructural examination of the point pattern and the line pattern. The micrographs are taken perpendicular to the line contact and at mid-thickness of the dogbone specimen. The shallow cavities are clearly observable for both surface patterns. The depth of the cavities is smaller than the grain size of the material ($\sim 170 \pm 83 \mu m$) so the aluminum grains are not intersected. Underneath the cavities is no microstructural change detected suggesting that the material strength persisted unchanged.
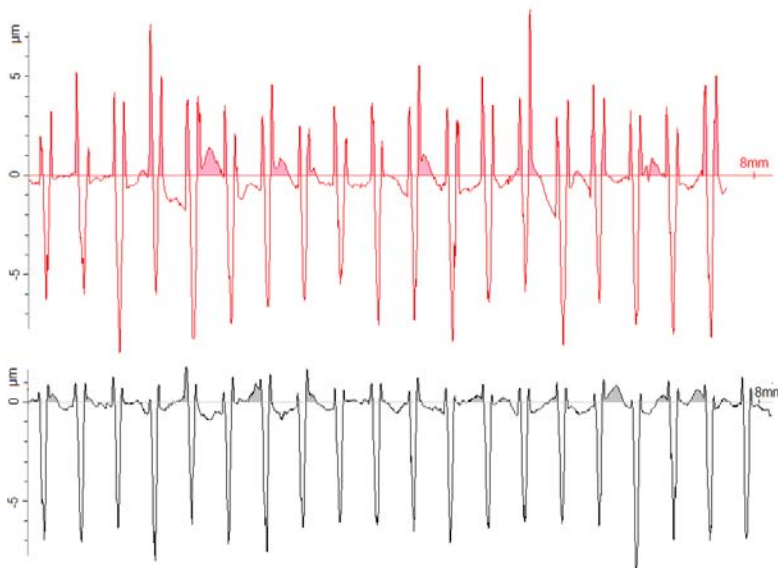

Figure 4. 2D Surface profile of the line pattern.
Top: as laser marked; bottom: as tested (identical scales)

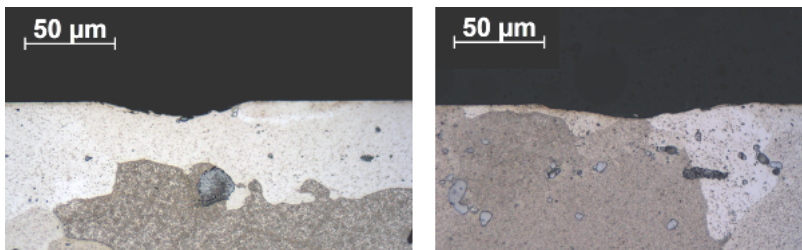*Figure 5.* Microstructural images of the surface patterns. Left: point pattern; right: line pattern

Fretting fatigue experiments
Fretting fatigue experiments are performed to measure the influence of the three surface textures on the fretting fatigue lifetime. The lifetime *N* is measured as the number of fatigue cycles until complete failure of the dogbone specimen.

The measured lifetimes varying between 45000 cycles and $1,4 \times 10^6$ cycles (high cycle fatigue). All cracks initiated in the contact area at the side of the applied fatigue force, left in figure 6, as known from literature (Hills and Nowell 1994). However, the line patterned specimens reveal a noticeable different behavior of crack initiation. Generally, the cracks initiate rather irregularly shaped as observed on the specimens with a virgin surface and point pattern surface, in figure 6 respectively left and middle. In contrast, all the cracks in the line patterned specimens grow along the laser textured line, see figure 6 right.

The stress concentration factor of the line pattern is very small (near one) just as the stress concentration factor of the point pattern (Pilkey 1997). However, the patterns are completely different. A crack initiated in a line of the line pattern will preferably grow along the contiguous line which has a slightly higher stress concentration factor. While a crack initiated in a spherical cap of the point pattern (or on the virgin surface) has no pronounced direction with an increased stress concentrations and consequently no pronounced direction of crack growth.

Figure 6. Fretted area after failure (F_N=543N, F_{fat}=8.8kN).
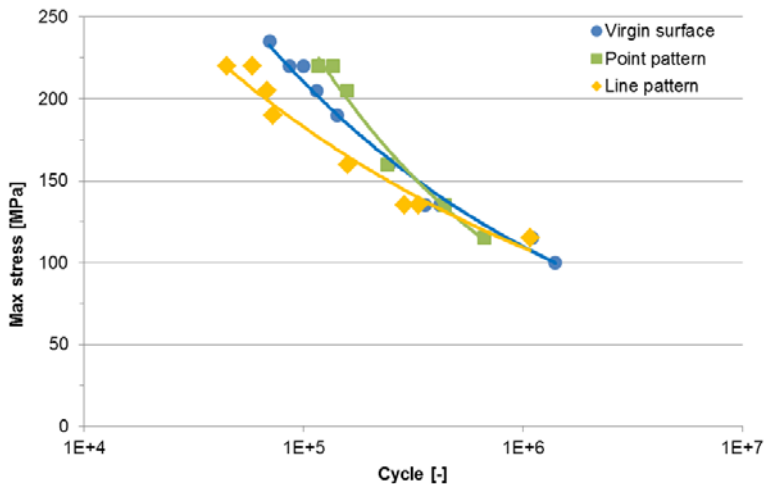Left: virgin; middle: point pattern; right: line pattern

Figure 7. Lifetime of fretting fatigue experiments on a virgin surface
and two laser patterned surfaces

The fretting fatigue lifetime of the three surface textures can be seen in figure 7. At low stresses and high number of cycles, $\sim 10^6$, there is no measurable

influence of the surface texture on the lifetime. Though, at higher stresses and lower number of cycles, $\sim 10^5$, there is a significant influence of the surface texture on the lifetime. The point pattern gives a 36% higher lifetime compared to the virgin surface. In contrast, the line pattern results in a 44% lower lifetime compared to the virgin surface.

Conclusions

This study describes a new surface texture pattern as a palliative for fretting fatigue. The new pattern is a line pattern with a very uniform likelihood of capturing wear particles moving in the contact. The new pattern is compared to a point pattern of spherical caps which is successfully been used in literature. Both patterns are applied with the same laser on aluminum 2024 T3 specimens. The micro geometry of both patterns is comparable: similar depth and width (and incidental height). Underneath the laser ablated cavities is no microstructural change observed for both patterns.

The fretting fatigue lifetime of both patterns is compared to the lifetime of a virgin surface. At one million cycles there is no significant difference between the patterned surfaces and the virgin surface. However, in the range of 10^5 cycles we observe a significant difference. The lifetime of the point pattern is 36% higher compared to the virgin surface. In contrast, the new line pattern shows a 44% decrease in lifetime compared to the virgin surface. Although the likelihood of capturing particles is more uniform, the fretting fatigue lifetime decreases. The likelihood of capturing particles is less important than the manner in which the cavities are designed. In particular, contiguous cavities (lines) appear to work as a predefined path of slight stress concentration, accelerate the crack propagation and reducing the total lifetime.

Nomenclature

d	depth μm	
F_{fat}	fatigue force	kN
F_N	normal force	N
h	height	μm
N	number of cycles to failure	-
R_T	total surface roughness	μm
R_σ	load ratio	-
w	width	μm

Acknowledgements

VAC Machines (Bruges, Belgium) is thanked for his assistance concerning laser texturing.

References

[1] De Pauw, J., P. De Baets, et al. (2013). Design of a fretting fatigue test rig with compliant springs. Sustainable construction & design. S. Hertelé. Ghent, Belgium, Ghent University, Soete laboratory.
[2] Diomidis, N. and S. Mischler (2011). "Third body effects on friction and wear during fretting of steel contacts." Tribology International 44(11): 1452-1460.
[3] Fouvry, S., K. Kubiak, et al. (2006). "Behaviour of shot peening combined with WC-Co HVOF coating under complex fretting wear and fretting fatigue loading conditions." Surface & Coatings Technology 201(7): 4323-4328.
[4] Hills, D. A. and D. Nowell (1994). Mechanics of fretting fatigue.
[5] Liu, K. K. and M. R. Hill (2009). "The effects of laser peening and shot peening on fretting fatigue in Ti-6Al-4V coupons." Tribology International 42(9): 1250-1262.
[6] Majzoobi, G. H., K. Azadikhah, et al. (2009). "The effects of deep rolling and shot peening on fretting fatigue resistance of Aluminum-7075-T6." Materials Science and Engineering: A 516(1-2): 235-247.
[7] Pilkey, W. D. (1997). Peterson's stress concentration factors /Walter D. Pilkey, Wiley.
[8] Prevey, P. S., R. A. Ravindranath, et al. (2006). "Case studies of fatigue life improvement using low plasticity burnishing in gas turbine engine applications." Journal of Engineering for Gas Turbines and Power-Transactions of the Asme 128(4): 865-872.
[9] Varenberg, M., G. Halperin, et al. (2002). "Different aspects of the role of wear debris in fretting wear." Wear 252(11-12): 902-910.
[10] Vilhena, L., B. Podgornik, et al. "Influence of texturing parameters and contact conditions on tribological behaviour of laser textured surfaces." Meccanica 46(3): 567-575.
[11] Volchok, A., G. Halperin, et al. (2002). "The effect of surface regular microtopography on fretting fatigue life." Wear 253(3-4): 509-515.
[12] Waterhouse, R. B. (1972). Fretting Corrosion. London, Pergamon Press.

Carbon nanostructures behavior on the strength of different atomic force function

Tamás PATAKI, Attila KÁRI-HORVÁTH

Institute for Mechanical Engineering Technology
Szent István University, Gödöllő

Abstract

Molecular mechanics studies were performed on structures consisting of Y junctions of carbon nanotubes. Tensile simulations were run on the same structure, wherein atomic force functions of various shape were used. According to the numerical test results the behavior of the structure, the failure site and the failure process could be determined irrespective of the shape of the force function.

Keywords

nanostructure, force function, Y junction

1. Introduction

Because of their derivation from graphene structures (winding of graphene ribbon) carbon nanotubes may be materials with a strength value approaching the theoretical maximum achievable in solids. Direct determination of the strength of carbon nanotubes has been performed on multiwall carbon nanotubes (MWCNT) (Demczyk 2002, Yu 2000a), and on bundles of single wall carbon nanotubes (SWCNT) (Yu 2000b). One can say of such experiments that these are very cumbersome and expensive tests that can be performed on simple carbon structures and the accuracy of the tests, thus the correctness of the obtained results is not yet clear. In every respect of mechanical stress no matter the buildup of the construction, that it is symmetric or not. (Z. Szakál 2008)

In order to determine the tensile strength of individual carbon nanotubes theoretically the methods of molecular mechanics are used. The basis of this that the interatomic binding forces can be calculated from the gradient of the potential function describing the energetics of chemical bonds. In most of such calculation the empirical Brenner potential (Brenner, 1990, 2002) has been used (Belytschko 2002, Mylvaganam 2004, Duan 2007, Fu 2008, Agrawal 2008).

In the original Brenner formulae at a certain interatomic distance there is a discontinuity in the potential function which causes problems in the atomic force function because of the sudden change of the slope. Neither this sudden slope change, nor the multiplication of the maximum atomic force due to the slope change can be explained by physical reasons. This change can modify the

behavior of any composite material (Andó 2004, 2008a, 2008b, 2009; Kalácska 2007).

In order to avoid the sudden change of slope a correction function has been introduced (Zsoldos 2009). The correction function has been defined by polynomials having adjustable parameters, and by means of these freely adjustable parameters the atomic force function can be fitted to the test results. As, however, the accuracy of the test results is not known, the usefulness of adjustment to the test results has not been decided either.

In this work it is investigated how can molecular mechanics simulations using the Brenner potential be used for the study of more complicated carbon nanostructures, such as Y junctions.

2. Algorithm

In the modified Brenner formulae they were used the following correction function (Zsoldos 2009):

$$f_{ij}(r) = \begin{cases} f_1(r), & R_1 \leq r \leq R_T \\ f_2(r), & R_T < r \leq R_2 \end{cases} \tag{1}$$

where R_T is the position of the inflection point between R_1 and R_2, r is the interatomic distance between two neighbor atoms.

$f_1(r)$ and $f_2(r)$ functions defined in two distinct intervals are polynomials of the fourth and third order respectively:

$$f_1(r)=a_0+a_1r+a_2r^2+a_3r^3+a_4r^4, \ f_2(r)=b_0+b_1r+b_2r^2+b_3r^3 \tag{2}$$

The coefficients of the polynomials have been determined by fitting them to the Brenner potential:

$$b_3 = \frac{f_T}{2(R_2 - R_T)^3} \quad a_4 = \frac{3f_T - 3 + 6b_3(R_2 - R_T)^2(R_T - R_1)}{(R_T - R_1)^4} \tag{3}$$

$$a_3 = \frac{4a_4\left[R_T^3 - R_1^3 - 3R_T^2(R_T - R_1)\right] + 3b_3(R_2 - R_T)^2 + d}{3(R_T - R_1)^2} \tag{4}$$

$$b_2=-3b_3R_T, \ a_2=-3a_3R_T-6a_4R_T^2, \ a_1=d-2a_2R_1-3a_3R_1^2-4a_4R_1^3 \tag{5}$$

$$\begin{aligned} b_1 &= d-2b_2R_2-3b_3R_2^2, \\ a_0 &= 1-a_1R_1-a_2R_1^2-a_3R_1^3-a_4R_1^4, \\ b_0 &= -b_1R_2-b_2R_2^2-a_3R_2^3 \end{aligned} \tag{6}$$

f_T in the expressions for the coefficients of the polynomials is the value of the correction function at the inflection point (at R_T). Variables R_T and f_T are freely adjustable parameters.

In this work it has been investigated how does the behavior of carbon nanostructures change, if the shape of the potential energy function and, consequently the shape of atomic force function is varied.

When varying the shape of the energy potential function and the atomic force function 7 different cases were investigated. In the first case the $f_{ij}(r)$ function was removed from the Brenner formula, i.e. it was assumed that its value is 1 in each case. In the next 6 cases 6 different value pairs were selected for R_T and f_T for the $f_{ij}(r)$ correction function, thus we generated 6 different atomic force functions. Figure 1 shows these 6 different cases. The differences between the energy potential functions are smaller, the variation of the free parameters in the atomic force function, however, results in more drastic changes. The question is really relevant: what changes are caused by the variation of the atomic force function in the behavior of carbon nanostructures?
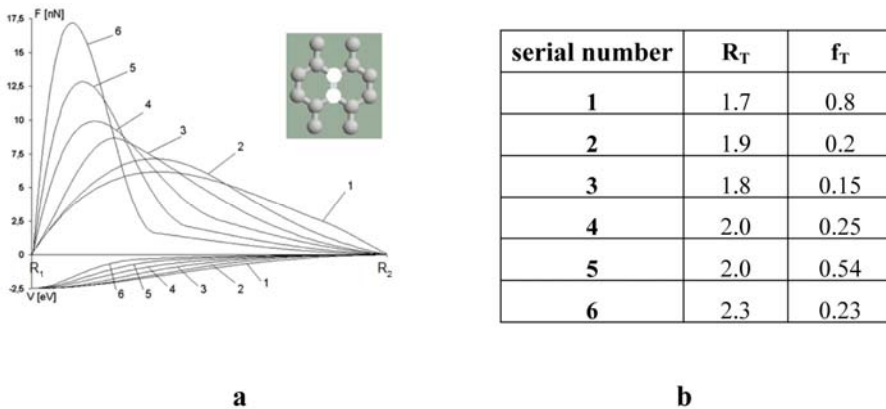

serial number	R_T	f_T
1	1.7	0.8
2	1.9	0.2
3	1.8	0.15
4	2.0	0.25
5	2.0	0.54
6	2.3	0.23

a **b**

Figure 1. a.) Below the abscissa the energy potential function, above the abscissa the atomic force function is shown, calculated between two adjacent atoms (indicated by white color) b.) Freely chosen parameters of the correction function.

3. Tensile simulation of carbon nanotube Y junction

Seven tensile simulations were performed by using the atomic force functions described in the previous paragraph. The tensile simulations were performed on the same structure consisting of two Y junctions opposing each other, as shown in Fig. 2a. These models of opposing Y junctions were built from zigzag type nanotubes, the chiral vector being (6, 0). During the tensile simulation axial tensile forces were applied at the ends of the four straight tube portions, as shown in Fig. 2b. Simulations were run until the appearance of deformation (failure).

In the first case the original Brenner potential was used, where the effect of „cutting" or correction function was not taken into account, its value was assumed to be invariably 1. During the tensile simulation process the position was identified where the structure was deformed.

Afterwards the effect of the correction function was determined using 6 different pairs of the freely chosen parameters. By this set of simulations we wanted to explore how much is it necessary to adjust the atomic force functions to exact experimental results in order to determine the weakest points.
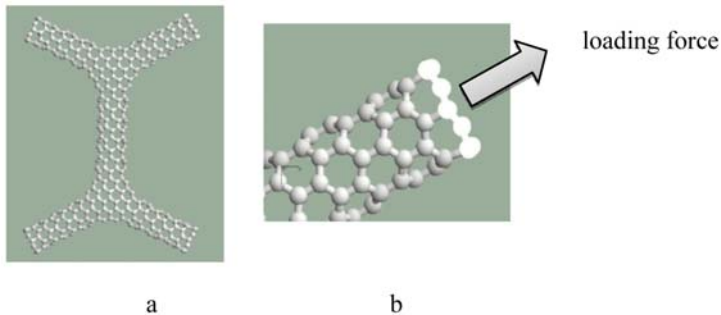

loading force

a   b

Figure 2. a.) the initial structure b.) The axial force applied at the ends
of the straight portions of the tubes

Fig. 3 shows the results of the calculation run with the original Brenner potential. The run was finished when the failure site was identified on the structure. This state was achieved when the elongation in all 4 branches reached 11.26 Å. This corresponds to 38% elongation. From the geometry of the structure it follows that two, symmetrically occurring failures can be observed. The deformations did not appear in the junction sites (nodes) but in the straight tube portions. It can be seen at higher magnification that certain bonds broke, some others are rearranged.
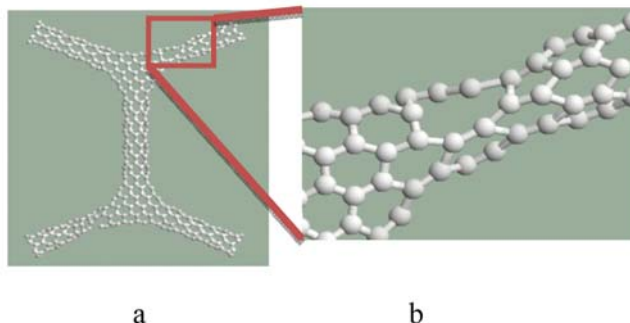

a   b

Figure 3. a.) The failed structure investigated by the original Brenner potential, b.)
At higher magnification one can see the broken bonds

TRANS-TRIO SCIENCES
*Carbon nanostructures behavior on the strength of
different atomic force function*

In the following the results of the runs performed using the correction functions determined by the 6 freely chosen parameter pairs mentioned above are shown (see Figs. 4a-4f).
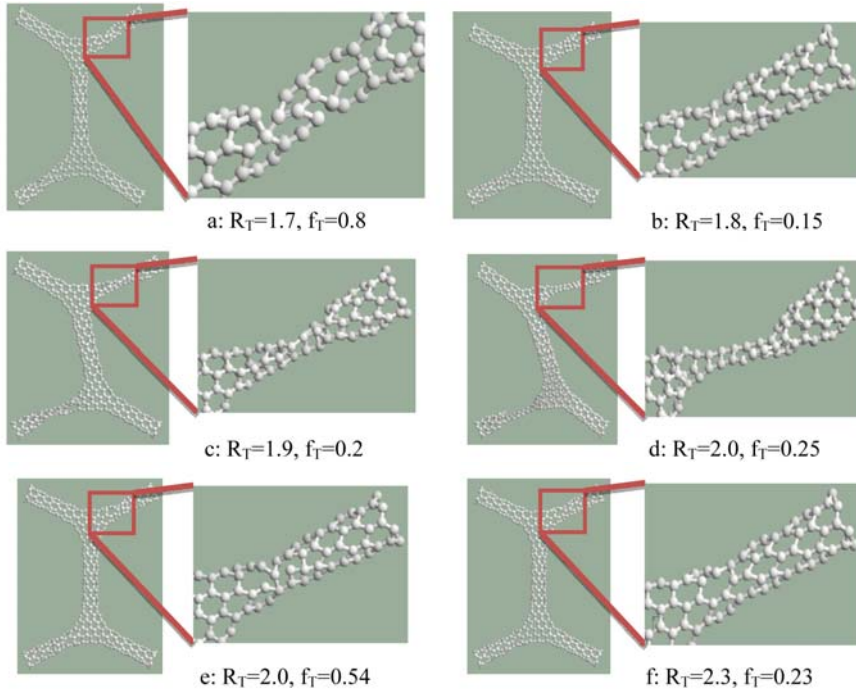

a: $R_T=1.7$, $f_T=0.8$

b: $R_T=1.8$, $f_T=0.15$

c: $R_T=1.9$, $f_T=0.2$

d: $R_T=2.0$, $f_T=0.25$

e: $R_T=2.0$, $f_T=0.54$

f: $R_T=2.3$, $f_T=0.23$

Figure 4. Results of the calculations performed using correction functions determined by different pairs of parameters

During the test runs it has been established that the failure occurs at the same structural unit, even at the same location (in the neighborhood of the same atoms). In all cases the deformation developed at the location observed in the first run. The shape of the atomic force function does not modify the failure location.

References

[1] Andó Mátyás, Kalácska Gábor, Czigány Tibor Agrawal P.M., Sudalayandi B.S., Raff L.M., Komanduri R., Comput. Mater. Sci. 41:450-45, 2008a.
[2] Belytschko T, Xiao S.P., Schatz G.C., Ruoff R., Phys. Rev. B 65:235430-1-8, 2002.
[3] Brenner D.W., Phys. Rev. B 42:9458-9471, 1990.
[4] Demczyk B.G., Wang Y.M., Cumings J., Hetman M., Han W., Zettl A., Ritchie R.O., Mater. Sci. and Eng. A 334:173-178, 2002.

[5] Duan W.H., Wang Q., Liew K.M., He X.Q., Carbon 45:1769-1776, 2007.

[6] Fu C.X., Chen Y.F., Jiao J.W., Sci. in China E 50:7-17, 2008.

[7] G. Kalácska, L. Zsidai, R. Keresztes, A. Tóth, M. Mohai, J. Szépvölgyi Wear 290-291. (2012) pp. 66-73.

[8] G. Kalácska, L. Fazekas, R. Keresztes, A Tóth, J. Szépvölgyi Applied Surface Science. 257 (2011) pp. 9532-9538.

[9] Kalácska Gábor, Andó Mátyás, Deák Ferenc, Sárosi Gyula FVM Mező-gazdasági Gépesítési Intézet, 2007. 3. kötet 195-199 p.

[10] Kalácska G.: EXPRESS Polymer Letters Vol.7, No.2 (2013) pp. 199-210. DOI: 10.3144/expresspolymlett.2013.18

[11] Keresztes R., Kalácska G.: Sustainable Construction & Design. 2010. Vol.1. p. 136-144. ISSN 2032-7471, ISBN 978-9-49072-600-3

[12] Mátyás Andó, Gábor Kalácska, Tibor Czigány Synergy and Technical Development, Gödöllő 2009 o6-199 1-6p.

[13] Mátyás Ando, Gabor Kalacska, Tibor Czigany Erősített Műanyagok 2008 Nemzetközi BALATON Konferencia, Keszhely 2008b. 1-9 p.

[14] Mátyás Ando, Gabor Kalacska, Tibor Czigany Mylvaganam K., Zhang L.C., Carbon 42:2025-2032, 2004.

[15] Yu M.F., Files B.S., Arepalli S., Ruoff R., Phys. Rev. Lett., 84:5552-5555., 2000b.

[16] Yu M.F., Lourie O., Dyer M.J., Moloni K., Kelly T.E., Ruoff R.S. Science, 287:637-640, 2000a.

[17] Z. Szakal, I Zsoldos, International journal of mathematical models and methods in applied sciences 4:(2) pp. 523-532. (2008).ISSN: 1998-0140

[18] Zsoldos I., László I., Carbon 4(7):1327–1334, 2009.

Study regard to use pistons with ceramic crown construction spark ignition engines

Ioan Radu ŞUGAR, Mihai BANICA, Nicolae UNGUREANU

Engineering and Technological Management Department,
Technical University of Cluj Napoca,
North University Center of Baia Mare, Baia Mare

Abstract

In the current internal combustion, engine specialists seeking ways to improve comparative indices. Just as in the aerospace industry, the use of ceramic materials can be a solution.

Keywords

engine, materials, ceramic, combustion.

1. Introduction

As techno-economic importance, ceramic materials are placed right after metals and plastics. If traditional ceramics (glass, tile, porcelain) has been used and produced from ancient times, technical ceramics, also known as „Fine Ceramics" or „advanced ceramics" has developed as material in the last 60-65 years.

The main categories of technical ceramic materials currently taken into account to be used for construction of heat engines are: silicates, silicon carbides, titanates, silicon nitrides, zirconium oxides.

These materials have undergone complex research studies on their structure, its reflection on physicochemical properties, on functional behaviour to mechanical, thermal, chemical stress, and their combinations, to thermal shock, thermal fatigue, and aging phenomena in exhaust gas.

There have also been studied structural changes that may occur due to conditions of use and specific issues of fracture mechanics (Băţaga et al., 2000).

The examination of the structure of materials has been based on: chemical and spectrographic analyses, determinations of physical properties, structural analysis from electron micrographs and scanning electron microscopy, determination of crystalliform slots through X-ray diffraction (Şugar, 2007).

Ceramics plasticity is very limited (Figure 1 and Figure 2) so that these materials deform elastically up to brittle fracture due to their structure of heterogeneous crystalline groups, thus with fewer slip planes than those of metals, which indicates that in moderate temperatures plastic deformations are absent.

Aluminium titanate is characterized by ionic bonds with their basic structural element similar to the octahedron found in the titanium oxide.

This translates into brittleness lower than those of silicates but also through a less impressive mechanical strength.

Zirconia is relevant to the engine parts because, of all the ceramics produced so far, it has its expansion coefficient nearest to that of the metal, it is a good thermal insulator and it allows to be reinforced (Chiru at al., 1999) (Fledrich at al. 2011).
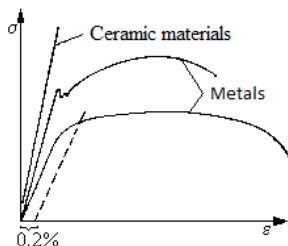

Figure 1. Curves of tension σ - unit deformation ε
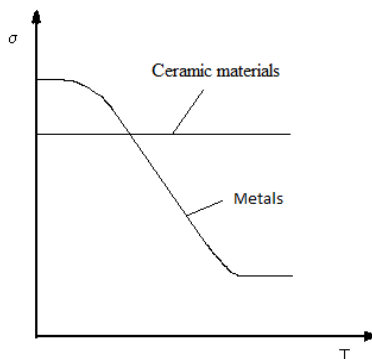of ceramic materials and metals

Figure 2. Mechanic resistance variation depending on temperature

In the case of internal combustion engines by using ceramic materials, the effect that these have on inertia and gas pressure during engine operation is studied.

Ceramic materials can be used in severe working conditions such as pumps and turbines used in the petrochemical industry, internal combustion engines, shipping and aerospace.

Operation must take into account a range of issues such as: vibration, the thermo-hydrodynamics of the lubricant film, the heat transfer, vaporization of the lubricant film, the shape of surfaces.

The researches have led to results concerning thermo-hydrodynamic lubrication between mating surfaces. With the help of infrared rays, an

experimental study of the temperature field between surfaces can be accomplished.

In order to determine the behaviour in service of the parts made of ceramics materials, flexibility has been taken into account. The results have included the influence of the studied parameters such as: constructive shape, lubricant film, viscosity, static and dynamic balancing.

Structural ceramic materials maintain their properties at elevated temperatures, they have a relatively large resistance to breakage, corrosion (comparable to that of stainless steels) and a high resistance to thermal shock, and they also have a low conduction coefficient (Şugar, 2007).

The technique used for the production of ceramic materials is based on sintering applicable in several variants.

2. Experimental research

For the experiment, ceramization of the piston and valve spark ignition engine has been chosen. Ceramization consists in isolating the piston crown and the ceramic valves with ceramic material (alumina, Al_2O_3). It corresponds to thermal and mechanical demands of MAS in general, it can be obtained by sintering almost to final shape; it has the coefficient of linear thermal extension close to that of the base material and it has a low price compared to other ceramic materials (aluminium titanate).

If at first were made full ceramic pistons due to poor reliability and tribological deficiencies were fabricated composite pistons made of two parts, one metal and one ceramic (Figure 3). The metal remains at a lower temperature and develops strength, high temperature ceramics, and is working on thermal barrier.

Figure 3. Ceramic piston crown

Since the expansion coefficient ratio between metal and ceramic materials is relatively high (sometimes over 10:1) is required for ceramic crown of the piston to choose a ceramic material having a coefficient of expansion as close to the base material.

A long period of time the silicon carbide ceramic material has been used in the manufacture of various internal combustion engines ceramizate. To increase the quality and reliability of internal combustion engines ceramizate, alumina (Al_2O_3) can be a solution.

To prove this both materials were heated with oxyacetylene flame and were cooled with a fan. Temperature measurement was done with a non-contact thermometer, IR (-50÷+1200 °C) in the infrared, as shown in Figure 4.

Figure 4. Contactless Thermometer IR (-50÷+1200ºC)

The test results are shown in Table 1.

Table 1. Coefficient of thermal expansion
of Al2O3 vs. SiC

Nr. Crt.	T, K	α_{Al2O3}, K^{-1}	α_{SiC}, K^{-1}
1	373	6,2	3,5
2	473	7	4
3	573	8	4,5
4	673	8,4	4,8
5	773	9	5,1
6	873	9,5	5,8
7	1173	9,6	6
8	1473	9,8	6,5

Figure 4 shows comparative evolution of the thermal expansion coefficient of temperature based on alumina or silicon carbide.
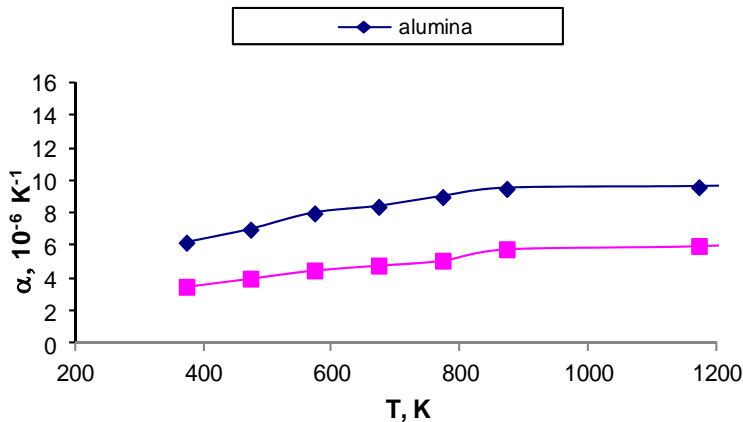
Figure 5. The variation of the coefficient of linear thermal expansion
for alumina and silicon carbide

The maximum temperature is recorded in the piston head. Thus it can reach 583 K for aluminum alloy piston (Burnete at al., 2001).

In case of ceramic piston crown, in the zone of the contact between the crown and the base material temperature does not exceed 533 K [Şugar, 2007]. Between 473 and 573 K the coefficient of linear thermal expansion of the material ranges from 21 to 23.8×10^{-6} K^{-1} [Grűnwald, 1980]. Analyzing the experimental results it is observed that to achieve required alumina ceramic crown against silicon carbide due to linear expansion coefficient close to that of the base material.

Conclusions

1. Ceramic materials can not completely replace metallic materials; their main drawback is the fragility;
2. Better results can be obtained using composite materials;
3. Component parts can be fabricated using alumina has a coefficient of thermal expansion of the material of the piston.

References

[1] Băţaga, N., Burnete, N., Barabas, I., Căzilă, A., Filip, N., Naghiu, A. and Dan, F. (2000), Motoare cu ardere internă. Combusibili, lubrifianţi şi materiale speciale pentru automobile. Economicitate şi poluare. Editura U.T. Press, Cluj-Napoca.
[2] Burnete, N., Băţaga, N. and Karamusantas, D. (2001), Construcţia şi calculul motoarelor cu ardere internă. Editura Todesco, Cluj-Napoca.

[3] Chiru, A., Anca, H.R., Cofaru, C., Kuchar, R., Soica, A. and Ispas, N. (1999), Materiale compozite, vol I. Editura Universității Transilvania, Brașov.

[4] Fledrich G., Pálinkás I., Keresztes R., Szabadi L., Kalácska G. (2011): Turning of zirconium-dioxide ceramics. Mechanical Engineering Letters. 2011. Vol.5. pp 44-57.

[5] Grűnwald, B. (1980), Teoria, calculul şi construcţia motoarelor pentru autovehicule rutiere. Bucureşti, Editura Didactică şi Pedagogică.

[6] Şugar, I.R. (2007), Utilizarea materialelor ceramice în arhitectura camerelor de ardere a motoarelor cu aprindere prin scânteie. Editura Risoprint, Cluj-Napoca.

Comparative analysis of the results of measuring roundness

Imre NÉMEDI[1], Gellért FLEDRICH[2], Miodrag HADŽISTEVIĆ[3],
Janko HODOLIČ[3]

[1]Polytechnical College of Subotica, Marka Oreskovića 16, Subotica, Serbia
[2]Institute for Mechanical Engineering Technology,
Faculty of Mechanical Engineering Szent István University, Gödöllő,
[3]University of Novi Sad, Faculty of Technical Sciences

Abstract

Coordinate measuring machines are devised for most complex measurements. Besides their dimension measuring abilities, the CNC operated machines can measure geometrical characteristics of form, such as straightness, roundness, cylindricity, etc. These are vital features in current times when control needs to submit very thorough reports not only on the form, but also on the geometrical features of the given workpiece. Yet the question arises: are these measuring data regarding roundness received from the CMM accurate and reliable enough for them to be exploited?

In order to confirm this statement, the geometrical roundness characteristics are measured on three types of coordinate measuring machines, the results of which are analyzed from several aspects.

The results have shown a special importance of specific measuring parameters and have shown to be independent of the type of measuring machines.

Keywords

coordinate measuring machines, measuring roundness, circularity.

1. Introduction

A workpiece from dimensions all workpieces have certain micro and macro geometrical surface characteristics. For deviation from dimension and macro geometrical characteristics of form, location, and direction there are functional limitation which, if they are overstepped, this may endanger the functionality of the workpiece. The tolerances on the drawings (PLANS, DESIGNS) have to completely ensure the dimensions and geometrical form, so that nothing is left to subjective evaluation of the factory staff or the controll service.

The forms of the real surfaces regularly have a certain degree of deviation in comparison to the geometrically ideal surfaces. The causes of deviation basically match with the causes of inaccuracy of measuring workpieces. Functional dimensions are always done with a certain degree of tolerance that simultaneously limit the form deviation of that workpiece.

If one needs a greater degree of precision, than the one provided by the tolerance level formed by the tolerance of longitudinal dimensions, then the form must be separately tolerated. All this is true for location between two or more surfaces. The exceptions for this are: symmetricity and coaxiality, as well as precision of rotation, as they are independent of real dimensions, but they are determined in relation to the central plain and the axis.

Geometrical tolerances are determined only when necessary from the aspect of functional requirements, changeability and eventually from the aspect of production. However, this does not mean automatically that a special way of manufacture, measuring or control has to be used. One specific version of form tolerance is analyzed in this paper, namely roundness.

In order for this analysis to be carried out the following measuring machines were used:
  – PRISMO MPS – CARL ZEISS Industrial Metrology,
  – DEA – Hexagon Metrology and
  – Crysta – Apex C776 – Mitutoyo.
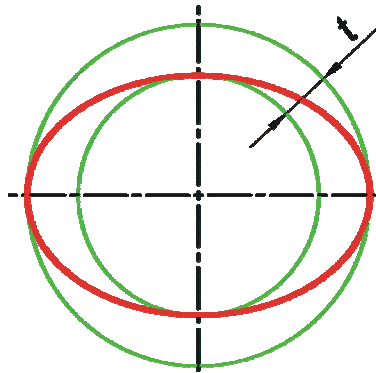
1. 1 Definition of tolerance of roundness

Figure 1. Definition of tolerance of roundness [2,4]

The field of roundness tolerance in the regarded plain is restricted by two concentric circles on the distance *t*. (fig. 1)

If the section lines are tolerated, then all section points must lie between two concentric circles on the section plain, on a radial distance of *t*. This parameter *t* is the value of tolerance of roundness.

2. Methods of roundness measurement

The above listed deviations from the ideal round forms are only of an orientational character. In reality, naturally, we will not receive finely defined

forms, but such forms, where an entire procedure must be carried out in order to define which case this is. This is achieved by introducing various methods of filtration of the gained results. Based on the applied measuring instruments the measurements and control can be grouped as follows:

  – Control using single measuring instruments,
  – Control using multiple measuring instruments (micrometers for external and internal measurements with measurements in two or three points),
  – Control using special measuring instruments fixtures, such as prisms for measurement and comparators; and
  – Control using diagrams which were gained by measurement on measuring machines.

This last group includes measurement using CMM and special measuring machines. CMM, such as flexible metrological systems have the ability to record all necessary information about the workpiece for further analysis, as well as to measure various sizes of the piece. Current measuring machines have the capabilities to process all recorded data owing to the sophisticated software solutions, and so the final image of the analyzed section in the form of a measurement report, in which all relevant measurement data are portrayed, as well as a graphical display of the received form of the workpiece.

3. Measurements

Measurements are carried out in five different location on the table, with the aim to exclude eventual errors which may have occured due to an inaccurate motion mechanism of the carrier construction of the measuring machine. The locations are presented in Fig. 2.
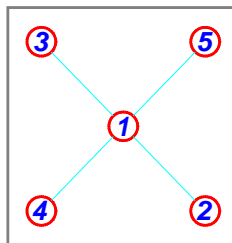

Figure 2. Setup of the measurement locations on the machine table [2]

3.1. Measurement workpieces

Measurement workpieces used for the realization of the experimental measurements are versatile from the aspect of dimensions and locations of measurement plains. We chose master rings (measurement of interior surfaces), a tolerance measurement for the master plug, and a pivot, produced in the

company ATB SEVER as part of the centrifugal pump construction – high quality accuracy considering dimensions, roundness, and cylindricity.

The tolerance master plug and pivot are representations for measurements of exterior surfaces. The dimensions chosen for measurement workpieces are the following:

- Master rings of the diameter D=Ø49,991 mm and D= Ø30 mm.
- Master plug is of the diameter of d= Ø80,
- Finally, the pivot is of the diameter Ø12 mm.

All measurement workpieces are made of high quality steel, thermally processed and ground.

3.2. Presentation of the used measurement machines

This section presents the used coordinate measuring machines and special measuring machines for measuring roundness.

a) Coordinate measuring machine PRISMO MPS – CARL ZEISS Industrial Metrology
- Measuring uncertainty (MPE$_E$): (2,7 + L/300) μm, where L is the length in mm.

b) Coordinate measuring machine DEA - Hexagon Metrology
- Measuring uncertainty (MPE$_E$): (0,9 + L/350) μm, , where L is the length in mm.

c) Coordinate measuring machine Crysta – Apex C776 - Mitutoyo
- Measuring uncertainty (MPE$_E$): (1,7 + 0,4 x L/350)   μ, where L is the length in mm.

d) Measuring roundness on the special machine for determining roundness Roundtest RA-2100 - Mitutoyo

The aim of this measurement was to gain accurate data regarding roundness, which will be used as reference in comparative analysis of measuring capabilities of the coordinate measuring machine.

The most important technical parameters of this measuring machine are:
- rotational accuracy on radial direction: (0,02 + 3,8 H/10 000) μm (H – the height of the workpiece given in mm),
- measuring force: 7 – 40 mN,
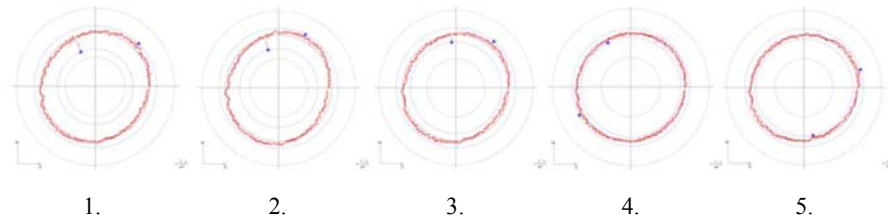- stylus tip form: ϕ1,6 mm.

4. Gained results

Measurement of roundness was carried out on the three described types of CMM. When distributing the measurement workpieces to the various machines, it was vital that on all machines there were interior and exterior surfaces measured by the same measuring probes. The distribution of measurement workpieces on the measuring machines was the following:

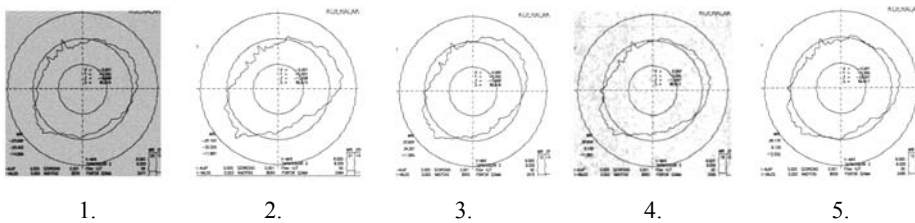1. On the *DEA - Hexagon Metrology* type machine we measured: pivot ϕ 12 mm and master ring ϕ 30 mm.

2. On the *PRISMO MPS – CARL ZEISS Industrial Metrology* type machine we measured: master plug φ 80 mm and master ring φ 49,991 mm.
3. Finally, for comparative results to the coordinate measuring machines, all pieces were also pre-measured on the *Crysta Apex C776 – Mitutoyo* type machine.

On the first two machines the measurings were carried out in five measuring positions. The results will be portrayed indexed by the numbers 1 – 5, depending on the measuring locations. Simultaneously a comparison of those results was carried out depending on the measuring location. Finally, the comparison of the results from the first two machines and the third machine – Mitutoyo was carried out, comparing them with the diagram from the measuring machine *Roundtest RA-2100 – Mitutoyo.*
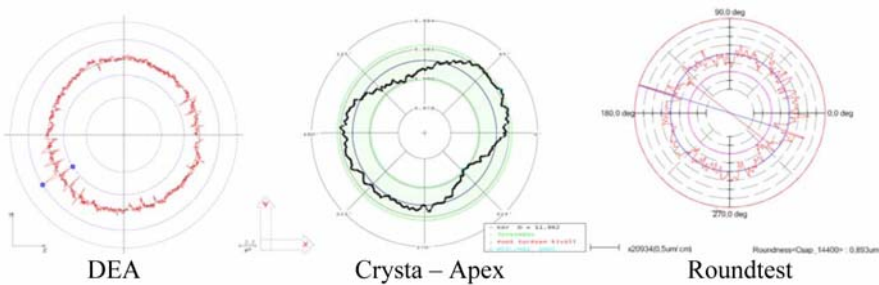
Measuring the φ 30 mm master ring

1.   2.   3.   4.   5.
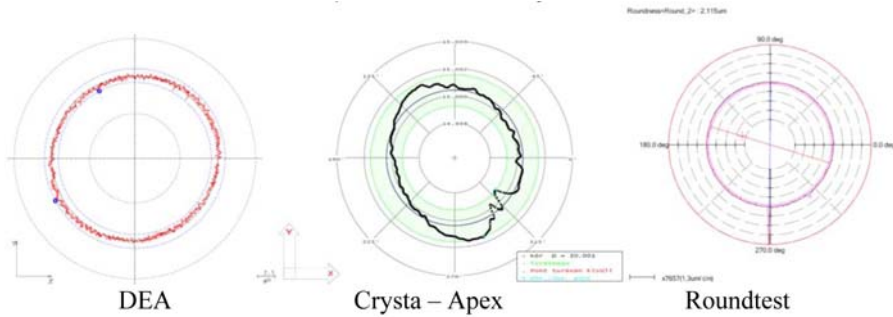
Measuring the master plug φ 80 mm

1.   2.   3.   4.   5.

Results of measurement on the φ 12 mm pivot

DEA   Crysta – Apex   Roundtest

Results of measurement on the ϕ 30 mm master ring

DEA   Crysta – Apex   Roundtest

Results of the measurements on the ϕ 80 mm master plug

PRISMO MPS   Crysta – Apex   Roundtest

Results of the measurement on the ϕ 49,991 mm master ring

PRISMO MPS   Crysta – Apex   Roundtest
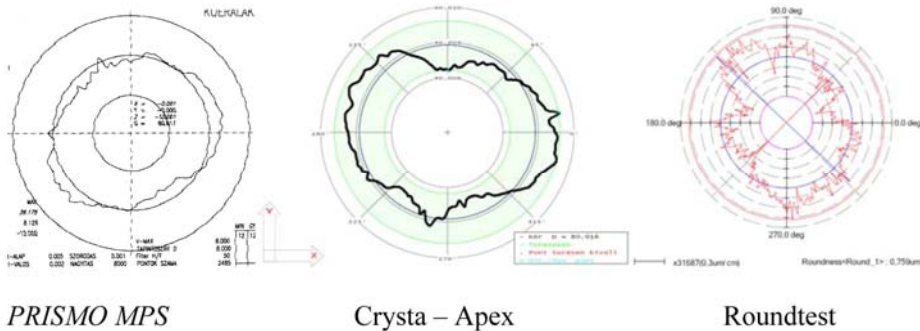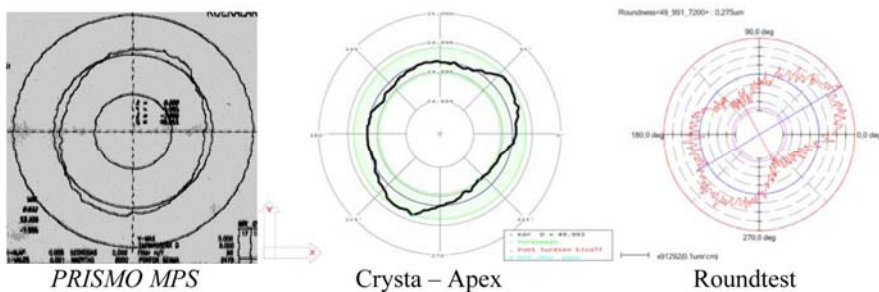
Conclusions

Based on the described facts and comparisons of the measurement results the following can be stated:

– The used machines for determining roundness globally give reliable results concerning the form of deviation of roundness – for the same measurement workpiece not once did it result in versatile forms.
– Recognizing the form of deviation depends in a great degree on the optimal magnification. This can be seen in the case of the CMM *DEA - Hexagon Metrology*, where the magnification was about 4000 times, thus reading the deviation from the form of the diagram was more difficult. Magnification with the other two measuring machines was about 8000 times, thus the form was easily recognizable.
– In the cases where the extreme points are recognizable, all measuring machines ensure their location and calculate their location except with special machines for roundness, which is not meant for such tasks,
– It is important to note that all measured bandwidths of roundness with coordinate measuring machines for the same measurement workpieces were identical or extremely close. This means that the results of the measurement of roundness in these cases did not significantly depend on the size of the measuring uncertainty. Hence, this parameter moved in a rather wide range in the three coordinate measuring machines used. This aspect will need further research.
– As far as accuracy of determining bandwidth of roundness is concerned, the coordinate measuring machine which was not specifically aimed at this type of control and measurement, providing about 3 – 5 time higher values than the results on the roundness machine. Taking into consideration that the sizes in question are only several micrometers, it can be stated that in production, where the tolerance level is usually about one hundredth of a millimeter, the coordinate measuring machines perfectly satisfy the present needs in determining the roundness of the workpieces.

References

[1] Stević, M.: Povećanje tačnosti merenja numerički upravljanih mernih mašina, monografija, Fakultet tehničkih nauka, FTN Izdavaštvo, Novi Sad, 2006.
[2] Nemedi, I.: Vrednovanje sistema za merenje kružnosti, magistarski rad, Fakultet tehničkih nauka, Novi Sad, 2009.
[3] Majstorović, V., Hodolič, J.: Numerički upravljane merne mašine, Fakultet tehničkih nauka, Institut za proizvodno mašinstvo, Novi Sad, 1998.
[4] Szilágyi, L.: Gépipari hosszmérések, Ipari szakkönyvtár, Műszaki Könyvkiadó, Budapest, 1982.
[5] Graham, B.: Scanning and digitising solutions, Metrology Division, Renishaw, USA, 2002. (www.renishaw.com)
[6] Table-Rotating Type Roundness Measuring / Cylindrical Profile Measuring Instruments, Rondcom_Accsy.pdf, Tokio Seimitsu, Japan, 2003., (www.zeiss.de)